



國立臺灣大學理學院大氣科學研究所

碩士論文

Department of Atmospheric Science

College of Science

National Taiwan University

Master Thesis

颱風生成與梅雨鋒之交互作用:凱米(2018)個案分析

The Interactions between Tropical Cyclone Formations and

Mei-Yu Fronts: A Case Study of Typhoon Gaemi (2018)

張玉來

Yu-Lai Chang

指導教授：楊明仁 博士

Advisor: Ming-Jen Yang, Ph.D.

中華民國 110 年 7 月

July, 2021



國立臺灣大學碩士學位論文 口試委員會審定書

本論文係 張玉來 君（學號 R08229004）在國立臺灣大學大氣科學學系、所完成之碩士學位論文，於民國 110 年 07 月 07 日承下列考試委員審查通過及口試及格，特此證明

口試委員：

楊明仁

（簽名）

（指導教授）

游政吉

王重興

李清勝

游政吉

系主任、所長

（簽名）

Acknowledgements



In these two years in graduate school, I appreciated my advisor, Prof. Ming-Jen Yang, firstly. He always guided me with enlightened attitude and encouraged me to confront and solve the arduous challenge. He usually spent much time discussing with me as I had no idea about my research. Every time I felt dejected and insecure, he accompanied with me and bolstered my confidence. Secondly, I was grateful of Prof. Cheng-Ku Yu, who led me into the range of atmosphere research. He also taught me that perseverance is the most critical factor in study. Additionally, I had gratitude to Prof. Cheng-Shang Lee and Chung-Chieh Wang for their willingness to be my committee members. They provided many useful suggestions to help me correct errors and improve my thesis. Thirdly, I expressed my appreciation of the assistances from my teachers and friends. Prof. Hung-Chi Kuo selflessly taught me the mathematics skills and the fundamental geostrophic dynamics. Prof. Chung Hsiung Sui and Jau-Ming Chen assisted me to broaden my view with the interaction between the different-scale systems. Moreover, Hungjui Yu, Mao-Cheng Li, Buo-Fu Chen and Ching-Hsuan Wu contemplated many important ideas and discussed the research strategy with me. Wei-Fan Liu, Yu-An Chen, Hao-ting Chi, Cidny Alexandra Ramirez Martinez, Shang-En Li, Chi Hang Pun, Brian Jeng and other colleagues in CPL lab gave me a hand to implement some analysis and refine my seminar and thesis. Last but not least, I thanked and loved my family. Their support fueled and revived me no matter what the difficulties I met in these two years. I wish that I will contribute to the atmosphere science after I graduate and not disappoint everyone.

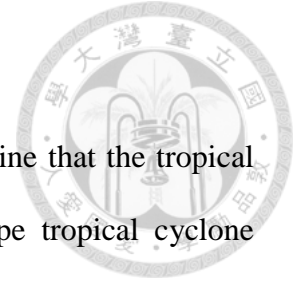
摘要



在本篇研究中，我們參考 Lee et al.(2006)的概念將生成於梅雨鋒面低壓槽的熱帶氣旋定義為鋒面旋生類型並針對其生成機制及其與環境的交互作用進行研究分析。首先，我們透過 1979-2018 年間的鋒面旋生個案分析大尺度環境場的重要特徵，並利用濾波分析分離出不同時間以及空間尺度的特徵。大尺度環流分析表明：強大的西南氣流、底層豐富的氣旋式渦度以及逐漸減少的環境斜壓性有利於熱帶氣旋在梅雨鋒面低壓槽的西南端生成。透過與合成分析的比較，我們驗證了凱米(2018)的代表性並分析他的渦旋尺度過程以及機制。強大的西南氣流促使鋒面區域產生活躍的對流及強水平風切，鋒面上的正壓不穩定產生擾動並且在鋒面低壓的位渦”滋養”下逐漸增強，覆蓋於其中一個渦旋上的中層短波槽協助中層渦旋的建立，最終此渦旋逐漸發展形成凱米(2018)。除了熱帶氣旋的生成外，伴隨的鋒消也是一個值得討論的現象。在凱米生成前，鋒前覆蓋的對流遮蔽太陽短波輻射導致該區域鋒消，斜壓性的減弱也有助於凱米發展為熱帶氣旋。在凱米生成後，其強大的位渦中心會扭曲破壞鋒面的位渦結構，凱米的次環流又會抑制鋒面對流的發展，使得第二類條件不穩定(CISK)被限制導致更進一步的鋒消。最後，我們提出了一個完整的概念模式解釋熱帶氣旋旋生及梅雨鋒面鋒消的過程及這些天氣系統之間的交互作用。

關鍵字:熱帶氣旋生成、梅雨鋒面、濾波分析、位渦、正壓不穩定

Abstract



In this study, we followed the concept of Lee et al. (2006) to define that the tropical cyclones formed in the Mei-Yu frontal depression as the frontal-type tropical cyclone formation. The frontal-type cases during 1979 to 2018 were identified to uncover the essential signatures of the large-scale environments. The filtering method was applied to distinguish the signals from different temporal and spatial scales. The large-scale analyses suggested that the strong southwesterly flow, abundant low-level vorticity and reduction of baroclinicity fertilized the formation of tropical cyclone in the southwest end of the frontal depression. Furthermore, a representative frontal-type case, tropical cyclone Gaemi (2018), was analyzed to investigate the vortex-scale process and mechanism via the reanalysis and the numerical simulation. The southwesterly flow induced the active convection and strong horizontal wind shear in the frontal region. The perturbations were triggered via barotropic instability and the potential vorticity in the frontal depression nourished their intensification. Moreover, the mid-level trough was above one frontal vortex and helped the establishment of mid-level vortex. This perturbation finally developed into a tropical cyclone — Gaemi. In addition to the cyclogenesis mechanism, the frontolysis was an interesting phenomenon as well. The frontolysis was induced by the short-wave radiation prior to Gaemi's development. The reduction of baroclinicity in this stage provided a suitable environment for Gaemi's formation. After Gaemi enhanced, Gaemi's strong potential vorticity distorted the frontal structure and Gaemi's secondary circulation constrained the convection in frontal region. Thus, the Conditional Instability of the Second Kind (CISK) mechanism was restrained and led to the significant frontolysis. Last, a conceptual model was proposed to elucidate the interactions between the tropical cyclone formations and Mei-Yu fronts.

Key words: tropical cyclone formation, Mei-Yu front, filtering analysis, potential vorticity, barotropic instability



Table of Contents



國立台灣大學碩士學位論文口試委員會審定書	i
Acknowledgements	ii
摘要	iii
Abstract.....	iv
Table of Contents	vi
List of Tables	viii
List of Figures.....	ix
Chapter1. Introduction.....	1
Chapter2. Data and Methods	4
2.1 Data	4
2.2 Definition of frontal-type TC formations.....	4
2.3 Filtering method	5
2.4 Model description.....	6
2.5 Budget analysis	7
2.6 The diagnose of Sawyer-Eliassen equation.....	8
Chapter3. Climatology of frontal-type TC formations.....	9
3.1 Statistics results.....	9
3.2 Correlations with intra-seasonal oscillation	9
3.3 Composite analyses of synoptic systems	11
Chapter4. Case overview and Model verification	16
4.1 Gaemi (2018)'s overview.....	16
4.2 The analysis of large-scale circulation and case representativeness	16

4.3 Local evolution.....	20
4.4 Model verification.....	23
Chapter 5. Mechanisms of cyclogenesis and frontolysis.....	25
5.1 Barotropic instability.....	25
5.2 Cyclogenesis process.....	27
5.3 Frontolysis process.....	30
5.4 The role of Taiwan topography.....	34
Chapter 6. Discussion.....	37
6.1 The representativeness of Gaemi (2018).....	37
6.2 The comparison between Gaemi (2018) and Diana (1984).....	39
Chapter7. Conclusions and Future Research Routes.....	42
7.1 Conclusions.....	42
7.2 Future work.....	44
Reference.....	46
Tables.....	51
Figures.....	52



List of Tables



Table 1. The frontal-type TC formations during 1979 to 2018

Table 2. The criteria of MJO (BSISO), ERW, and synoptic systems for filtering analysis

Table 3. Model description for CTL

List of Figures



Figure 1. Figures from other studies: (a) Diana (1984)'s formation (Bosart and Bartlo 1991)
(b) The conceptual model of frontal-type formation (Lee et al. 2006)

Figure 2. The WRF simulation domain. The grid sizes of D01, D02 and D03 are 18, 6 and 2km, respectively.

Figure 3. The averaged circulation of the intraseasonal oscillation associated with frontal-type TC formation. The barbs, color, and countour are wind anomaly (m/s), vorticity anomaly (s-1), and OLR anomaly, respectively. The wind anomaly was 10 times of the actual value. The OLR was only plotted in the strong convection region, where the amount of OLR anomaly was larger than one standard deviation of the whole domina in these period. (a) is the environmental conditions associated with 30-90 days oscillations averaged from 6 days prior to the date when the TSs formed. (b) is the enviromeantal conditions associated with 10-45 days osciallation 6 days prior to the TSs formation. (c) is the same as (b) but 3 days prior to TS formation. (d) is the same as (b) but is on the day as TS formed.

Figure 4. The composite of the synoptic-scale circulations at 850 hPa. The contour, color and barbs are geopotential height(m), relative vorticity (s-1) and wind (m/s), respectively. The black TC symbols mark the averaged locations of TD formation and the blue ones represent those for TS formation. The time was relative to the TS formation time.

Figure 5. The composite of the synoptic-scale evolutions at 850 hPa. The contour, color and barbs are geopotential height (m), wind velocity (m/s) and wind (m/s), respectively. The location of the low-level jet (wind speed>12m/s) was highlighted by red contour. The black TC symbols mark the averaged locations of TD formation and the blue ones represent those for TS formation. The time was relative to the TS formation time.

Figure 6. The composite of the synoptic-scale circulation at 500 hPa. The contour and barbs represent geopotential height (m) and wind (m/s), respectively. The color is thickness between 850 hPa and 500 hPa (m). The black TC symbols mark the averaged locations of TD formation and the blue ones represent those for TS formation. The time was relative to the TS formation time.

Figure 7. The composite of the synoptic-scale circulation at 200 hPa. The color (s^{-1}), contour (m) and barbs (m/s) are divergence, geopotential height and wind, respectively. The black TC symbols mark the averaged locations of TD formation and the red ones represent those for TS formation. The time was relative to the TS formation time.

Figure 8. The evaluation of synoptic-scale vorticity (s^{-1}) and vertical wind shear (m/s). (a) is the calculation domain for composite, which was defined based on Figure 4. (c) is 850-hPa vorticity in the frontal and cyclogenesis regions. (e) is the variation of the vertical wind shear. (b), (d) and (f) are the same as (a), (c) and (e) but only from TC Gaemi (2018).

Figure 9. Gaemi's tracks and the analyses from the JMA. (a) Gaemi's tracks from the JMA, control run (CTL) and sensitive experiment without Taiwan topography (Noterrain) during Gaemi's formation. (b), (c) and (d) are the JMA weather maps at 12 UTC 12 June, 12 UTC 13 June and 00 UTC 15 June, respectively.

Figure 10. Same as Figure 3 except for the case study of TC Gaemi (2018).

Figure 11. Same as Figure 4 except for the case study of TC Gaemi (2018).

Figure 12. Same as Figure 5 except for the case study of TC Gaemi (2018).

Figure 13. Same as Figure 6 except for the case study of TC Gaemi (2018).

Figure 14. Same as Figure 7 except for the case study of TC Gaemi (2018).

Figure 15. Gaemi's local evolution. The dashed line marked the location of the Mei-Yu

front (wind shear line). (a), (c), (e) are at 12 UTC 12 June and (b), (d), (f) are at 00 UTC 13 June. (a) and (b) show the 500-hPa temperature (color, °C), geopotential height (solid line, m) and wind (barb, m/s) in reanalysis data. (c) and (d) show the 850-hPa temperature (color, °C), geopotential height (solid line, m) and wind (barb, m/s) in reanalysis data. (e) and (f) are the brightness temperature (°C) of Band-13 from Himawari-9 Satellite.

Figure 16. Same as Figure 15 except (a), (c), (e) at 12 UTC 13 June and (b), (d), (f) at 00 UTC 15 June.

Figure 17. Same as Figure 15 except at 00 UTC 16 June.

Figure 18. The comparison of the synoptic-scale evolution between reanalysis data and CTL simulation at 00 UTC 13 June. The dashed lines marked the locations of the Mei-Yu front (wind shear line). (a), (c) are from reanalysis data and (b), (d) are from CTL simulation. (a), (b) show the thickness between 850 hPa and 500 hPa (color, m), 500-hPa geopotential height (solid line, m) and 500-hPa wind (barb, m/s). (c), (d) show 850-hPa potential vorticity (color, PVU), 850-hPa geopotential height (solid line, m) and 850-hPa wind (barb, m/s).

Figure 19. Same as Figure 18 except at 12 UTC 13 June.

Figure 20. Same as Figure 18 except at 00 UTC 15 June.

Figure 21. Same as Figure 18 except at 00 UTC 16 June.

Figure 22. Gaemi's local evolution in the CTL simulation. The TC symbols are Gaemi and dashed lines marked the locations of the Mei-Yu front (wind shear line). (a), (c), (e) are at 00 UTC 13 June and (b), (d), (f) are at 12 UTC 13 June. (a) and (b) show the 500-hPa temperature (color, °C), geopotential height (solid line, m) and wind (barb, m/s). (c) and (d) show the 850-hPa temperature (color, °C), geopotential height (solid line, m) and wind (barb,

m/s) (e) and (f) are the brightness temperature ($^{\circ}\text{C}$).

Figure 23. The same as Figure 22 except (a), (c), (e) at 00 UTC 15 June and (b), (d), (f) at 00 UTC 16 June.

Figure 24. The comparison of the vortex-scale evolution between the reanalysis data and CTL simulation. The vorticity and PV were averaged within 200 km from Gaemi's center. The time label which was marked by hours was relative to the time when Gaemi intensified as a TS. (a), (c) are the cyclogenesis process from reanalysis data and (b), (d) are from CTL simulation. (a), (b) are relative vorticity and (c), (d) are PV.

Figure 25. The comparison of the frontal evolution between reanalysis data and the CTL simulation. The frontogenesis function and PV were averaged within 200 km from the front. The time label which was marked by hours was relative to the time when Gaemi intensified as a TS. (a), (b) are the frontogenesis function in reanalysis and the CTL run, respectively, prior to Gaemi's formation between 110°E and 120°E . (c) is the comparison of PV in reanalysis and the CTL simulation between 125°E and 135°E as Gaemi approached.

Figure 26. The subjectively analysis of barotropic instability. (a) is a classic mass-field distribution of the barotropic instability (Kuo and Horng 1994). In (b) (06 UTC), (c) (09UTC) and (d) (12 UTC), the TC symbols is the frontal vortex which developed into Gaemi and the star is another frontal vortex. The dashed line is the location of the front (wind-shear line). The color, contour, and barbs are PV (PVU), geopotential height (m), and wind (m/s), respectively.

Figure 27. The PV distribution at 500 hPa and 850 hPa. The TC symbols are Gaemi. The dashed line is the Mei-Yu front. The color, contour, and barbs are PV (PVU), geopotential height (m), and wind (m/s), respectively. (a), (c), (e) are 500-hPa distributions at 03 UTC

13 June, 12 UTC 13 June and 00 UTC 15 June. (b), (d), (f) are 850-hPa evolutions at 03 UTC 13 June, 12 UTC 13 June and 00 UTC 15 June.

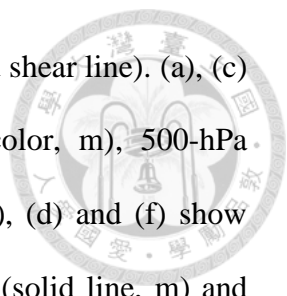
Figure 28. The PV budget and the associated diabatic heating. (a), (c), (e) are the PV profiles contributed by different forcings (PVU/2hours) from 02 to 04 UTC 13 June, 11 to 13 UTC 13 June, and 23 UTC 14 June to 01 UTC 15 June, respectively. (b), (d), (f) are the diabatic heating profiles (K/2hours) from 02 to 04 UTC 13 June, 11 to 13 UTC 13 June, and 23 UTC 14 June to 01 UTC 15 June, respectively.

Figure 29. Diabatic heating in frontal boundary layer prior to Gaemi's formation. The dashed line is the location of the Mei-Yu front and the black box is the calculation domain of Figure 25(b). The barbs are wind. The color in (a) and (b) is summation of sensible heat flux, latent heat flux and long-wave radiation (W/m^2). The color in (c) and (d) is sensible heat flux (W/m^2) from surface. The color in (e) and (f) is latent heat flux (W/m^2) from surface. In addition, (a), (c) and (e) are at 00 UTC 13 June (frontogenesis stage). (b), (d), (e) are at 06 UTC 13 June (frontolysis stage).

Figure 30. Same as figure 29. The color in (a) and (b) is radar reflectivity (dBz). The color in (c) and (d) is downward short-wave radiation at surface (W/m^2). In addition, (a), (c) are at 00 UTC 13 June (frontogenesis stage). (b), (d), are at 06 UTC 13 June (frontolysis stage).

Figure 31. The frontolysis process from the PV aspect. (a), (b) and (c) are the PV distribution (color), geopotential height (contour), and wind (barbs) at 850 hPa. (d) shows the PV budget terms (PVU/2hours) and vertical velocity ($-Pa/s$). Every term was averaged within the black box in a-c. (e) is the diabatic heating below 600 hPa (K/2hours). (f) was the vertical velocity from the diagnose of Sawyer-Eliassen equation.

Figure 32. The synoptic-scale evolution in Noterrain simulation. The TC symbols are



Gaemi and the dash lines marked the location of the Mei-Yu front (wind shear line). (a), (c) and (e) illuminate the thickness between 850 hPa and 500 hPa (color, m), 500-hPa geopotential height (solid line, m) and 500-hPa wind (barbs, m/s). (b), (d) and (f) show 850-hPa potential vorticity (color, PVU), 850-hPa geopotential height (solid line, m) and 850-hPa wind (barbs, m/s).

Figure 33. The vortex-scale evolution in Noterrain simulation. The vorticity and PV were averaged within 200 km from Gaemi's center. (a) is relative vorticity and (b) is PV.

Figure 34. Gaemi's local evolution in Noterrain simulation. The TC symbols are Gaemi and dash lines marked the locations of the Mei-Yu front (wind shear line). (a), (c), (e) are at 12 UTC 13 June and (b), (d), (f) are at 00 UTC 15 June. (a) and (b) show the 500-hPa temperature (color, °C), geopotential height (solid line, m) and wind (barb, m/s) (c) and (d) show the 850-hPa temperature (color, °C), geopotential height (solid line, m) and wind (barb, m/s). (e) and (f) are the brightness temperature (°C).

Figure 35. The 200-hPa PV at (a) 00 UTC and (b) 12 UTC on 13 June. The color is PV (PVU), contour is 200 hPa geopotential height (m), and barbs (m/s) are wind.

Figure 36. The conceptual model for the interactions between the frontal-type TC and the Mei-Yu front. (a) is prior to TC formation. In this stage, the short-wave radiation induced the frontolysis and the east section of front was maintained by the CISK. The barotropic instability triggered low-level perturbations and the short-wave trough helped the establishment of the mid-level PV pool. (b) is after TC formation. The TC was a strong PV center to organize the weak PV pool adjacent to the TC. The frontal PV was pumped out by the TC and the secondary circulation of the TC restrained the convection in the frontal region. The front experienced significant frontolysis as TC approached.

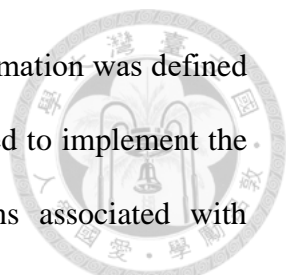
Chapter1. Introduction



Above the tropical ocean, some disturbance can develop into tropical cyclone (TC) in the suitable environment where the low-level vorticity is abundant and vertical wind shear is weak (Gray 1968; 1975; 1979; Fu et al. 2012). The environmental conditions are usually regulated by large-scale circulation. While a large-scale low pressure passed tropical ocean, it can induce deep convection which further aggregates in the specific region and establish substantial cyclonic-vorticity anomaly at low level (Gill 1980; Wheeler and Kiladis 1999; Wheeler et al. 2000), which is favorable for TC cyclogenesis. Hence, TC formations usually gather in particular phase of the large-scale oscillations (Chen et al. 2018).

Some TCs, however, were able to form in an extratropical environment (Gray 1998). In the past, several papers have analyzed these phenomena. For example, Hurricane Diana (1984) was a famous case, which formed in a strong baroclinic environment and many studies have explored its formation (Figure 1a). Bosart and Bartlo (1991) described the formation process and indicated some possible mechanisms. The invasion of stratosphere air induced a potential vorticity (PV) anomaly formed at high level and the positive PV advection associated with this PV patch triggered the mid-level ascent, which could enhance the convection and the depression at low level. Afterwards, the environmental baroclinicity reduced due to the transport of latent heat and sensible heat from surface. The low-level depression was also transformed from a mid-latitude system into a tropical system owing to the latent heating by the active convection. The roles of upper-level trough and latent heat release were both verified through numerical simulation and sensitivity experiments (Davis and Bosart 2001; 2002; 2003).

Similarly, Lee et al. (2006) explored TC formations associated with Mei-Yu fronts and



elucidated the effects of the synoptic systems. Firstly, “frontal-type” formation was defined and the cases formed in South China Sea (hereafter SCS) were identified to implement the composite analysis. Secondly, the synoptic environmental conditions associated with frontal-type formations were summarized: the enormous cyclonic vorticity in the Mei-Yu depression and the intense southwesterly flow at low level, the conspicuous short-wave troughs adjacent to the disturbances at middle levels, and the obvious divergence related to the diffluent flow at high level. Last, a conceptual model of frontal-type formations was proposed to portray the formation process (Figure 1b). In addition to the synoptic analyses, Lee et al. (2008) simulated the Noguri’s (2002) formation, a classic frontal-type formation, to describe the mesoscale processes of cyclogenesis.

To further examine the roles of Mei-Yu front on frontal-type TC formations, discussion about Mei-Yu frontal structure was essential as well. Mei-Yu fronts resemble the mid-latitude systems in the eastern portion (near Japan) but the fronts are akin to the tropical disturbances in the western section (near Southern China). In general, Mei-Yu fronts exhibit intense horizontal wind shear, abundant vorticity but relatively weak temperature gradient (Chen and Chang 1980). Due to the lack of significant baroclinic forcing from synoptic-scale systems, Mei-Yu front, especially in the western section, relies on the CISK mechanism from convective-scale systems (Charney and Eliassen 1964) to preserve frontal structure: strong frontal convergence triggers the active convection in the frontal region. Latent heat release in convective systems induces that PV (vorticity) augment in the frontal area. Convergence in the frontal vicinity is strengthened by Ekman pumping and facilitates the development of convective systems. Cyclogenesis via CISK enhances deformation to further improve frontogenesis. Based on this argument, PV (or

relative vorticity) is not only the definition of cyclogenesis, but also an indicator of frontogenesis in the Mei-Yu fronts with weak baroclinicity and even better than temperature gradient (Kuo and Anthes 1982; Cho and Chen 1995; Chen et al. 2003; 2008).

The above-mentioned papers have studied the frontal-type TC formations and the dynamic structure of the Mei-Yu front. Nevertheless, the roles of different-scale circulations on frontal-type TC formations have not been fully explored. The vortex-scale evolutions and mechanisms were not comprehensively elucidated in the past studies. Since the frontal-type TCs formed under strong synoptic-scale forcing relative to the typical TC formations, other weather systems, such as Mei-Yu front, could exert the obvious influence on the TCs during the TC formations. Additionally, the strong PV centers and secondary circulations of TCs are able to affect the CISK mechanism in the frontal regions. However, the evolution of Mei-Yu fronts during TC formations and the impacts induced by TCs were not explored either. In this study, we would investigate the large-scale fields associated with the frontal-type TC formations in Chapter3 first. The background circulations in different temporal and spatial scales were composited to analyze. Secondly, a representative case, TC Gaemi (2018), would be studied to illustrate the vortex-scale process of the frontal-type TC formations in Chapter4 and Chapter5. Finally, the frontal evolution associated with Gaemi's formation was also analyzed in Chapter4 and Chapter5 to uncover the interactions between frontal-type TC and the Mei-Yu front.

Chapter2. Data and Methods



2.1 Data

Various data were utilized in this study. Firstly, the ERA-5 (Hersbach et al. 2018) provided by European Centre for Medium-Range Weather Forecasts (ECMWF) was used in the objective analyses and the WRF model simulation. The ERA5, an hourly reanalysis data with 0.25° horizontal grid size and 37 vertical levels, are able to resolve synoptic and meso-alpha signatures. This database after 1979 was utilized in this study due to the assurance of data quality. Secondly, the frontal systems were subjectively examined based on the daily weather charts from Japanese Meteorological Agency (JMA). Corresponding to the weather analysis, JMA's best track data were adopted to evaluate TC strengths and locations. Last, the satellite-observed brightness temperature data with 2-km spatial grid size and 10-mininutes temporal interval were analyzed to investigate the convective systems in the vicinity of Mei-Yu front and TC. This databank was retrieved from Himawari-9 satellite and provided by Chiba University.

2.2 Definition of frontal-type TC formations

The frontal-type TC formations were defined based on the concept proposed by Lee et al. (2006) with several refinements:

- 1) The TCs formed during May to June and strengthened into TS
- 2) The frontal region was defined as the area adjacent to Mei-Yu front marked on JMA weather charts and with relative vorticity exceeding 10^{-5} s^{-1} and PV exceeding 0.3 PVU at 850 hPa on this front.
- 3) The TC's closed surface isobars were located at the southwest end of the frontal region prior to TC formation.

The cases of frontal-type TC formations from 1979 to 2018 were shown in Table 1.

2.3 Filtering method

The Fourier decomposition was performed to distinguish the signals between the synoptic-scale background and the vortex-scale signals (Hendricks et al. 2010; Wei and Yang 2015). This technique helped to focus on the evolution of synoptic- and larger-scale background to uncover the possible mechanism fertilizing TC formations. To discriminate the circulations of TCs from environment and Mei-Yu front, the distinction of properties was vital to discuss. The spatial scale of Mei-Yu depressions is several hundred kilometers in the across-front direction, which resembled the scale of TC. Nonetheless, the temporal scale is obviously difference between TC (about 7-8 days) and Mei-Yu front (about 2 weeks) in these cases. Hence, we filter out the vortex-scale signatures by removing the waves with the period less than 8 days.

In addition to the synoptic analyses, filtering was also applied to diagnose the influence of intraseasonal oscillation as well (Wheeler and Kiladis 1999). Kikuchi and Wang (2009) indicated that the energies of intraseasonal oscillations in the Northwestern Pacific are concentrated in two peaks, 10-24 days and 30-60 days. The signal of 10-45 days is guided by equatorial Rossby wave (ERW) and the signal of 30-90 days is dominated by Madden-Julian oscillations (MJO) or Boreal Summer Intraseasonal Oscillation (BSISO). Referring to the wave-amplitude distribution shown by Wheeler and Kiladis (1999), the 30-90 days temporal filter and the spatial filter of 0-5 eastward latitudinal wavenumber were adopted to capture the behaviors of MJO or BSISO (hereafter 30-90 days oscillation for both MJO and BSISO). The 10-45 days temporal filter and the spatial filter of 1-10 westward latitudinal wavenumber were implemented to investigate the signatures of ERW.

The details of the filtering analyses were described in Table 2.

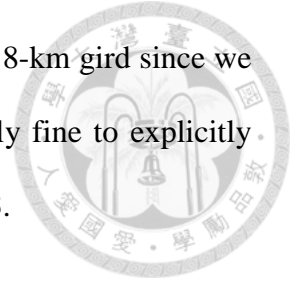
2.4 Model description

Version 3.9 of WRF-ARW (Skamarock et al. 2008) was utilized to simulate Gaemi (2018). The WRF domain was shown in Figure 2. The horizontal grid sizes of the triply-nested domain are 2, 6 and 18 km, respectively. The convection was assumed to be captured by 2-km grids reasonably and the structure of synoptic systems, such as subtropical high, could be simulated on the wide outermost domain. Two-way interactions between the inner and outer domain was considered. Additionally, sixty eta-levels with higher resolution in the planetary boundary layer (PBL) were used to resolve the small-scale forcing in PBL. The vertical-velocity damping was implemented to prevent the numerical instability induced by high vertical resolution.

Moreover, TC Gaemi (2018) was simulated from 00 UTC 12 June to 00 UTC 16 June with the initial values and boundary conditions from the ERA5. The simulation results were analyzed since 00 UTC 13 June so that model has sufficient time to spin up and generate convective systems. In addition to the longer spin-up time, four-dimensional data assimilation (FDDA), so-called nudging, was performed to maintain synoptic-scale signatures during the spin-up period (Stauffer and Seaman 1990). Grid nudging was conducted in the first 21 hours with factors of 0.0004, 0.0002 and 0.0001 in the outermost, intermediate and innermost grids, respectively.

Last, the physical parameterization schemes included the Grell-3D ensemble cumulus parameterization, the double-moment WDM6 microphysics parameterization (Lim and Hong 2010), the Goddard long-wave and short-wave radiation parameterization (Chou and Suarez 1999; Chou et al 2001), and the Yonsei University (YSU) PBL parameterization





(Hong and Pan, 1996). Cumulus scheme was only implemented in the 18-km grid since we assumed that the grid sizes of the 6-km and 2-km grids are sufficiently fine to explicitly resolve convection. Details of simulation settings were shown in Table 3.

2.5 Budget analysis

In this study, budget analyses were applied to quantitatively evaluate the cyclogenesis and frontogenesis (frontolysis) process. PV budget was conducted to determine the critical forcings responsible for Gaemi's cyclogenesis and frontolysis. According to Hoskins et al. (1985), Ertel PV (Ertel 1942) is an essential parameter describing the cyclogenesis due to its conservation and invertibility. Moreover, the augmentation of PV was an indicator of frontogenesis in the Mei-Yu front with weak baroclinicity (Cho and Chen 1995; Chen et al. 2003; 2008). Under the assumption of the hydrostatic equilibrium, the relative PV equation and tendency equation were evaluated as:

$$PV = \frac{\bar{\zeta}_a \nabla \theta}{\rho} \sim -g \zeta_a \cdot \frac{\partial \theta}{\partial p}, \quad \text{Eq. (1)}$$

$$\frac{\partial PV}{\partial t} \sim -(\bar{V} - \bar{c}) \nabla_p PV - \omega \frac{\partial PV}{\partial p} - g \zeta_a \frac{\partial}{\partial p} \left(\frac{D\theta}{Dt} \right), \quad \text{Eq. (2)}$$

$$\text{TEN} = \text{HAD} + \text{VAD} + \text{DIA}, \quad \text{Eq. (3)}$$

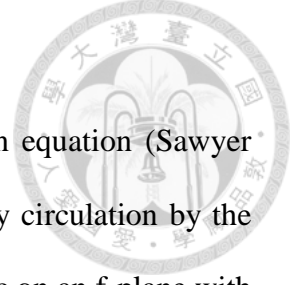
In addition to the PV budget, the frontogenesis function was calculated as:

$$\begin{aligned} \frac{d}{dt} |\nabla \theta| = & -\frac{1}{|\nabla \theta|} \left(\left(\frac{\partial \theta}{\partial x} \right)^2 \left(\frac{\partial u}{\partial x} \right) + \left(\frac{\partial \theta}{\partial y} \right)^2 \left(\frac{\partial v}{\partial y} \right) + \frac{\partial \theta}{\partial x} \frac{\partial \theta}{\partial y} \left(\frac{\partial u}{\partial x} + \frac{\partial v}{\partial y} \right) + \frac{\partial \theta}{\partial z} \left(\frac{\partial w}{\partial x} \frac{\partial \theta}{\partial x} + \frac{\partial w}{\partial y} \frac{\partial \theta}{\partial y} \right) - \right. \\ & \left. \left(\frac{\partial \theta}{\partial x} \frac{\partial}{\partial x} \left(\frac{d\theta}{dt} \right) + \frac{\partial \theta}{\partial y} \frac{\partial}{\partial y} \left(\frac{d\theta}{dt} \right) \right) \right) \quad \text{Eq. (4)} \end{aligned}$$

$$\text{frontogenesis} = \text{stretch} + \text{horizontal shear} + \text{tilting} + \text{diabatic} \quad \text{Eq. (5)}$$

(Miller 1948; Colle et al. 2002)

All of the budget terms were calculated in a system-centric quasi-Lagrangian framework (Yang et al. 2018).



2.6 The diagnose of Sawyer-Eliassen equation

Following the concept of Schubert et al. (2007), Sawyer-Eliassen equation (Sawyer 1956; Eliassen 1962) was implemented to diagnose Gaemi's secondary circulation by the cooperation with Shang-En Lee. It was assumed that TC is axisymmetric on an f-plane with the gradient-balance circulation and there was no tangential component of the secondary circulation. We could obtain the Sawyer-Eliassen equation as:

$$\frac{\partial}{\partial r} \left(A \frac{\partial(r\psi)}{r\partial r} + B_t \frac{\partial\psi}{\partial z} \right) + \frac{\partial}{\partial z} \left(B_v \frac{\partial(r\psi)}{r\partial r} + C \frac{\partial\psi}{\partial z} \right) = \frac{g}{C_p T_0} \frac{\partial Q}{\partial r} \quad \text{Eq.(6)}$$

$$\left\{ \begin{array}{l} e^{-\frac{z}{H}} u = -\frac{\partial\psi}{\partial z} \\ e^{-\frac{z}{H}} w = \frac{\partial(r\psi)}{r\partial r} \\ A = e^{\frac{z}{H}} \frac{g}{T_0} \left(\frac{\partial T}{\partial z} + \frac{\kappa T}{H} \right), \kappa = \frac{R}{C_p}, \\ B_t = -e^{\frac{z}{H}} \frac{g}{T_0} \frac{\partial T}{\partial r}, \\ B_v = -e^{\frac{z}{H}} \left(f + \frac{2v}{r} \right) \frac{\partial v}{\partial z}, \\ C = e^{\frac{z}{H}} \left(f + \frac{2v}{r} \right) \left(f + \frac{\partial(r\psi)}{r\partial r} \right), \end{array} \right. \quad \text{Eq. (7)}$$

where $z = H \log\left(\frac{p_0}{p}\right)$, $H = \frac{RT_0}{g}$ were defined as the vertical coordinate and constant scale height, w was the vertical velocity in this coordinate, u and v were the radial velocity and tangential velocity, Q was the diabatic heating.

In this analysis, the diabatic heating was evaluated by the axisymmetric average of the latent heat release in 3-km radial spacing within 2500 km from Gaemi's center. The vertical range of the domain was from 40 hPa to 960 hPa with 20-hPa grid size. T_0 was set as 250 K, which was near the mean temperature in troposphere, and P_0 was 1000 hPa. The Holton balance (Holton 2004; Montgomery and Persing 2021) was utilized to obtain the gradient-balance circulation and temperature.

Chapter3. Climatology of frontal-type TC formations



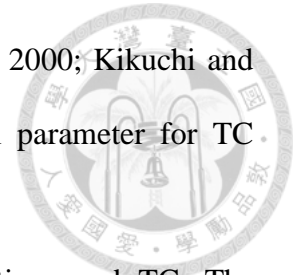
3.1 Statistics results

According to the statistics from the TC cases in Table 1, there were fourteen frontal-type TC formations in 1979-2018. These frontal-type TCs averagely developed into tropical depression (hereafter TD) at 18.1°N , 117.1°E , and developed into tropical storm (hereafter TS) at 20.2°N , 120.0°E , where it was in northeastern South China Sea (hereafter SCS). Guided by the seasonal mean circulation, the frontal-type TCs averagely moved Northwesterly. Moreover, the frontal-type TCs spent about 2 days (46.7 hours) strengthening from TD to TS. These statistics results resembled the conclusions proposed by Lee et al. (2006) and Chen et al. (2020). In addition to these statistics of TCs, the filtering results with different spatial and temporal scales were composed based on the time when TCs reached the TS intensity. In the following two sections, the environmental conditions of frontal-type TC formations were quantitatively studied by composite analyses.

3.2 Correlations with intra-seasonal oscillation

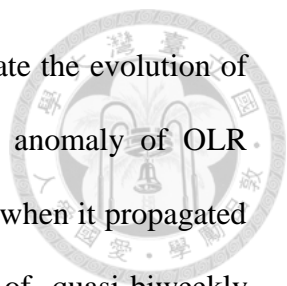
In the baroclinic environment, fluctuations would develop into mid-latitude cyclones if they encountered suitable environmental conditions (Charney 1947; Petterssen and Smebye 1971; Hoskins et al. 1985). Nonetheless, frontal-type TCs could overcome the strong vertical wind shear and develop into TCs. In these frontal-type TC formations, the intraseasonal oscillations may play essential roles since intraseasonal oscillations can establish a background with stronger vorticity at low level and higher relative humidity at middle level in specific phase (Chen et al. 2018). To clarify the association between intraseasonal oscillations and the frontal-type TC formations, the filtering on OLR and relative vorticity at 850 hPa were investigated. Anomaly of OLR can represent the location

and strength of convection (Wheeler and Kiladis 1999; Wheeler et al. 2000; Kikuchi and Wang 2009) and vorticity anomaly at low level is the most critical parameter for TC formations (Fu et al. 2012; Chen et al. 2018).



Firstly, we studied the association between 30-90 days oscillations and TC. The temporal scale of 30-90 days oscillations was far larger than synoptic scale (several days). Therefore, the filtering results was composited from 6-day before TS formations to the day TS formed to examine the averaged 30-90 days anomaly during TC formations (Figure 3a). In this mean field, the strong convection region, where the negative anomaly of OLR was larger than one standard deviation of the analysis domain, covered the Bay of Bengal, Indochina Peninsula and SCS. This distribution of OLR suggested the active phase of 30-90 days oscillations propagated into Indochina Peninsula and SCS (Chen et al. 2018) during the frontal-type TC formations. Additionally, the aggregation of convection generated an asymmetric latent-heating source (relative to equator) spanning from Indochina Peninsula to SCS. This strong heating source stimulated not only the obvious anomaly of southwesterly flow but also the substantial anomaly of cyclonic vorticity in SCS and Northwestern Pacific based on the Matsuno-Gill's solution (Matsuno 1966; Gill 1980). The stronger southwesterly flow could transport plentiful vapor from Indian Ocean to fertilize the convection in SCS and the frontal region, which extended from Taiwan to Okinawa. The background circulation with abundant cyclonic vorticity in SCS and the frontal region could enhance the Mei-Yu frontal depression and further nourish TC formations (Gray 1975; Gray 1979; Fu et al. 2012; Chen et al. 2018) as well.

Secondly, the roles of ERW were discussed as well. Differing from the scale of 30-90 days oscillations, the scale of ERW is similar to synoptic scale. Thus, the filtering results



prior to TC formations were shown in Figure 3b, 3c, and 3d to illuminate the evolution of background circulation. Six days before TS formation, a significant anomaly of OLR (larger than one standard deviation) gradually intensified and elongated when it propagated from Western Pacific to Eastern Asia, similar to the behaviors of quasi-biweekly oscillations shown by Kikuchi and Wang (2009). The substantial anomaly of OLR covered most of the vicinity ahead of the Mei-Yu front three days prior to TS formation (Figure 3c). As a result, the ERW could trigger more active convection ahead of the front, which could lead to more severe frontal circulations (Chen et al. 2003) to enhance the frontal depression. Akin to 30-90 days oscillations, the associated anomaly of cyclonic vorticity was able to strengthen the Mei-Yu frontal depressions and establish an abundant-vorticity environment nourishing the TC formations. The obvious anomaly of southwesterly flow also enhanced the southwesterly flow ahead of front and even helped the formation of low-level jet. Moreover, the amplitude of ERW was much larger than 30-90 days oscillations. ERW has more contribution to the frontal-type TC formations.

Both of 30-90 days and the ERW oscillations established positive vorticity anomaly at low level and induced the aggregation of convection in SCS. In addition, 30-90 days oscillation and the ERW were able to generate the anomaly of southwesterly flow and help the formation of atmospheric river (shown in Section 3.3), which can strengthen the vapor flux and the horizontal wind shear in frontal region (discussed in Chapters 4 and 5). Accordingly, these composite analyses of intraseasonal oscillations confirmed that intraseasonal oscillations indeed establish a suitable environment for the TC cyclogenesis.

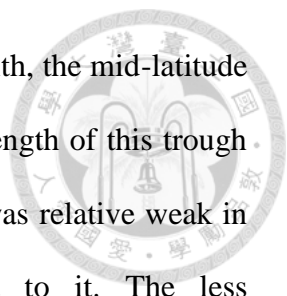
3.3 Composite analyses of synoptic systems

The synoptic-scale systems were modulated by intraseasonal oscillations and guided

the evolution of vortex-scale systems. Therefore, synoptic analyses could comprehensively elucidate the influences of large-scale circulations on frontal-type TC formation. Lee et al. (2006) has summarized the common synoptic signatures and proposed a conceptual model to describe the synoptic evolutions during frontal-type formation through composite analysis. In this study, we further analyzed synoptic circulations (with larger-scale signals) via filtering skills and quantitative computation.

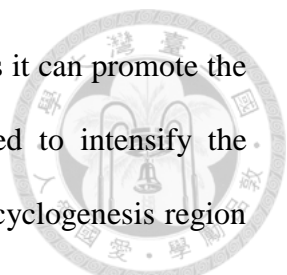
First of all, we discuss the synoptic evolution at 850 hPa (Figure 4). The low-level patterns were most essential for frontal-type formations since Mei-Yu front is a shallow depression (Chen and Chang 1980) and TC cyclogenesis develops from low level via vortical hot tower (Hendricks et al. 2004; Montgomery et al. 2006). A frontal depression (positive relative vorticity region) extending from SCS to Okinawa was built 144 hours prior to TS formation and gradually. The average location of the frontal-type TC formations was in the southwest end of the frontal depression (northeastern SCS). It fertilized the TC formations that the depression deepened and the cyclonic vorticity strengthened until the cyclone developed into a TC. In addition, modulated by intraseasonal oscillation, an intense atmospheric river (Newell et al. 1992, Zhu and Newell 1994) from Indian Ocean invaded SCS and Western Pacific and transport abundant vapor (Figure 5). The wind speed was robust and steady that the wind speed in synoptic scale reached the criteria of low-level jet (12m/s; Zeng et al. 2019) above Indochina Peninsula, which can trigger severe convection and precipitation (Matsumoto 1972; Chen and Yu 1988).

Secondly, the mid-level systems were also a crucial forcing in frontal-type cyclogenesis (Figure 6). The development of the mid-level trough-ridge systems implied variations of the environmental baroclinicity and the mid-level vortex should be established



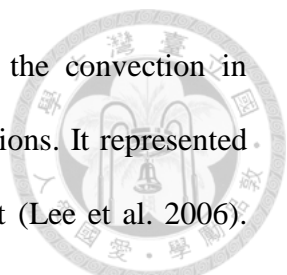
during TC cyclogenesis (Raymond et al 2011; Davis 2015). To begin with, the mid-latitude baroclinic wave was far from the location of TC formation and the strength of this trough did not amplify either. This evolution suggested that the baroclinicity was relative weak in formation environment although the Mei-Yu front was adjacent to it. The less intensification of baroclinic wave also indicated that the frontogenesis of the Mei-Yu front should attribute to the mechanisms except baroclinic instability. In addition, a mid-level, short-wave trough was located above the northern SCS, where it was west of the averaged location of TC formation. Thus, this short-wave trough could induce the positive vorticity advection at middle level and help the establishment of the mid-level vortex. Moreover, this short-wave trough in which the thickness between 850 and 500 hPa was thicker than the adjacent vicinity was not a baroclinic wave, but might be induced by latent heating in convective systems. Thus, it could prevent the low-level disturbance to develop into a mid-latitude cyclone since this short-wave trough did not enhance the low-level cold advection. Last, the conspicuous diffluent flow of Southern Asia High induced substantial divergence at 200hPa (Figure 7) above the SCS. The high-level divergence could promote the outflow of convection and TC circulation. According to the above-mentioned synoptic pattern, the frontal-type TC formed in a frontal depression with abundant low-level vorticity but the baroclinicity was limited. The mid-level trough and high-level diffluence nourished the TC formation as well.

To further clarify the synoptic evolutions, two essential parameters, low-level vorticity and vertical wind shear, were evaluated in the upstream region, cyclogenesis region, and frontal region, respectively (Figure 8a). In general, the relative vorticity (Figure 8c) in the cyclogenesis region and the frontal region both augmented 72 hours prior to TS formations.



The Mei-Yu front strengthened and the TC formations were fertilized as it can promote the frontogenesis and cyclogenesis that the Mei-Yu depressions deepened to intensify the deformation. Afterwards, the relative vorticity started to decline in the cyclogenesis region 48 hours before TS formation, when the TD averagely formed. It showed the kinematics energy was transported from synoptic-scale systems to mesoscale systems that the reduction of the environmental vorticity and the TC cyclogenesis were simultaneous. This energy-cascade (Smith and Waleffe, 1999) process was consistent to the bottom-up theory indicating that the TC cyclogenesis was triggered by the low-level vorticity concentration. Differing from the typical TC formations with weak synoptic disturbance above the tropical ocean, the frontal-type TC formations still associated with the obvious energy cascade after TC formed owing to the strong synoptic system adjacent to TC, such as Mei-Yu front. This result indicated that the intensification of the frontal-type TC could be persistently influenced by environmental systems after TC formation. Similarly, the relative vorticity also began to decrease in the frontal region 72 hours prior to TS formations. The weakening of frontal depression restricted the heating efficiency in the CISK mechanism and the averaged strength of deformation in the frontal region.

In additional to the 850-hPa vorticity, the vertical wind shear between 850hPa and 200hPa, which was detrimental to TC formation, were analyzed as well (Figure 8e). The vertical wind shear in the cyclogenesis area was least throughout the whole TC formation period. It was the reason why the TCs could only form in the cyclogenesis region but not in the frontal region or the upstream region. Nevertheless, the vertical wind shear (about 10 m/s) in the cyclogenesis region was substantially greater than the typical value during TC formations in the northwestern Pacific, which was less than 10 knots (Gray 1968). The



stronger vertical wind shear could restrict the heating efficiency of the convection in frontal-type TC and restrain the intensity of the frontal-type TC formations. It represented the strength of the frontal-type TCs were constrain in this environment (Lee et al. 2006). Furthermore, the environmental conditions favored frontogenesis 72 hours prior to TS formation due to the intensification of vertical wind shear. Akin to the relative vorticity, the vertical wind shear started to decline 72 to 24 hours before the TS formations. The baroclinicity reduction established a relatively suitable environment for TC formation. By contrary, the considerable decline of the vertical wind shear in the frontal region could directly lead to the frontolysis and the vorticity decrease further enhanced frontolysis. If the vorticity of mesoscale systems also vanished, the Mei-Yu front would weaken owing to the lack of baroclinic forcing and the reduction of deformation in synoptic scale.

These synoptic analyses elucidated the evolution of environmental conditions which modulated the cyclogenesis, frontogenesis and frontolysis in the different stages. Nevertheless, the mesoscale processes of the frontal-type TC formations should be further examined to clarify the interactions between the TC and the Mei-Yu front. Hence, a case study of TC Gaemi (2018) was conducted to illustrate these scientific questions in the following chapters.

Chapter4. Case overview and Model verification



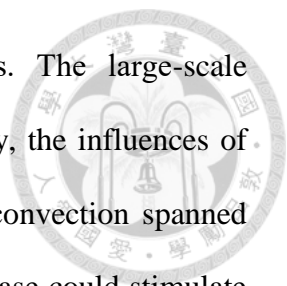
4.1 Gaemi (2018)'s overview

The statistic studies were only applied to explore the coarse-resolution signatures since composite analysis could blur the fine-resolution structures. A representative case study was vital to uncover the vortex-scale process of frontal-type TC formations. In this study, TC Gaemi (2018) was utilized to illustrate the mechanism of cyclogenesis and frontolysis.

The JMA's best track and weather charts were shown in Figure 9a. A stationary front (Mei-Yu front) moved northward to Bashi channel and extended into southern China prior to 12 UTC 12 June 2018 (Figure 9b). At 12 UTC 13 June 2018, a vortex at the southwest end of the front developed into a TD (Figure 9c). This TD translated northeastward to Taiwan Strait along the frontal depression and strengthened into TS Gaemi (2018) at 00 UTC 15 June 2018 (Figure 9d). After Gaemi intensified as a TS, it still translated northwestward and transformed into an extratropical cyclone (not shown). In addition to Gaemi's cyclogenesis, the frontolysis was another worthwhile phenomenon as well. The southwest end of front vanished when the TD formed and the front "dissipated" after Gaemi passed it. Thus, the southwest patch of the front must experience tremendous frontolysis when Gaemi formed and approached. During Gaemi's formation, the vorticity in the frontal depression could nourish the cyclogenesis. Gaemi was also able to affect the front via its strong PV and secondary circulation after Gaemi reached the TS intensity. To investigate the role of large-scale circulation on the interactions between Gaemi and the Mei-Yu front, the filtering analysis would be implemented and discussed in the next section.

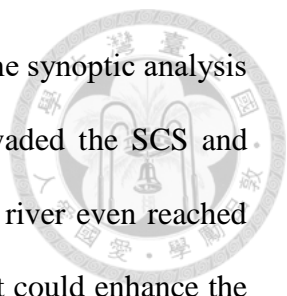
4.2 The analysis of large-scale circulation and case representativeness

The same as Chapter 3, the intraseasonal oscillation and synoptic evolution associated



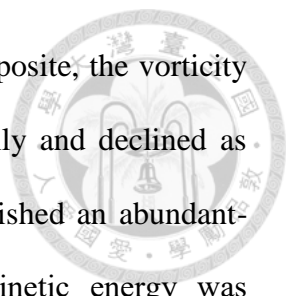
with Gaemi's formation were also analyzed via filtering analysis. The large-scale circulations of Gaemi was compared with the composite results. Firstly, the influences of the 30-90 days oscillations were examined (Figure 10a). The strong convection spanned from Indochina Peninsula to the SCS and the associated latent heat release could stimulate the cyclonic-vorticity anomaly and immense anomalous southwesterly flow in the SCS based on the Matsuno-Gill solution. The abundant low-level vorticity and vapor flux due to the intense southwesterly flow fertilized the enhancement of the Mei-Yu depression and Gaemi's formation in the SCS. Moreover, the signals of ERW were conspicuous as well. An anomaly originated from Western Pacific gradually strengthened and elongated when it propagated toward the SCS. The anomaly of southwesterly flow also intensified during this period. On the day when Gaemi intensified as a TS, the strong-convection, which elongated from Indochina Peninsula to Okinawa, covered the area ahead of the frontal and cyclogenesis region. The violent convective systems could enhance the Mei-Yu depression via the CISK and nourished Gaemi's cyclogenesis by convective aggregation. Furthermore, the intense anomaly of low-level vorticity strengthened the Mei-Yu depression and furnished the suitable environment for Gaemi's intensification. According to the above analyses, intraseasonal oscillations established a suitable environment to fertilize Gaemi's formation. Gaemi resembled the composite results in the aspect of intraseasonal oscillations.

In addition to the intraseasonal oscillations, the roles of the synoptic-scale circulation were also analyzed. At 850 hPa (Figure 11), a frontal depression formed in the Bushi Channel 144 hours prior to the TS formation and thence gradually deepened and moved northward. This frontal depression achieved the strongest intensity on the day when Gaemi developed into a TS. The frontal depression established a plentiful-vorticity environment



for Gaemi's cyclogenesis at the southwest end of this front. Moreover, the synoptic analysis also suggested that a robust atmospheric river from Indian Ocean invaded the SCS and Western Pacific (Figure 12). The almost whole portion of atmospheric river even reached the criteria of low-level jet in synoptic scale. Such a strong low-level jet could enhance the horizontal wind shear and vapor flux in frontal vicinity, which was able to trigger more fluctuations and convective systems along the Mei-Yu front. Furthermore, the mid-level trough system and baroclinicity were also considered. The mid-latitude trough located in the northern China 144 hours before Gaemi reached the TS intensity and gradually intensified afterwards (Figure 13a, b, c). This trough could help the formation of frontal system in the central China and East China Sea with the augmentation of thickness (temperature) gradient. Simultaneously, the low-level frontal depression also deepened (Figure 11 a, b, c). The frontogenesis was induced by the synoptic systems. The mid-latitude trough moved to Japan and started to weaken as Gaemi became a TS. The frontal depression also weakened at the same time. The environmental preferred frontolysis in this stage. Additionally, a warm-core, short-wave trough also formed and strengthened above the southwest end of Mei-Yu front prior to Gaemi developed into a TS (Figure 13 c, d). The vorticity advection was able to nourish the establishment of Gaimi's mid-level vortex to help Gaemi's formation. Similar to the composite result, the divergence at 200 hPa in SCS was obvious as well. The diffluent region above the SCS was in the west of Philippine 144 hours before Gaemi reached the TS intensity and gradually move northward. Hence, the high-level divergence region covered Gaemi and could enhance Gaemi's outflow. Consequently, the synoptic pattern furnished a suitable environment for Gaemi's formation.

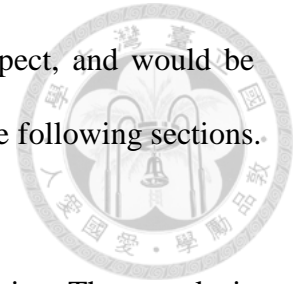
Evolution of the essential parameters was also evaluated in the upstream, cyclogenesis,



and frontal region, respectively (Figure 8b) as well. Similar to the composite, the vorticity in both the cyclogenesis region and frontal region strengthened initially and declined as Gaemi developed into a TS (Figure 8d). The frontal depression established an abundant-vorticity environment to fertilize Gaemi's cyclogenesis and the kinetic energy was transported from large-scale systems to vortex-scale systems after Gaemi reached the TS intensity. The vorticity in the frontal region also resembled the composite. It preferred frontogenesis that vorticity (horizontal deformation) enhanced prior to Gaemi's formation. The vorticity gradually reduced after Gaemi became a TS and may lead to frontolysis. Additionally, the vertical wind shear substantially intensified in all of the domains 24 hours before the time when Gaemi strengthened into a TS and obviously declined afterwards. The frontogenesis was nourished initially but later restrained. Moreover, the vertical wind shear, which restricted TC development, was also weakest in the cyclogenesis region (about 15m/s between 200 hPa and 850 hPa) during Gaemi's formation despite the fact that the vertical wind shear was also considerably greater than the typical value (10knots, Gray 1968) during TC formation in the northeastern Pacific. According to the analysis, Gaemi also resembled the composite in the synoptic aspect.

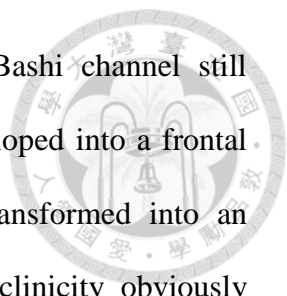
Consequently, the large-scale circulations fertilized Gaemi's cyclogenesis. The 30-90 days oscillations and the ERW triggered the strong southwesterly flow, abundant low-level vorticity and the aggregation of convection. Furthermore, the synoptic-scale systems nourished Gaemi's formation by strong atmospheric river, significant low-level vorticity, mid-level trough, high-level divergence and relative weak vertical wind shear. On the other hand, synoptic circulation favored frontogenesis in the frontal depression prior to Gaemi developed into TS but restrained frontogenesis afterwards. Moreover, Gaemi's formation

could represent the frontal-type formations in the large-circulation aspect, and would be utilized to explore the mechanisms of cyclogenesis and frontolysis in the following sections.



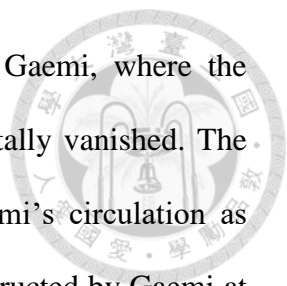
4.3 Local evolution

The large-scale circulation has been investigated in the previous section. The reanalysis data and satellite observation would be used to describe the local evolutions of Gaemi and the Mei-Yu front in this section. At 12 UTC 12 June, an obvious wind shear line (Mei-Yu front) extended from the southern China to Okinawa with significant temperature gradient and intense horizontal wind shear at 850 hPa (Figure 15a). A short-wave, warm-core trough was above the southwest end of the trough at 500 hPa (Figure 15c). Modulated by the large-scale circulation, the southwesterly flow was strong and the associated low-level convergence triggered active convection ahead of the front (Figure 15e). Moreover, it implied this Mei-Yu front was a weak baroclinic system that the axis of the low pressure did not obviously tilt and the short-wave trough was warm core. The mid-level warm core also indicated that this trough was not induced by baroclinic wave but might attribute to the convective heating. In the next 12 hours (00UTC 13 June), the frontogenesis was induced by a slight augment of temperature gradient and substantial intensification of horizontal wind shear (Figure 15b). The Mei-Yu depression deepened and the southwesterly flow intensified. Two mesoscale vortexes located in Guangdong and Bashi channel began to develop at the same time. These two vortexes might be triggered via barotropic instability (Kuo 1949; Kuo and Horng 1994; Ferreira and Schubert 1997) in an environment with violent horizontal wind shear. Simultaneously, the mid-level trough strengthened and still stayed in the same location. In addition, the stronger southwesterly furnished more vapor and induced more intense convergence to stimulate violent convection ahead of the front.



At 12UTC 13 June, the vortexes located in Guangdong and Bashi channel still intensified and move eastward (Figure 16c). The east one finally developed into a frontal vortex embedded in the Mei-Yu front. The west one, however, transformed into an equivalent barotropic, warm-core TD. Additionally, the frontal baroclinicity obviously declined but the frontal depression deepened. The abundant low-level vorticity and reduction of baroclinicity nourished TD intensification. On the other hand, the front was in frontolysis but the deformation strengthened simultaneously. The most possible mechanism contributing frontolysis was the diabatic heating which could offset the frontogenesis induced via the enhancement of deformation (Eq.4). Similar to the previous stage, the mid-level trough still intensified and remained in the same region (Figure 16a). The TD (west vortex) was totally covered by mid-level trough but the east vortex was located at the margin of this short-wave trough. Thus, the short-wave trough exerted different forcing on these two vortexes and might modulate their evolutions in different way. Moreover, the convection ahead of the front was more violent owing to more intense convergence. The location of a convective system, which developed with a nearly axisymmetric structure, was consistent to the location of TD (Figure 12e). Due to the considerable reduction of baroclinicity and the active convection, the CISK mechanism gradually dominated the frontal evolution after this stage (Chen et al. 2003).

Gaemi was categorized as a TS at 00UTC 15 June. Gaemi's warm-core structure and cyclonic circulation had been built at 850 hPa (Figure 16b). The northeasterly (southwesterly) flow in the west (east) side of Gaemi was strengthened by the Gaemi's circulation. The intense convergence was strengthened by the strong northeasterly (southwesterly) flow in the west (east) side of Gaemi and stimulated the alignment of



convection (Figure 12f). In addition, the front on the west side of Gaemi, where the temperature gradient and horizontal wind shear obviously declined, totally vanished. The frontal structure in southwestern section could be destructed by Gaemi's circulation as Gaemi formed. Simultaneously, the warm-core structure had been constructed by Gaemi at 500 hPa (Figure 12d). Although the closed isobars did not exist at this time, the mid-level circulation and temperature anomaly was obviously distinct from the short-wave trough. Gaemi still intensified and translated northeastward in the next 24 hours (00 UTC 16 June). The warm-core structure, cyclonic circulation and isolated isobars were established completely both at low level (Figure 13a) and middle level (Figure 13b) though the phases of temperature and geopotential height were slightly different. Hence, Gaemi had achieved its mature stages. Moreover, the horizontal wind shear and the baroclinicity substantially reduced in the west of Gaemi. The frontal structure had dissipated from the southern China to Taiwan after Gaemi passed. Only in the east of Gaemi can front preserve its structure. Furthermore, the convection also suggested the pattern of Gaemi and front (Figure 13c). The coverage of convection in the west side was far less than that in the east side.

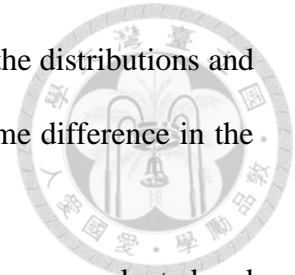
The evolution of weather systems was remarked in this section: Gaemi developed into a TC from a mesoscale vortex in a Mei-Yu frontal depression of which the baroclinicity gradually declined. This front experienced the frontogenesis prior to the time when the vortexes intensified but was in frontolysis as one vortex strengthened into a TD. The Mei-Yu front totally vanished where Gaemi passed. Additionally, a mid-level trough covered the cyclogenesis region. It was a quasi-stationary, warm-core system and differed from a fast-moving, cold-core baroclinic wave. According to the overview in this section, the essential processes from the CTL simulation were validated in the next section.

4.4 Model verification

A WRF simulation was performed to diagnose the important processes in the weather event and the overview in the previous section furnished the criteria for model verification. According to the case overview, there were some essential evolutions of the weather systems during Gaemi formation: the frontogenesis and frontolysis of the Mei-Yu front, Gaemi's cyclogenesis, and the distribution of short-wave trough at 500 hPa.

Figure 18, 19, 20, and 21 showed the comparison of the synoptic pattern in numerical simulation with the reanalysis data. At low level, the PV pattern was compared since the PV was supposed to be the critical parameter to uncover the interaction of Gaemi and the front. The CTL run can simulate the evolution of the PV band representing the front: the distortion when perturbation formed, the filamentation as Gaemi approached and the weakening after Gaemi passed. The CTL simulation also captured the behaviors of the robust PV center representing Gaemi, such as the location, size and strength. Additionally, the thickness between 500 and 850 hPa and the mid-level systems were investigated to confirm the thermal conditions. The warm advection associated with the atmospheric river and the short-wave trough above the southern China from the CTL simulation resembled the evolution in the reanalysis data. The CTL run also suggested the establishment of Gaemi's warm-core structure in the reanalysis data. Moreover, the local evolution of the front and cyclone was also examined (Figure 22,23). The CTL simulation was able to capture Gaemi's cyclogenesis: the warm-core establishment, the intensification of cyclonic circulation, and the pattern of isobars, even including the phase difference between the temperature and geopotential height. In general, the frontolysis process in the east of Gaemi at 850 hPa and the pattern of short-wave trough at 500 hPa from the CTL simulation was in

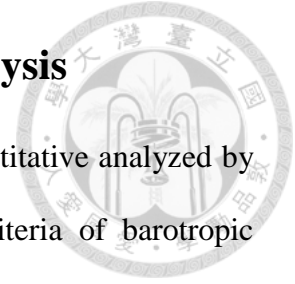
good agreement with the evolution in the reanalysis data. Furthermore, the distributions and the strength of convection were caught by the CTL simulation with some difference in the fine-resolution signatures.



In addition to the subjective validation, some important parameters were evaluated and compared with the reanalysis data. Firstly, TS's track from the CTL was shown in Figure 9a. The CTL captured the northeastward track and the approximate location although the TC's path in the CTL was slightly west and south to JMA's best track. Moreover, Figure 24 indicated that the CTL simulation suggested the bottom-up process in the vorticity aspect and mid-level vortex due to the short-wave trough in the PV aspect. Secondly, the frontal structure was validated with reanalysis data in the different stages as well. The temperature gradient was compared between reanalysis data and the CTL run prior to Gaemi's formation (Figure 25a, b). General speaking, the diabatic term dominated the variation of temperature gradient, which was consistent to the overview in Section 4.3. This front experienced the frontogenesis initially but started frontolysis afterwards. Furthermore, the stretching term and horizontal shear term contributed to little frontogenesis owing to the less baroclinicity. The tilting term mainly induced frontolysis in this period. After Gaemi formed, the baroclinicity had reduced considerably and the temperature gradient was difficult to elucidate the correlation between Gaemi and front. Only via the analysis of PV can front relate to Gaemi. The evolution of PV in the CTL resembled the trend in reanalysis data (Figure 25c): the PV obviously reduced when Gaemi approached to the analysis region.

The CTL run well simulated the weather systems based on the validation in this section. We could analyze the frontolysis and cyclogenesis process by the CTL simulation. In the next chapter, the possible mechanism remarked in Section 4.3 would be verified.

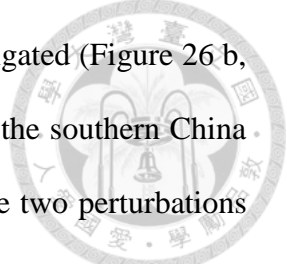
Chapter 5. Mechanisms of cyclogenesis and frontolysis



In this Chapter, the mechanism remarked in Section 4.3 were quantitative analyzed by the reanalysis data or WRF simulation. In the first section, the criteria of barotropic instability were quantitatively investigated. Later, the budget analysis was conducted to uncover the mechanisms of cyclogenesis and frontolysis in the second and third section, respectively. Moreover, the location of Gaemi's formation was close to Taiwan. Thus, the role of the steep topography in Taiwan were examined in the last section.

5.1 Barotropic instability

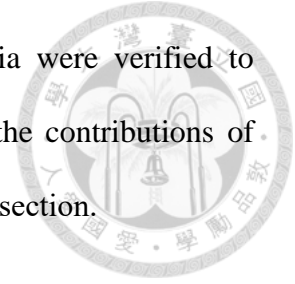
Kuo and Horng (1994) indicated the necessary conditions of barotropic instability. Firstly, the vorticity distributions must not be an omnidirectional monotonic function in which the perturbation cannot keep intensifying. Secondly, the wavelength of Rossby waves (PV waves) in both side of the shear zone exceeds 4.8-times width of this shear zone. Hence, these two PV waves can enhance each other via phase lock. Thirdly, the perturbation grows when this perturbation has "right" tilting direction (Figure 26a) to allow that the kinetic energy transported from background flow into the vortexes. Last, the substantial horizontal wind shear further nourishes the intensification of perturbations since the immense horizontal wind shear can not only fertilize the formation of PV waves but also furnish the kinetic energy from the environment. In the following analyses, we would subjectively compare the PV distributions with the conceptual model and objectively examine these necessary criteria. Moreover, the reanalysis data was used in this discussion. One of the reasons was that ERA5's resolution was sufficient to resolve this phenomenon. Second reason was that the PV distribution in WRF simulations would be complicated by the convective systems.



To begin with, the PV evolution at 850 hPa was subjectively investigated (Figure 26 b, c, d). An obvious PV band extended from the West Pacific Ocean into the southern China with enormous horizontal wind shear at 0600 UTC 13 June. There were two perturbations embedded in this PV band. Afterwards, both of the perturbations intensified and this PV band was distorted simultaneously. The PV distribution resembled the classic 4-layer conceptual model by Kuo and Horng (1994) (Figure 26a). The tilting directions were consistent to the conceptual model in which the perturbations were strengthened by the environmental kinetic energy. Thus, these two PV perturbations might be triggered via the barotropic instability. Moreover, the PV was not a monotonic function in the north-southward direction. Consequently, these perturbations were subjectively considered to be generated by the barotropic instability.

In addition, the ratio of the PV-wave wavelengths and the PV-band width was evaluated. Since the PV perturbations were intensified by the phase lock of PV waves, the distance between these two vortices were approximately the wavelength of PV waves if we assumed these vortices had similar translation velocity. Furthermore, the PV wave existed in the vicinity with substantial gradient of PV. We estimated the PV-band width as the shortest distance between two 0.6-PVU contours. We evaluated the ratio at 0900UTC 13 June owing to the more obvious PV perturbations but less filamentation of PV band. The PV-band width was about 80 km and PV-wave wavelength was about 540 km at this time. The wavelength was about 6.75, which was near the ratio of maximum-intensification rate (Kuo and Horng 1994). Hence, the ratio of PV-wave wavelength and PV-band width in this case agreed with the value evaluated from barotropic-instability theory indicated by Kuo and Horng (1994).

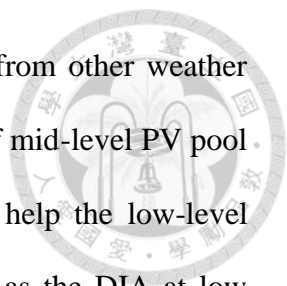
According to these analyses, the subjective and objective criteria were verified to confirm possibility of the barotropic instability. We would examine the contributions of several environmental systems during Gaemi's cyclogenesis in the next section.



5.2 Cyclogenesis process

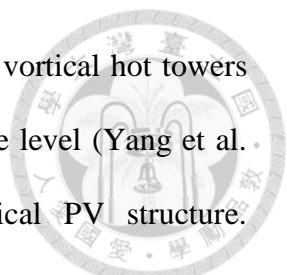
After the barotropic instability triggered the perturbations, the mesoscale vortex still strengthened. The contributions of environmental conditions were analyzed in PV aspect since the effects of diabatic heating and advection could be distinguished. General speaking, the mid-level PV pool and low-level PV center were established via the diabatic heating (hereafter DIA). The vertical advection (hereafter VAD) modulated the vertical structure during the TC formation. On the other hand, other system exerted their influence on cyclogenesis by the horizontal advection (hereafter HAD). The positive PV advection can improve the heating efficiency to enhance the cyclogenesis by DIA. In the following analysis, the PV budget was evaluated within 200km from Gaemi's center at 0200-0400 UTC 13 June (initial stage), 1100-1300 UTC 13 June (TD stage) and 2300 UTC 14 June – 0100 UTC 15 June (TS stage) (Figure 27, 28). The PV budget and the averaged strength of relative vorticity (Figure 24b) and PV (Figure 24d) were used to diagnose the forcing during Gaemi's cyclogenesis.

In Figure 24d, the most obvious signature was the mid-level PV pool, which formed much earlier than Gaemi's formation. The formation mechanism of PV pool was worth exploring since the mid-level PV pool was vital to TC formation (Raymond et al. 2011; Davis 2015). The heating profile in the initial stage (Figure 28b) showed that the maximum of diabatic heating was located at higher level (about 400 to 300 hPa), which agreed with the results proposed by Raymond et al (2011). However, the DIA had far less contribution



than the HAD at middle level (700-400 hPa). It implied the PV was from other weather systems at the same layer instead of latent heating. The intensification of mid-level PV pool can not only improve the heating efficiency at middle level but also help the low-level cyclogenesis afterwards. Moreover, the HAD has similar contribution as the DIA at low level (900-800 hPa), although the cyclogenesis was slightly offset by the VAD. This signature suggested that the perturbation was formed via the contributions of the DIA by convection and of the HAD from the nearby weather system (frontal depression). Actually, the intensification of perturbation by the barotropic instability was also through the horizontal advection. This result indirectly validated the role of barotropic instability. The low-level cyclogenesis fertilized the TC formation in the next stage due to the improvement of the heating efficiency. The vortical hot tower in the abundant-vorticity environment was able to concentrate the vorticity effortlessly as well.

As the Gaemi developed into a TD, the PV-budget structure (Figure 28c) and the heating profile (Figure 28d) substantially varied. At low level (below 700 hPa), the HAD almost had no contribution on cyclogenesis. It was supposed that the vortex had reached the upper-limit strength by the barotropic instability, because the barotropic instability cannot directly intensify the perturbation into a TD (Guinn and Schubert 1993). In other words, the barotropic instability was not able to enhance TD effectively. Gaemi's PV was not strong enough to organize the PV in the environment at this time, either. Therefore, contribution of the HAD was almost neglectable. Furthermore, modulated by the mature convection (Figure 22f), the maximum of diabatic heating shifted to middle level (one local maximum located at about 450 hPa and the other located at 600 hPa) (Raymond et al. 2011). The strong diabatic heating by the convection and cyclonic vorticity established in the previous



stage generated the substantial DIA. Moreover, the deep convection in vortical hot towers transported the PV (cyclonic vorticity) from the low level to the middle level (Yang et al. 2018). The VAD exerted strong influence to modulate the vertical PV structure. Additionally, the HAD even had negative contribution at 500 hPa, since Gaemi was located at the west of the trough axis at 500 hPa (Figure 27c). Only above 450hPa did the HAV have positive contribution. The VAD was responsible for the cyclogenesis from 700 to hPa to 500 hPa and the DIA also played some roles. Therefore, the VAD by convection and DIA by latent heating were the main terms at middle level.

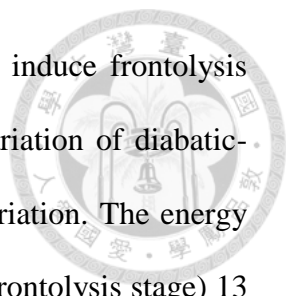
When Gaemi intensified as a TS, Gaemi had reached the mature stage (Section 4.3). Due to the more considerable mid-level diabatic heating (Figure 28f), the DIA was stronger in this stage than in the previous stage at low level (below 700 hPa) (Figure 28e). The active convection transported PV from low level to middle level. This heating profile and contributions of the DIA and VAD were typical in the mature stage of TC. Nevertheless, the HAD had larger contribution than DIA, which was uncommon in this stage. The substantial HAD implied that TC may be near a relative weak PV pool and this PV pool furnished the PV to this TC (Guinn and Schubert 1993). Based on the horizontal distribution of PV (Figure 25f), Gaemi was in a frontal depression and the distributions of PV was akin to the process that the strong PV center organized the weak PV. The frontal depression played the role as a PV pool and provided the PV to enhance PV via the HAD. Different from the previous stage, Gaemi's PV was strong enough to organize the plentiful environmental PV. Thus, HAD was tremendous at the mature stage and even larger the DIA. Although the mid-level (400-700 hPa) cyclogenesis was mainly attribute to DIA and VIA, HAD had some contribution as well, especially between 500 and 400 hPa.

Simultaneously, Gaemi was gradually separated from the short-wave trough and located in the east of its axis, where the trough could induce the positive HAD (Figure 27e). Gaemi's mid-level PV was also organizing the PV in the short-wave trough. Thus, HAD was able to enhance the mid-level cyclogenesis in this stage.

Accordingly, the environmental systems played different roles on Gaemi's cyclogenesis in different stages. In the initial stage, the mid-level trough and frontal depression induced the cyclogenesis via the HAD. The amount of the HAD was far greater than the DIA and VAD at middle level but resembled the DIA at low level. As Gaemi developed into a TD, the DIA dominated the cyclogenesis and the VAD transported the PV upward due to the sufficient heating efficiency and the development of convection. In addition, HAD was nearly ignorable since Gaemi's strength surpassed the upper limit that perturbation could still intensify via barotropic instability. Gaemi's PV was not strong enough to organize the environmental PV in this stage either. Gaemi's PV strengthened and convection was mature when Gaemi reached the TS stage. Thus, the DIA and VAD had more contributions. Nevertheless, the HAD was an important forcing as well because Gaemi's PV center was able to organize the environmental PV. Moreover, Gaemi's PV could also destroy the adjacent PV structure, such as the Mei-Yu front, based on this result. The frontolysis process would be analyzed in the next section.

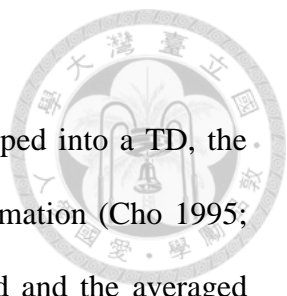
5.3 Frontolysis process

In addition to the cyclogenesis process, the frontolysis process was also investigated as well. The frontolysis was supposed to be the effect of the tilting and diabatic heating term before Gaemi's formation. The tilting terms almost induced the frontolysis and the frontogenesis by the diabatic heating obviously declined during this stage (Figure 25b). It



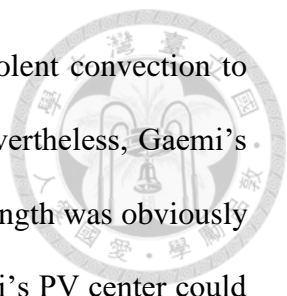
was well known that the thermally-direct secondary circulation could induce frontolysis through the tilting term (Colle et al. 2002). On the other hand, the variation of diabatic-heating effect was worthwhile to further analyze due to its obvious variation. The energy exchange on the surface at 00 UTC (frontogenesis stage) and 06 UTC (frontolysis stage) 13 June was analyzed to discuss the frontolysis mechanism since the diabatic heating from the surface (Figure 29a, b), which was the summation of the upward long-wave radiation, sensible and latent heat flux, possessed the good relation to the frontogenesis (frontolysis). At 00 UTC, the latent (Figure 29c) and sensible heat flux (Figure 29e) could not contribute the frontolysis since the latent and sensible heat flux ahead of the front was greater. The Mei-Yu front was a weak baroclinic system so that the temperature difference between the air and land (ocean) was less than the typical mid-latitude system and the frontolysis process was not induced by the transformation of the air-mass characteristic. The short-wave radiation was similar in the both side of the front due to pattern of the convection (Figure 30a). At 06 UTC, the sensible (Figure 29d) and latent heat flux (Figure 29f) in the rear of the front substantially augmented, which indicated the temperature gradient between air and land considerably increased during this period. We could speculate that the surface was heated since the Mei-Yu front was quasi-stationary (Figure 30a, b) and cold advection did not strengthen during this period (not shown). Additionally, the pattern of the downward short-wave radiation at surface (Figure 30d) suggested that the solar radiation mainly heated the rear of the front at this time, which could lead to the frontolysis. The evolution of short-wave radiation mainly attributed to the development of the convection that could block the solar radiation effectively (Figure 30a, b). Therefore, this result suggested that the heating by the short-wave radiation was responsible for the frontolysis

before Gaemi's formation.

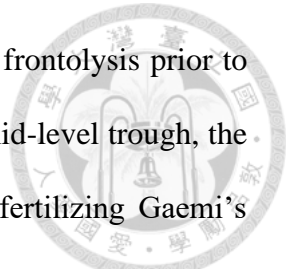


Although the temperature gradient declined prior to Gaemi developed into a TD, the frontal structure could be preserved by the intensification of the deformation (Cho 1995; Chen et al. 2003; 2008). The frontal depression significantly deepened and the averaged strength of deformation enormously augmented during Gaemi's formation. Why did frontal PV decline when Gaemi approach (Figure 25c)? To elucidate the physical mechanisms, the PV budget was implemented to explore the mechanisms which destroyed the PV structure in frontal region. According to the PV budget (Figure 31d), PV was maintained or even enhanced by the DIA. This result suggested that the frontal convection (diabatic process) was the essential mechanism to induce frontogenesis in PV aspect (Chen et al. 2003). The VAD, which induced by the strong convergence at low level, only played a secondary role in this process. Moreover, the HAD had strong negative contribution throughout the analysis period. It implied that PV was removed out from the frontal region via horizontal wind, such as the robust southwesterly flow ahead of front. We could further distinguish the frontogenesis /frontolysis into 3 stages to elucidate the mechanism of frontolysis based on the evolution of PV budget. In the first stage (prior to 17 UTC 14 June), the front experienced slightly frontogenesis with the significant enhancement of the DIA and VAD. It showed that diabatic heating strengthened (Figure 31e) during this stage. Although the negative contribution of the HAD augmented when Gaemi's gradually approached and intensified, the amount was not enough to induce frontolysis.

The frontolysis by the HAD and the frontogenesis by the DIA substantially strengthened in a short time as Gaemi approached (Figure 31b) in the next stage (17 UTC 14 June to 01 UTC 15 June). Since Gaemi's cyclonic PV could enhance the southwesterly



flow ahead of the front, the strong low-level convergence triggered violent convection to strengthen the diabatic heating (Figure 31e) and DIA (Figure 31d). Nevertheless, Gaemi's PV could induce frontolysis via another mechanism. The frontal-PV strength was obviously weaker than Gami at this time since Gaemi reached the TS stage. Gaemi's PV center could distort the frontal PV and pump it out from the frontal region via the HAD. This result was consistent with the PV budget of Gaemi in the TS stage (Figure 28e). Figure 31d showed that the amount of the HAD declined after 22UTC 14 June. Gaemi reached the margin of analysis domain at this time. The positive PV tendency ahead of Gaemi (Wang et al. 2009) was able to compensate some negative contribution of the HAD. After 02 UTC 15 June (third stage), the abrupt reduction of DIA directly led to a significant frontolysis. Simultaneously, the averaged diabatic heating rate (Figure 31e) and vertical velocity considerably declined as well. This evolution suggested that the frontal convection was significantly weakened. According to Emanuel (1986), the descend motion around TC was an essential part of the TC secondary circulation in the energy aspect. Frank (1977) validated the existence of descent by composite analysis as well. Moreover, the vertical velocity (Figure 31f) from the diagnose of Sawyer-Eliassen equation suggested that the obvious descent (0.5 Pa/s, which was near the amount of the averaged ascent in the frontal region) associated with Gaemi's secondary circulation distributed about from 600 km to 1500 km. The range of the significant descent agreed with the longest distance from the east side of the frontal analysis domain to Gaemi after 02 UTC 15 June. Hence, the persistent descent around Gaemi was able to restrain the ascent in the frontal region to constrain development of convective systems. The reduction of latent heat release with the relative inactive convection could contribute to the less DIA to induce frontolysis.

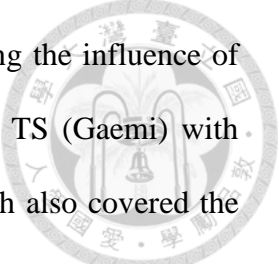


Consequently, the variation of solar radiation on surface led to the frontolysis prior to Gaemi formed. In addition to the abundant low-level vorticity and the mid-level trough, the reduction of baroclinicity helped to establish a suitable environment fertilizing Gaemi's formation at the southwest end of the front depression as well. After Gaemi formed and intensified, Gaemi's PV center was able to distort the environmental PV and destruct the Mei-Yu front. The frontal PV was pumped out from the frontal region and the efficiency of CISK was restricted. Moreover, Gaemi's secondary circulation restrain the frontal convection to reduce the diabatic heating. Reduction of the DIA further enhanced the frontolysis. Hence, TC Gaemi could destroy the frontal structure and induce that the Mei-Yu front vanished after Gaemi passed.

5.4 The role of Taiwan topography

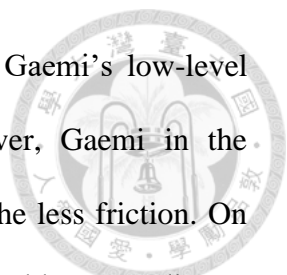
In previous analysis, we verified that the contributions of the front and the mid-level trough for Gaemi's cyclogenesis. Gaemi induced frontolysis process after Gaemi formed. The role of the topography in Taiwan was not discussed. However, Gaemi and front were adjacent to Taiwan, where the mountain ranges were steep but obviously smaller than synoptic scale. The steep terrain in Taiwan was able to locally affect Gaemi's cyclogenesis and evolution of the Mei-Yu front. Thus, a sensitivity experiment without Taiwan topography was implemented to examine the topography effect (hereafter Noterrain experiment). In this experiment, the sea-level height was set as zero in Taiwan and the other settings was the same as the CTL run.

The synoptic evolution after 12 UTC 13 June for Noterrain experiment was shown in Figure 32 to compare with the CTL simulation (Figure 18 to 21). The synoptic pattern at 00 UTC 13 June was not compared because the model started to simulate without nudging



after 21 UTC 12 June. The model should spend several hours amplifying the influence of Taiwan terrain. Resembling the CTL run, the vortex developed into a TS (Gaemi) with similar intensity and location. An obvious short-wave, warm-core trough also covered the location of Gaemi's formation. After Gaemi formed, the frontal PV was distorted and declined when Gaemi approached. It showed the frontolysis in the west of Gaemi that the baroclinicity (gradient of thickness) and PV reduced. The slight difference between the CTL and Noterrain simulations in synoptic scale suggested that Taiwan topography exerted the ignorable impacts on synoptic-scale systems due to the small horizontal scale. Taiwan terrain could only affect the system's evolution with similar scale, such as vortex-scale process. Therefore, Gaemi's formation in Noterrain was analyzed. Figure 9a showed Gaemi's path from the CTL and Noterrain runs. The path from the Noterrain run resembled the CTL path since the synoptic circulation was the main forcing to steer TC. Nevertheless, there were some differences in Gaemi's path and strength between the CTL and Noterrain simulations after Gaemi approached Taiwan. Additionally, Gaemi in the Noterrain run was cyclogenesis via bottom-up process (Figure 31a) and a mid-level PV pool formed prior to Gaemi's formation (Figure 31b) as well. Gaemi in the Noterrain experiment intensified faster at low level (below 850 hPa) than CTL prior to 00UTC 15 June owing to the reduced friction without the topography.

The evolution in the local view was examined as Gaemi was near Taiwan (Figure34). At 12 UTC 13 June, Gaemi in the Noterrain run located in the east of Guangdong, which is slightly west to that in the CTL but with similar strength (Figure 34c). The location and strength of convection in the Noterrain experiment also resembled the CTL run (Figure 34e). At 00 UTC 15 June, Gaemi moved to the southern Taiwan. Gaemi's location in the



Noterrain simulation was slightly north to that in the CTL run since Gaemi's low-level circulation was not block by Taiwan terrain (Figure 32d). Moreover, Gaemi in the Noterrain run was stronger with more organized convection owing to the less friction. On the contrary, the difference of Gaemi's strength at middle level was ignorable. According to the PV analysis in Section 5.2 (Figure 28e), the short-wave trough, which was larger than Taiwan in horizontal scale and higher than Taiwan topography, contributed obviously to the intensification of the mid-level cyclone. Thus, the mid-level cyclogenesis was almost not influenced by Taiwan terrain.

Consequently, Taiwan topography could affect the local, low-level weather systems, such as Gaemi's low-level circulation and path when it approached Taiwan. Nevertheless, the influence on synoptic system was ignorable due to the small horizontal scale of Taiwan terrain. The mid-level trough, frontal structure and convection ahead of front was similar to those in the CTL simulation since they were mainly modulated by synoptic evolution. Hence, the process of Gaemi's formation in the Noterrain experiment also resembled that in the CTL run owing to the similar synoptic environment and the fast translation, which allowed Gaemi to stay for a short time near Taiwan. Therefore, Taiwan topography was not the deceive forcing in this case.

Chapter 6. Discussion



6.1 The representativeness of Gaemi (2018)

The case study of Gaemi (2018) was implemented to analyze the vortex-scale processes of the frontal-type TC formations. How much mechanisms of the interactions between Gaemi and the Mei-Yu front can be introduced to elucidate the other frontal-type cases? The scales of these mechanisms should be the key to answer this question. If the processes were mainly modulated by the synoptic-scale systems shown in the filtering analysis, they could also play the similar role on the other frontal-type TC formations. By contrary, the mechanisms induced by the convective-scale systems, which was more random and unpredictable, might not be critical in the different cases. We would deploy this opinion to discuss the generality of these cyclogenesis and frontolysis mechanisms.

Firstly, the barotropic instability triggered the perturbations along the wind-shear line in the frontal region with strong horizontal wind shear induced by the strong southwesterly flow, which reached the intensity of low-level jet (12m/s) in the synoptic scale. Although the temporal scale of barotropic instability (several hours) was far less than synoptic scale (8 days in this study), the southwesterly flow could be resolved in the filtering analysis. The intense atmospheric river could enhance the horizontal wind shear and cyclonic vorticity in the frontal depression to furnish a suitable environment for the barotropic instability. Therefore, the barotropic instability could probably stimulate the perturbation in the other cases. Secondly, the frontolysis mechanism prior to Gaemi's formation was induced by the convection ahead of the front. The convection was more random and different in every case so that the distribution of the convective systems might not lead to frontolysis in the other cases. Other forcing, for example the latent heat flux in the PBL, might contribute the

reduction of the baroclinicity in the other frontal-type TC formations.

Thirdly, the frontal depression was able to nourish the development of the TCs in the other frontal-type TC formations due the obvious signals of the frontal depression in the composite filtering analysis. The intensification of the Mei-Yu depression prior to TC formation generated abundant low-level vorticity, which was the most critical parameter affecting TC formation. The energy cascade process in the frontal depression also indicated that the synoptic-scale systems still exert their influence on TC even after TC formation. The transportation of vorticity (PV) was also implied that the PV was removed from the synoptic-scale system (Mei-Yu front), which could lead to frontolysis. Moreover, the PV axisymmetric process was a well-known mechanism when a strong PV center was adjacent to a weak PV pool. This process was mainly modulated by the slow-manifold circulation, which was predictable. Thus, the contribution of the frontal depression to TC cyclogenesis in the other cases more probably resembled the mechanisms in Gaemi. The process of the frontolysis after TC formation in the other cases could be similar to in Gaemi as well. In addition, the warm-core, short-wave trough was also in the west of the location of TC formation in both of the composite and Gaemi's filtering analysis. It indicated this short-wave trough could help the establishment of the mid-level trough in other cases.

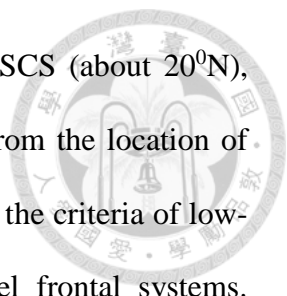
Consequently, some mechanisms uncovered in Gaemi's case study could be the critical processes in the other frontal-type TC formations as well if these processes were modulated by the large-scale circulation due to the similar evolution. On the other hand, there was no evidence suggested that the mechanisms dominated by convective-scale systems must work in the other cases.

6.2 The comparison between Gaemi (2018) and Diana (1984)

In this study, Gaemi (2018)'s formation, which formed in a weak baroclinic environment, was analyzed comprehensively in previous chapters. One scientific question was worth discussing: Are there the similarity and difference between Gaemi (2018) and Diana (1984), a famous Atlantic hurricane formed in the baroclinic environment? To elucidate the fundamental properties about these two frontal-type TC formations, we would compare and contrast them based on previous studies (Bosart and Bartlo 1991; Davis and Bosart 2001; 2002; 2003).

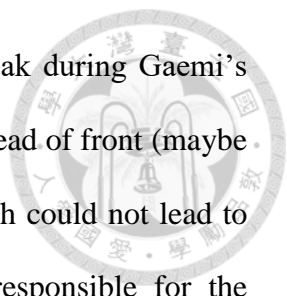
Both Gaemi and Diana formed in the southwest end of a front, where the baroclinicity was relative weak. The strong convergence and plentiful vapor flux in frontal region triggered the active convection. These convective systems released substantial latent heating in the middle level to contribute the cyclogenesis at low level in the PV aspect. Moreover, the frontolysis with the reduction of baroclinicity was also a common signature. If the baroclinicity didn't reduce, Gaemi and Diana would developed in to a frontal vortex or even a mid-latitude cyclone. In this process, the energy sources of the cyclones were transformed from baroclinic instability into latent heating. Simultaneously, the front started frontolysis and the cyclone was detached from the front. This transformation of baroclinicity was a vital process of Diana's and Gaemi's formation.

Nevertheless, Gaemi's and Diana's formations had distinct developments due to the difference of baroclinicity, which can be validated by the comparison of gradient of temperature and thickness between 500 to 1000 hPa (or 850 hPa). Firstly, Diana formed in a higher-latitude region (about 30⁰N) with relative strong baroclinicity. The strong northwesterly flow guided by the mid-latitude system dominated the evolution of the low-



level frontal systems. By contrast, Gaemi formed in the northeastern SCS (about 20⁰N), where the baroclinicity was weaker. The mid-latitude trough was far from the location of Gaemi's formation (Figure 13). The robust southwesterly flow (reached the criteria of low-level jet in synoptic scale) dominated the evolution of the low-level frontal systems. Secondly, the stratosphere air invaded the upper troposphere prior to Diana's formation. The tropopause folding generated a positive PV anomaly and contributed to the ascent at the middle troposphere via the positive PV advection at higher level. This ascend motion triggered the active convection in the frontal region and the latent heating by these convective systems further enhanced the low-level cyclogenesis. The forcing modulating cyclogenesis was mainly from upper-troposphere system during Diana's formation, which was confirmed by the sensitive experiment. In the contrast, there was no evidence to suggest that the stratosphere air invaded troposphere during Gaemi's cyclogenesis (Figure 35). The low-level perturbation was triggered via the barotropic instability and nourished Gaemi's intensification by PV in the frontal depression. The mid-level trough only helped the establishment of mid-level PV pool to improve the efficiency of the low-level vorticity concentrating. Accordingly, the forcing inducing Gaemi's formation was mainly from the low-level systems.

In addition, the frontolysis process was different between Diana and Gaemi as well. The latent heat flux and sensible heat flux in the PBL contributed the reduction of baroclinicity during Diana's formation owing to the conspicuous temperature difference between the atmosphere and ocean, which resembles the transformation process of the air mass. The latent heat release in Diana's convection further help itself transform from a mid-latitude, baroclinic system to a tropical, equivalent barotropic system. However, since



the temperature difference between the atmosphere and ocean was weak during Gaemi's formation, the latent heat and sensible heat fluxes were even stronger ahead of front (maybe associated with the stronger southwesterly flow) above the ocean, which could not lead to frontolysis. The different heating of the short-wave radiation was responsible for the frontolysis due to the blocking by the convection ahead of the front prior to the Gaemi's formation. After Gaemi intensified as a TC, Gaemi's PV and secondary circulation restrained the CISK to further induce frontolysis.

Although Diana and Gaemi experienced the transformation of baroclinicity during formation, the formation processes were different in terms of baroclinicity for these two cases. Thus, the mechanism for Gaemi's formation differed from Diana's formation.

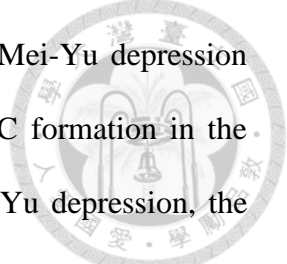
Chapter 7. Conclusions and Future Research Routes



7.1 Conclusions

In this study, the 14 frontal-type TC formations during 1979-2018 were identified based on the criteria proposed by Lee et al. (2006) to show the typical properties and the generalized signatures of frontal-type TC formation. According to the statistical results, the averaged location of frontal-type TC formation was in the northeast SCS. Steered by the southwesterly flow, the averaged motion of these TC cases was northeastward.

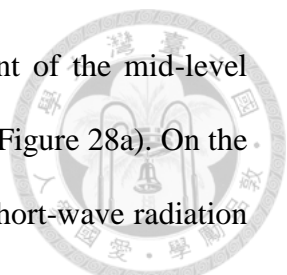
The filtering analyses of the frontal-type TC formations were composited to elucidate the associated large-scale circulation as well. Firstly, the composite results suggested that the active phase of 30-90 days oscillations was correlated to the frontal-type TC formations. In the active phase, the southwesterly flow and the low-level cyclonic vorticity over the SCS was enhanced by the convective-heating anomaly over the Indochina Peninsula. Both the plentiful vapor flux by the anomalous southwesterly flow and the abundant low-level cyclonic vorticity could nourish the TC formations in the SCS. Secondly, the composite results also suggested the association of the ERW, which was able to strengthen the southwesterly flow and cyclonic vorticity as well. Moreover, the convection anomaly of the ERW could directly induce the violent convection in the frontal region, which further fueled the development of the severe systems. Last, modulated by intraseasonal oscillation, the synoptic-scale evolution furnished a suitable environment for TC formation. In the northeast SCS, TC formations were fertilized by the strong southwesterly flow, abundant low-level cyclonic vorticity, the mid-level trough, conspicuous high-level divergence. Although the vertical wind shear was considerably stronger than the typical value as TCs formed in the northwestern Pacific, the vertical wind shear in the southwest end of the Mei-



Yu depression was less than in the adjacent vicinity. In addition, the Mei-Yu depression preferred frontogenesis prior to TC formations but frontolysis after TC formation in the aspect of vorticity and vertical wind shear. Similar to the whole Mei-Yu depression, the vorticity in the cyclogenesis area (the southwest end of the front) reduced after the TC formed. The reduction of environmental kinetic energy with the augmentation in vortex scale suggested the energy cascade in this stage, which implied the frontal-type TC was still influenced by synoptic environment obviously after TC formation.

To further uncover the vortex-scale process of frontal-type TC formation and the mesoscale evolution of the Mei-Yu front, Typhoon Gaemi (2018) was chosen to perform the case study. To begin, the evolution of Gaemi was described and some essential processes were summarized: Gaemi's formation and intensification, the frontolysis prior to Gaemi's formation and the frontolysis in the region where Gaemi had passed. The WRF simulation used for the diagnosis was validated for these processes to assure that the simulation was able to capture the important evolution. Additionally, the background circulations in different spatial and temporal scales were investigated. Akin to the composite results, large-scale environment nourished TC formation in the southwest end of front. The frontal depression preferred the frontogenesis prior to Gaemi's formation but frontolysis afterwards in the synoptic aspects. Gaemi's representativeness was confirmed by the comparison with composite as well.

Last, a conceptual model (Figure 36) was proposed to elucidate the mechanisms of cyclogenesis and frontolysis. Prior to Gaemi's formation (Figure 36a), the strong horizontal wind shear triggered that the vortexes formed along the Mei-Yu front via the barotropic instability. The frontal PV also fueled the intensification of the perturbations (Figure 28a).

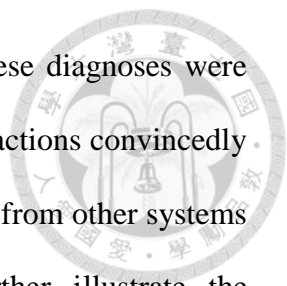


Moreover, the mid-level trough furnished PV to help the establishment of the mid-level vortex, which was able to improve the efficiency of bottom-up process (Figure 28a). On the other hand, the frontolysis was induced by the different heating of the short-wave radiation prior to Gaemi's formation (Figure 30). The baroclinicity in the frontal depression declined in this stage, which could further nourish Gaemi's formation. The CISK mechanism could gradually dominate the evolution of the Mei-Yu front owing to the reduction of the baroclinicity. After Gaemi intensified as a TS (Figure 36b), the Mei-Yu front played the role as a PV pools furnishing PV to strengthen averaged low-level PV in Gaemi's center (Figure 28e). On the contrary, Gaemi's PV center could distort and pump out the frontal PV to restrict the efficiency of the CISK. Gaemi's secondary circulation was able to restrain the frontal convection to constrain the diabatic heating in frontal region (Figure 31). Hence, Mei-Yu front totally vanished after Gaemi passed. Furthermore, the PV concentrating remarked in this conceptual model indicated Gaemi was persistently influenced by the strong synoptic-scale forcing (Mei-Yu front) and agreed with the energy cascade shown in the synoptic analysis. The kinetic energy (PV) of the synoptic-scales systems (Mei-Yu front) was transported to the vortex-scale system (Gaemi).

Through the comprehensive diagnosis, this study not only uncovered the frontal-type TC formation in different temporal and spatial scales but also elucidated the interactions between the TC cyclogenesis and the front.

7.2 Future work

This study has indicated the fundamental properties of frontal-type TC formations. The large-scale circulations of frontal-type formations were diagnosed comprehensively by the filtering and composite analysis. The cyclogenesis and the frontolysis processes were

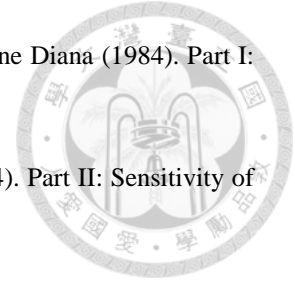


illustrated through a case study, Typhoon Gaemi (2018). Although these diagnoses were able to answer some scientific questions, they cannot elucidate the interactions convincingly since the diagnosis cannot distinguish the signals of one weather system from other systems directly. Thus, the sensitivity experiments were necessary to further illustrate the interactions between different systems as well. In the future, one can implement the sensitivity experiment via the piecewise PV inversion to remove the PV patches of Gaemi, the front, and the mid-level trough, respectively. These experiments may suggest that the direct contribution to frontolysis by TC, the influence of the front, and the mid-level trough on Gaemi's cyclogenesis. Moreover, we invoked other papers (Gray 1968; 1975; 1979; Fu et al.2012; Chen et al. 2018) to confirm the role of the larger-scale circulations. In the future, the influence of the large-scale circulation and the “threshold” of the important synoptic parameters for frontal-type TC formation can be further verified by the comparison between the frontal-type TC and the frontal-vortex in the Mei-Yu front, which did not develop into TC. Based on the comparison results, the sensitive experiment can be also performed by removing or changing the specific large-scale circulations to examine the role of the large-scale systems and the “threshold” of these synoptic conditions.



Reference

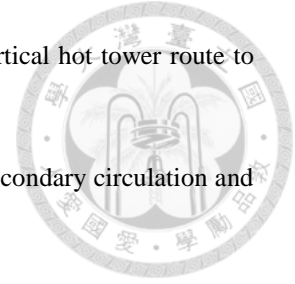
- Bosart, L. F., and J. A. Bartlo, 1991: Tropical storm formation in a baroclinic environment. *Mon. Wea. Rev.*, **119**, 1979–2013.
- Charney, J. G., 1947: The dynamics of long waves in a baroclinic westerly current, *J. Atmos. Sci.*, **4**(5), 136–162.
- Charney, J. G., and Eliassen, A., 1964: On the Growth of the Hurricane Depression, *J. Atmos. Sci.*, **21**(1), 68–75.
- Chen, G. T.-J., and C.-P. Chang, 1980: The structure and vorticity budget of an early summer monsoon trough (mei-yu) over southeastern China and Japan. *Mon. Wea. Rev.*, **108**, 942–953
- , and C. C. Yu, 1988: Study of low-level jet and extremely heavy rainfall over northern Taiwan in the mei-yu season. *Mon. Wea. Rev.*, **116**, 884–891.
- , Wang, C., and Liu, S. C., 2003: Potential Vorticity Diagnostics of a Mei-Yu Front Case, *Mon. Wea. Rev.*, **131**(11), 2680–2696.
- , —, and Chang, S., 2008: A Diagnostic Case Study of Mei-yu Frontogenesis and Development of Wavelike Frontal Disturbances in the Subtropical Environment, *Mon. Wea. Rev.*, **136**(1), 41–61.
- Chen, J.-M., C.-H. Wu, P.-H. Chung, and C.-H. Sui, 2018: Influence of intraseasonal-interannual oscillations on tropical cyclone genesis in the Western North Pacific. *J. Clim.*, **31**, 4949–4961.
- , P.-H. Lin, C.-H. Wu, and C.-H. Sui, 2020: Track variability of South China Sea-formed tropical cyclones modulated by seasonal and intraseasonal circulations. *Terr. Atmos. Ocean. Sci.*, **31**, 239–259.
- Cho, H. R., and G. T. J. Chen, 1995: Mei-Yu frontogenesis. *J. Atmos. Sci.*, **52**, 2109–2120.
- Chou, M.-D. and Suarez, M.J., 1999: A Solar Radiation Parameterization (CLIRAD-SW) Developed at Goddard Climate and Radiation Branch for Atmospheric Studies. *NASA Technical Memorandum* NASA/TM-1999-104606.
- , M. J. Suarez, X. Z. Liang, and M. M.-H. Yan, 2003: A thermal infrared radiation parameterization for atmospheric studies. *NASA Tech. Rep.* NASA/TM-2001-104606, Vol. **19**, 56 pp.
- Colle, B. A., B. F. Smull, and M.-J. Yang, 2002: Numerical simulations of a landfalling cold front observed during COAST: Rapid evolution and responsible mechanisms. *Mon. Wea. Rev.*, **130** · 1945–1966.



- Davis, C. A., and L. F. Bosart, 2001: Numerical simulations of the genesis of hurricane Diana (1984). Part I: Control simulation. *Mon. Wea. Rev.*, **129**, 1859–1881.
- , and ——, 2002: Numerical simulations of the genesis of hurricane Diana (1984). Part II: Sensitivity of track and intensity prediction. *Mon. Wea. Rev.*, **130**, 1100–1124.
- , and ——, 2003: Baroclinically induced tropical cyclogenesis. *Mon. Wea. Rev.*, **131**, 2730–2747.
- , 2015: The Formation of Moist Vortices and Tropical Cyclones in Idealized Simulations, *J. Atmos. Sci.*, **72**(9), 3499-3516.
- Eliassen, A., 1962: On the vertical circulation in frontal zones. *Geophys. Publ.*, **24**, 147–160.
- Emanuel, K. A., 1986: An air-sea interaction theory for tropical cyclones. Part I: Steady-state maintenance. *J. Atmos. Sci.*, **43**, 585–605
- Ertel, H., 1942: "Über hydrodynamische Wirbel"atze. *Physik. Z. (Leipzig)*, **43**, S. 526–529.
- Ferreira, R. N., and Schubert, W. H., 1997: Barotropic Aspects of ITCZ Breakdown, *J. Atmos. Sci.*, **54**(2), 261-285.
- Frank, W. M., 1977: The Structure and Energetics of the Tropical Cyclone I. Storm Structure, *Mon. Wea. Rev.*, **105**(9), 1119-1135.
- Fu, B., Peng, M. S., Li, T., and Stevens, D. E., 2012: Developing versus Nondeveloping Disturbances for Tropical Cyclone Formation. Part II: Western North Pacific, *Mon. Wea. Rev.*, **140**(4), 1067-1080.
- Gill, A.E., 1980: Some simple solutions for heat-induced tropical circulation. *Q.J.R. Meteorol. Soc.*, **106**, 447-462.
- Gray, W. M., 1968: Global View of the Origin of Tropical Disturbances and Storms, *Mon. Wea. Rev.*, **96**(10), 669-700.
- , 1975: Tropical cyclone genesis. *Dept. of Atmos. Sci. Paper No. 234*, Colo. State Univ., Ft. Collins, CO, 121 pp.
- , 1979: Hurricanes: their formation, structure and likely role in the tropical circulation. Supplement of Meteorology Over the Tropical Oceans. Published by RMS, James Glaisher House, Grenville Place, Bracknell, Berkshire, *RG 12 1BX, D. B. Shaw*, ed., 155-218.
- , 1998: The formation of tropical cyclones. *Meteorol. Atmos. Phys.* **67**, 37–69
- Guinn, T. A., and W. H. Schubert, 1993: Hurricane spiral bands. *J. Atmos. Sci.* **50**,3380-3403.



- Hendricks, E. A., M. T. Montgomery, and C. A. Davis, 2004: The role of“vortical” hot towers in the formation of tropical cyclone Diana (1984), *J. Atmos. Sci.*, **61**, 1209–1232.
- , Peng, M. S., Fu, B., and Li, T., 2010: Quantifying Environmental Control on Tropical Cyclone Intensity Change, *Mon. Wea. Rev.*, **138**(8), 3243-3271.
- Holton, J. R., 2004: *An Introduction to Dynamic Meteorology*. 4th ed. Academic Press, 683-535 pp.
- Hong, S., and Pan, H., 1996: Nonlocal Boundary Layer Vertical Diffusion in a Medium-Range Forecast Model, *Mon. Wea. Rev.*, **124**(10), 2322-2339.
- Hoskins, B. J., M. E. McIntyre, and A. W. Robertson, 1985: On the use and significance of isentropic potential vorticity maps. *Quart. J. Roy. Meteor. Soc.*, **111**, 877–946.
- Kikuchi, K., and Wang, B., 2009: Global Perspective of the Quasi-Biweekly Oscillation, *J. Clim.*, **22**(6), 1340-1359.
- Kuo, H., 1949: Dynamic Instability of Two-Dimensional Nondivergent flow in a Barotropic Atmosphere, *J. Atmos. Sci.*, **6**(2), 105-122.
- Kuo, H.-C. and C.-H. Horng, 1994: A Study of Finite Amplitude Barotropic Instability. *Terr. Atmos. Ocean. Sci.*, **5**, 199-243.
- Kuo, Y. H., and R. A. Anthes, 1982: Numerical simulation of a Mei-Yu system over southeastern Asia. *Pap. Meteor. Res.*, **5**, 15–36.
- Lee, C., Y. Lin, and K. K. W. Cheung, 2006: Tropical Cyclone Formations in the South China Sea Associated with the Mei-Yu Front. *Mon. Wea. Rev.*, **134**, 2670–2687.
- , —— and C. -M. Huang, 2008: Tropical Cyclone Formations in the South China Sea. Paper presented at the 28th Conference on Hurricanes and Tropical Meteorology, 28 April - 2 May, Florida
- Lim, K. S., and Hong, S. 2010: Development of an Effective Double-Moment Cloud Microphysics Scheme with Prognostic Cloud Condensation Nuclei (CCN) for Weather and Climate Models, *Mon. Wea. Rev.*, **138**(5), 1587-1612.
- Matsumoto, S., 1972: Unbalanced low-level jet and solenoidal circulation associated with heavy rainfalls. *J. Meteor. Soc. Japan*, **50**, 194–203.
- Matsuno, T., 1966 Quasi-geostrophic motions in the equatorial area, *J. Met. Soc. Japan*, **44**, 25–43.
- Miller, J. E., 1948: On the concept of frontogenesis. *J. Meteor.*, **5**, 169–171.



- Montgomery, M. T., Nicholls, M. E., Cram, T. A., and Saunders, A. B., 2006: A vortical hot tower route to tropical cyclogenesis. *J. Atmos. Sci.*, **63**(1), 355–386.
- Montgomery, M. T., and J. Persing, 2021: Does balance dynamics well capture the secondary circulation and spinup of a simulated hurricane? *J. Atmos. Sci.*, **78**, 75-95.
- Newell, R. E., N. E. Newell, Y. Zhu, and C. Scott, 1992: Tropospheric rivers? A pilot study, *Geophys. Res. Lett.*, **19**, 2401-2404
- Petterssen, S. and Smebye, J. 1971. On the development of extratropical cyclones. *Q J R Meteorol. Soc.* **97**, 457–482.
- Raymond, S. L. Sessions, and C. Lopez Carrillo, 2011: Thermodynamics of tropical cyclogenesis in the northwest Pacific. *J. Geophys. Res.*, **116**, D18101.
- Sawyer, J.S., 1956: The vertical circulation at meteorological fronts and its relation to frontogenesis. *Proc. Roy. Soc. London*, **A234**, 346-362.
- Schubert, W. H., C. M. Rozoff, J. L. Vigh, B. D. McNoldy, and J. P. Kossin, 2007: On the distribution of subsidence in the hurricane eye. *Q. J. Roy. Meteor. Soc.*, **133**, 710–715.
- Skamarock, W. C., Klemp, J. B., Dudhia, J., Gill, D. O., Barker, D., Duda, M. G., ... Powers, J. G. 2008: A Description of the Advanced Research WRF Version 3 (No. NCAR/TN-475+STR). *University Corporation for Atmospheric Research*.
- Smith, L.M. and Waleffe, F., 1999: Transfer of energy to two-dimensional large scales in forced, rotating three-dimensional turbulence. *Phys. Fluids* **11** (6), 1608–1622.
- Stauffer, D. R., and Seaman, N. L. 1990: Use of Four-Dimensional Data Assimilation in a Limited-Area Mesoscale Model. Part I: Experiments with Synoptic-Scale Data, *Mon. Wea. Rev.*, **118**(6), 1250-1277.
- Wang, C.-C., H.-C. Kuo, Y.-H. Chen, H.-L. Huang, C.-H. Chung, and K. Tsuboki, 2012: Effects of asymmetric latent heating on typhoon movement crossing Taiwan: The case of Morakot (2009) with extreme rainfall. *J. Atmos. Sci.*, **69**, 3172-3196.
- Wei S.-W., and M.-J. Yang, 2015: The Composite Study for Typhoons with Extreme Rainfalls on Taiwan. *Atmos. Sci.*, **43**, 233-264. (in Chinese with English abstract)
- Wheeler, M., and Kiladis, G. N., 1999: Convectively Coupled Equatorial Waves: Analysis of Clouds and Temperature in the Wavenumber–Frequency Domain, *J. Atmos. Sci.*, **56**(3), 374-399.

——, —— and Webster, P. J., 2000: Large-Scale Dynamical Fields Associated with Convectively Coupled Equatorial Waves, *J. Atmos. Sci.*, **57**(5), 613-640.

Yang, M., Wu, Y., and Liou, Y., 2018: The Study of Inland Eyewall Reformation of Typhoon Fanapi (2010) Using Numerical Experiments and Vorticity Budget Analysis. *J. Geophys. Res.*, **123**, 9604-9623.

Zeng, W., Chen, G., Du, Y., & Wen, Z., 2019: Diurnal Variations of Low-Level Winds and Precipitation Response to Large-Scale Circulations during a Heavy Rainfall Event, *Mon. Wea. Rev.*, **147**(11), 3981-4004.

Zhu, Y., & Newell, R. E., 1994: Atmospheric rivers and bombs. *Geophys. Res. Lett.*, **21**, 1999–2002.

Hersbach, H., Bell, B., Berrisford, P., Biavati, G., Horányi, A., Muñoz Sabater, J., Nicolas, J., Peubey, C., Radu, R., Rozum, I., Schepers, D., Simmons, A., Soci, C., Dee, D., and Thépaut, J-N., 2018: ERA5 hourly data on pressure levels from 1979 to present.

Himawari 8/9 gridded data are distributed by Center for Environmental Remote Sensing (CERES), Chiba University, Japan.

Tables



Table 1. The frontal-type TC formations during 1979 to 2018

Year	Tropical cyclone	Year	Tropical cyclone
2018	Gaemi	1997	Levi
2014	Hagibis	1994	Russ
2014	Mitag	1988	Susan
2012	Talim	1987	Ruth
2004	Conson	1986	Mac
2002	Noguri	1982	Skip
2000	Longwang	1981	Ike

Table 2. The criteria of MJO (BSISO), ERW, and synoptic systems for filtering analysis

Phenomena	Temporal scale	Spatial scale	Duration
MJO (BSISO)	30~90 days	0~5 wave number	180 days
ERW	10~45 days	-1~-14 wave number	180 days
Synoptic and larger scale systems (or simply synoptic)	> 8 days	None	40 days

Table 3. Model description for CTL

Terms	Settings
Version	WRF 3.9
Grid size	18 km - 6 km – 2 km
Simulation time	00 UTC, 12 June 2018 – 00UTC, 16 June 2018
Nudging	21 hours (coefficient 4-2-1 ($10^{-4} s^{-1}$))
Time step	30 s
Vertical levels	60 (the lowest eta level is 0.9985)
Model top	20 hPa
Microphysics scheme	WDM6
Cumulus scheme	Grell 3D (for d01)
PBL scheme	YSU
Damping	W_damp

Figures

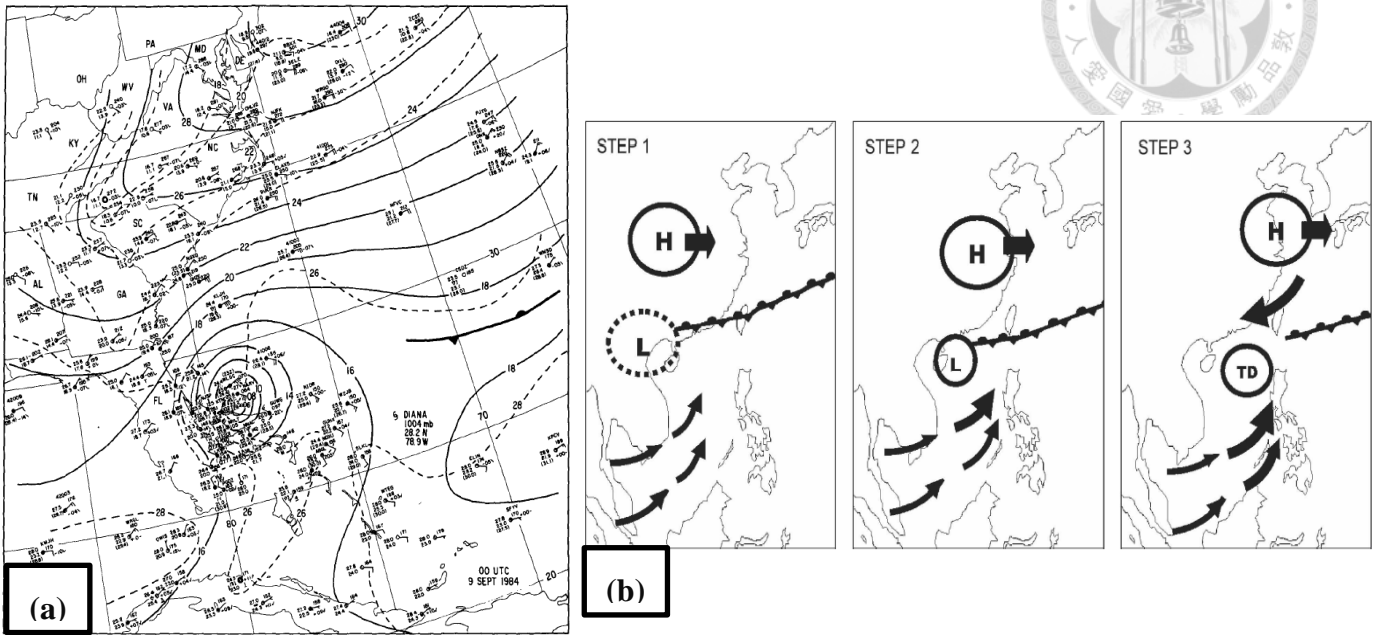


Figure 1. Figures from other studies: (a) Diana (1984)’s formation (Bosart and Bartlo 1991)
 (b) The conceptual model of frontal-type formation (Lee et al. 2006)

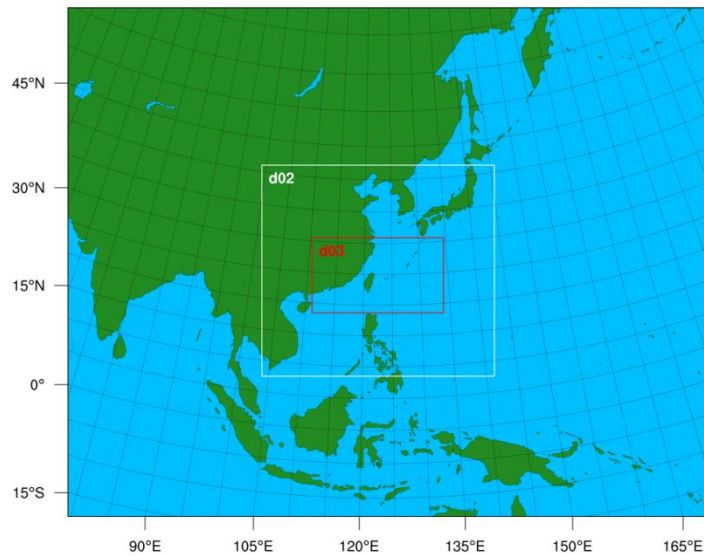


Figure 2. The WRF simulation domain. The grid sizes of D01, D02 and D03 are 18, 6 and 2km, respectively.

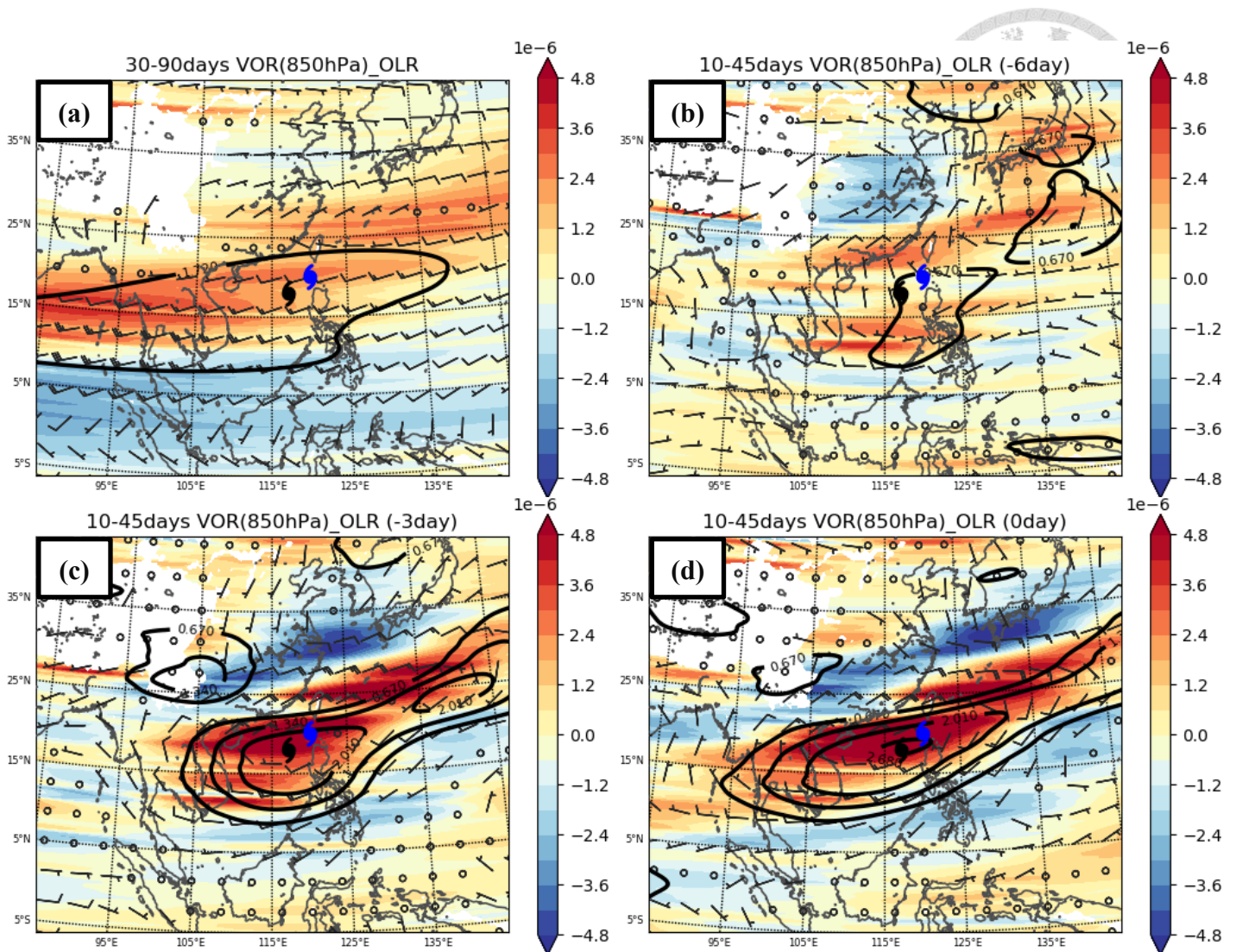


Figure 3. The averaged circulation of the intraseasonal oscillation associated with frontal-type TC formation. The barbs, color, and contour are wind anomaly (m/s), vorticity anomaly (s^{-1}), and OLR anomaly, respectively. The wind anomaly was 10 times of the actual value. The OLR was only plotted in the strong convection region, where the amount of OLR anomaly was larger than one standard deviation of the whole domain in these period. (a) is the environmental conditions associated with 30-90 days oscillations averaged from 6 days prior to the date when the TSs formed. (b) is the environmental conditions associated with 10-45 days oscillation 6 days prior to the TSs formation. (c) is the same as (b) but 3 days prior to TS formation. (d) is the same as (b) but is on the day as TS formed.

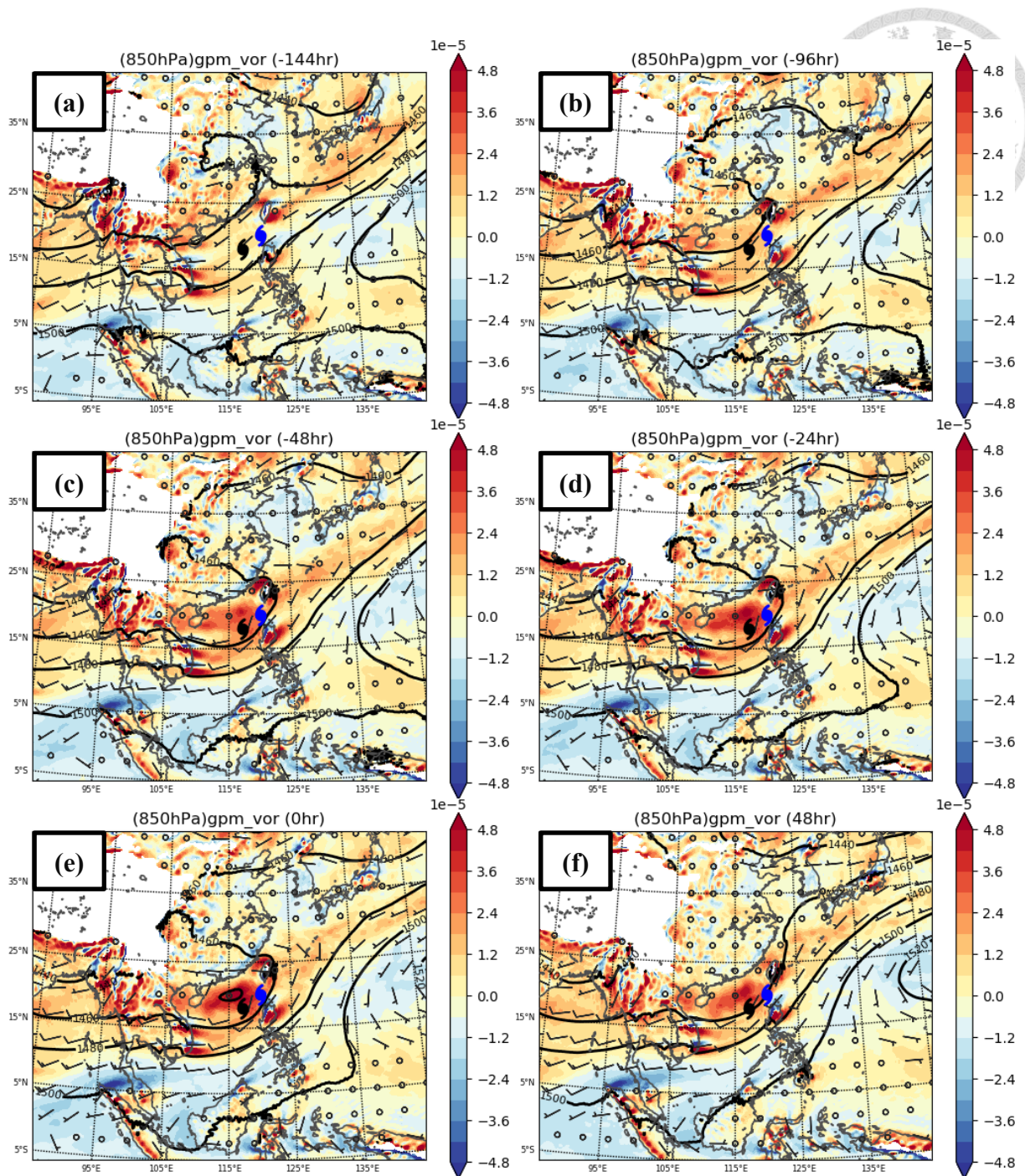


Figure 4. The composite of the synoptic-scale circulations at 850 hPa. The contour, color and barbs are geopotential height(m), relative vorticity (s^{-1}) and wind (m/s), respectively. The black TC symbols mark the averaged locations of TD formation and the blue ones represent those for TS formation. The time was relative to the TS formation time.

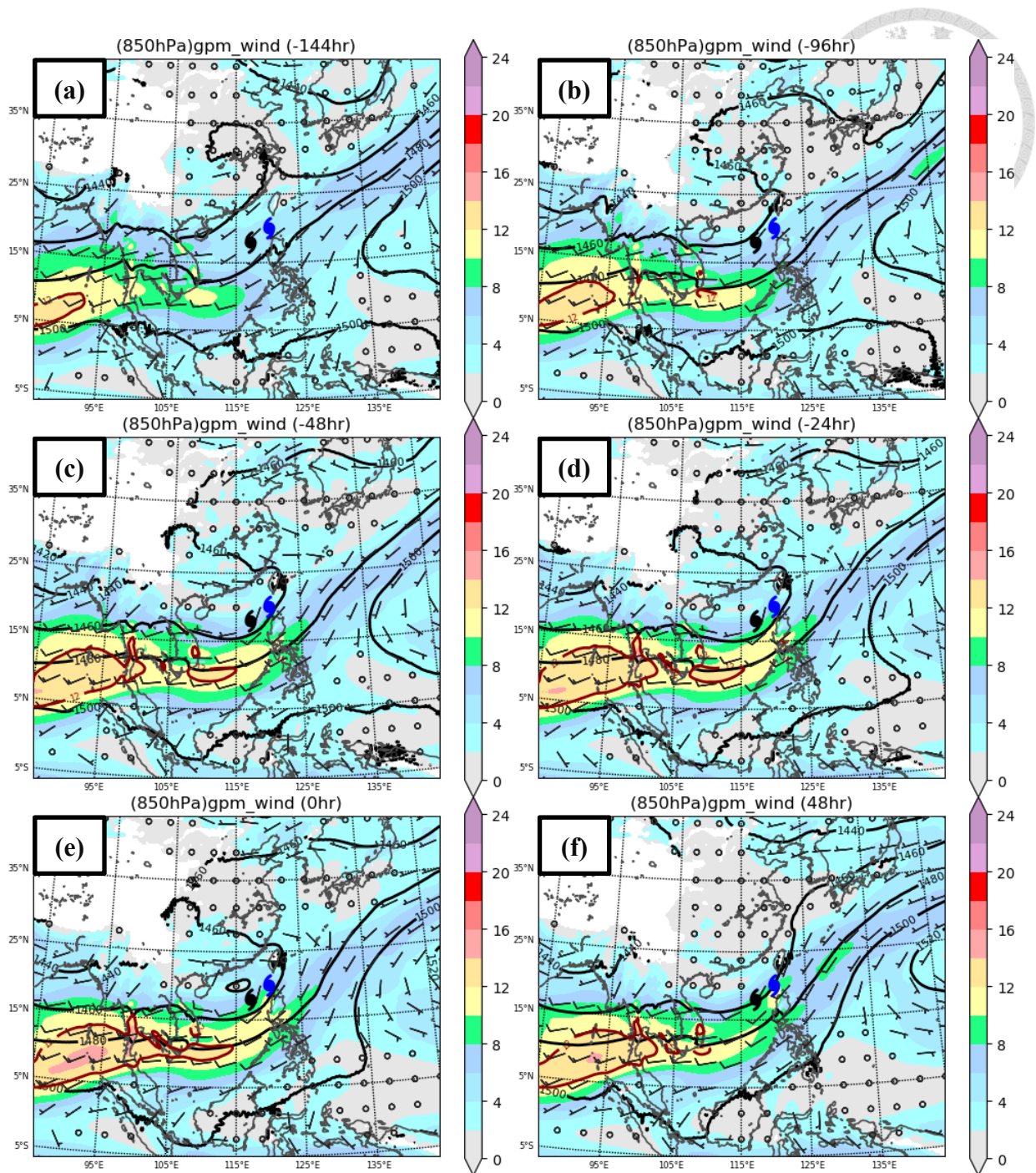


Figure 5. The composite of the synoptic-scale evolutions at 850 hPa. The contour, color and barbs are geopotential height (m), wind velocity (m/s) and wind (m/s), respectively. The location of the low-level jet (wind speed > 12 m/s) was highlighted by red contour. The black TC symbols mark the averaged locations of TD formation and the blue ones represent those for TS formation. The time was relative to the TS formation time.

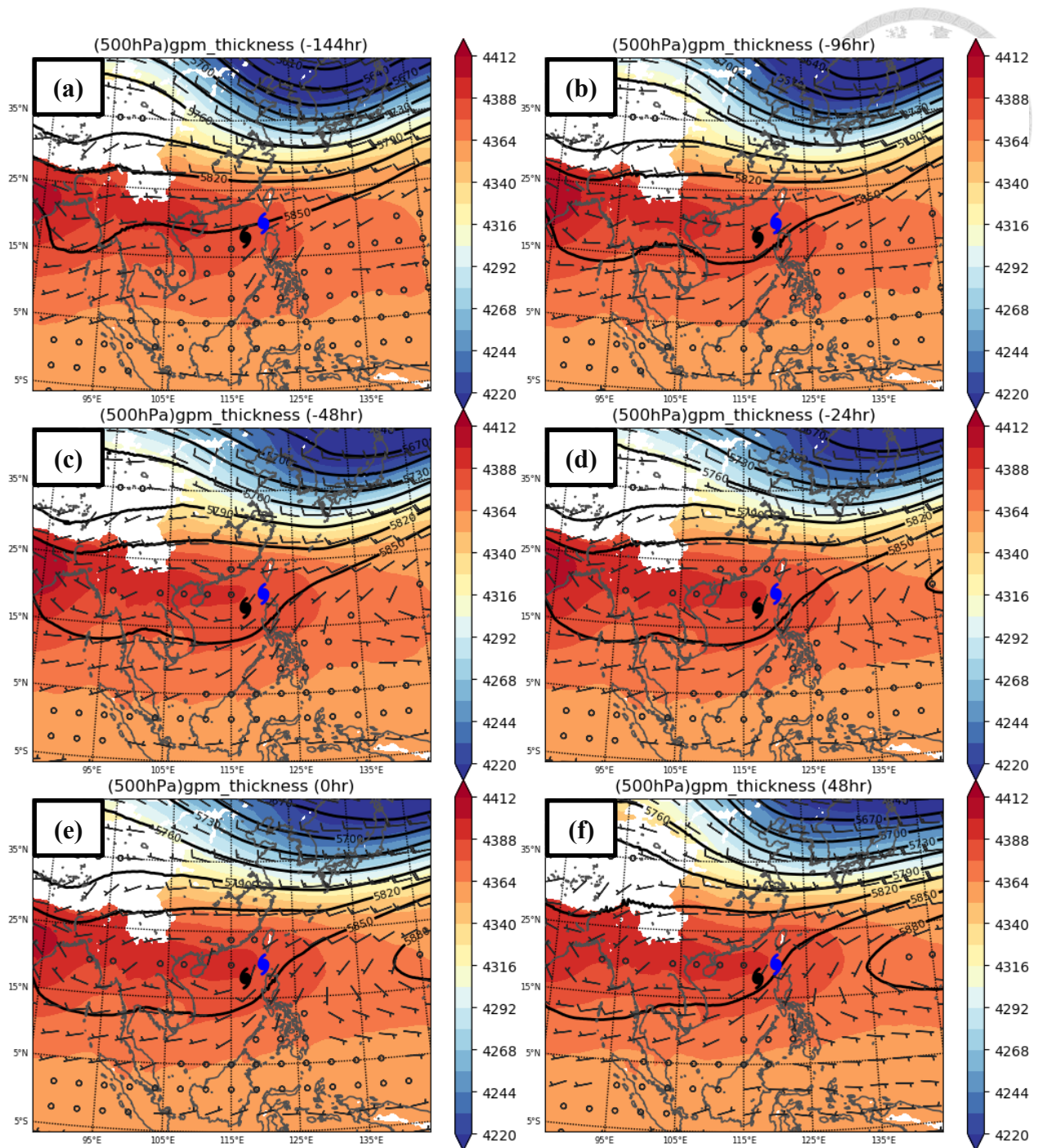


Figure 6. The composite of the synoptic-scale circulation at 500 hPa. The contour and barbs represent geopotential height (m) and wind (m/s), respectively. The color is thickness between 850 hPa and 500 hPa (m). The black TC symbols mark the averaged locations of TD formation and the blue ones represent those for TS formation. The time was relative to the TS formation time.

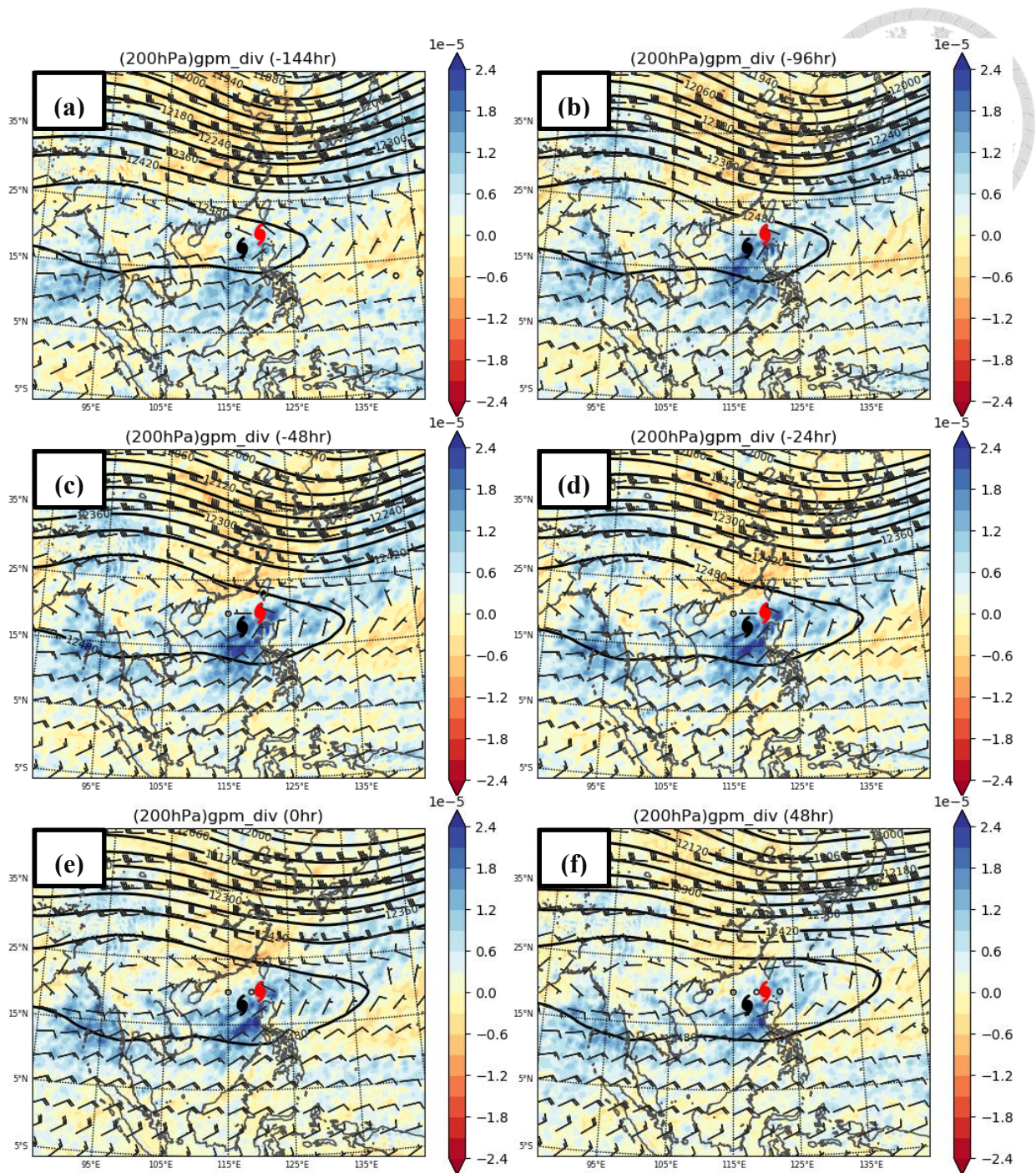


Figure 7. The composite of the synoptic-scale circulation at 200 hPa. The color (s^{-1}), contour (m) and barbs (m/s) are divergence, geopotential height and wind, respectively. The black TC symbols mark the averaged locations of TD formation and the red ones represent those for TS formation. The time was relative to the TS formation time.

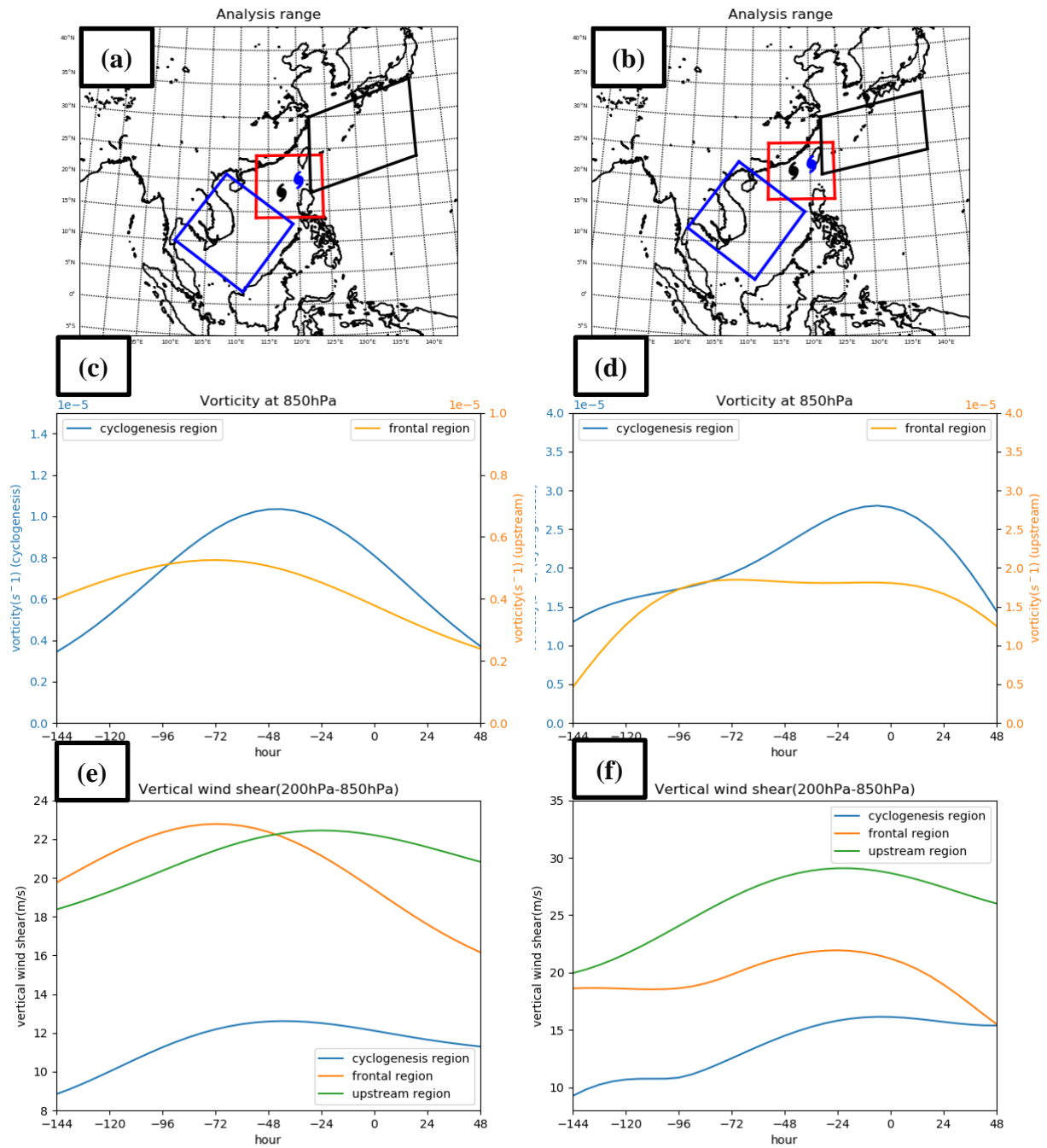
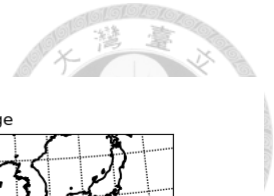


Figure 8. The evaluation of synoptic-scale vorticity (s^{-1}) and vertical wind shear (m/s). (a) is the calculation domain for composite, which was defined based on Figure 4. (c) is 850-hPa vorticity in the frontal and cyclogenesis regions. (e) is the variation of the vertical wind shear. (b), (d) and (f) are the same as (a), (c) and (e) but only from TC Gaemi (2018).

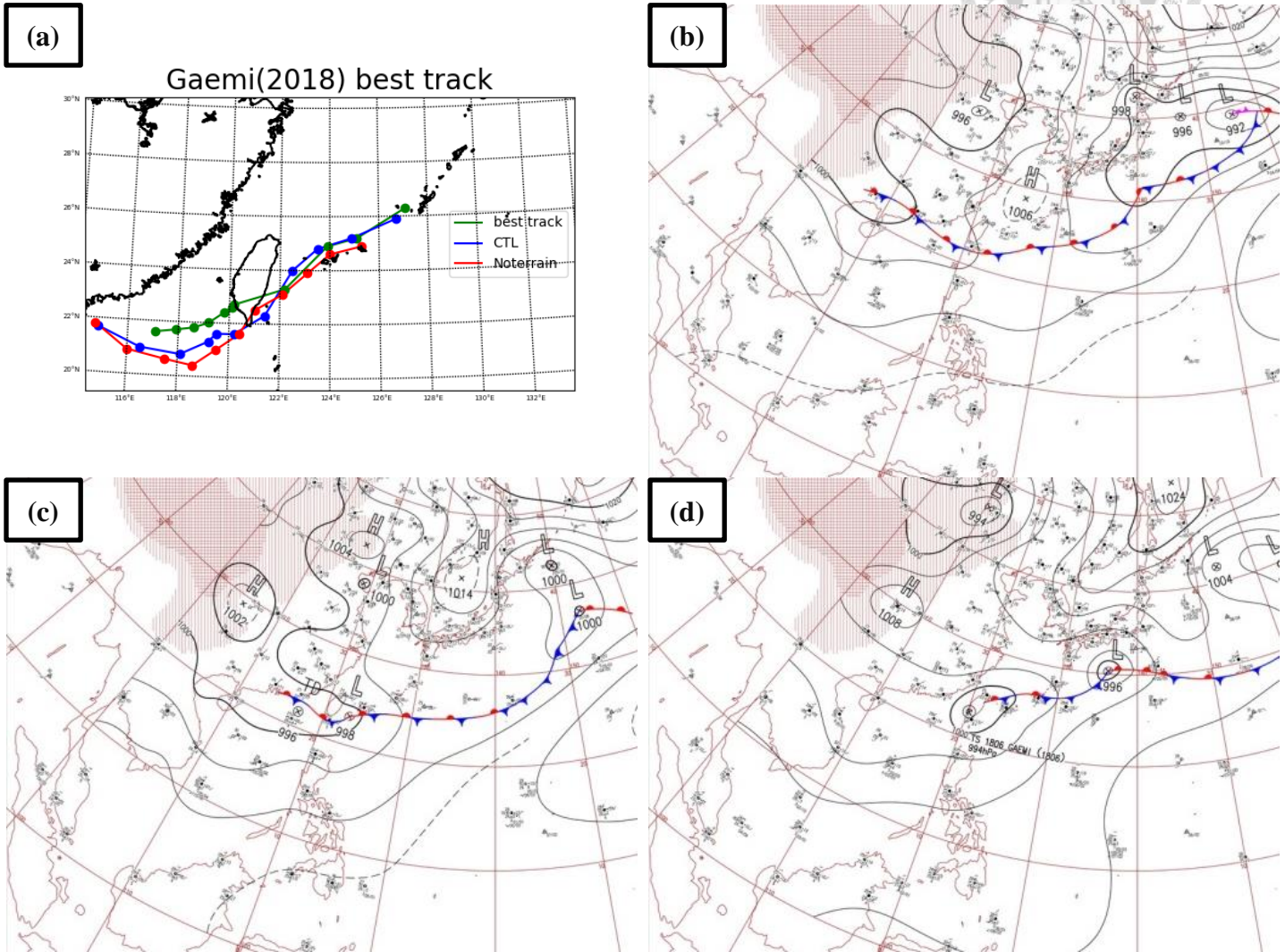


Figure 9. Gaemi's tracks and the analyses from the JMA. (a) Gaemi's tracks from the JMA, control run (CTL) and sensitive experiment without Taiwan topography (Noterrain) during Gaemi's formation. (b), (c) and (d) are the JMA weather maps at 12 UTC 12 June, 12 UTC 13 June and 00 UTC 15 June, respectively.

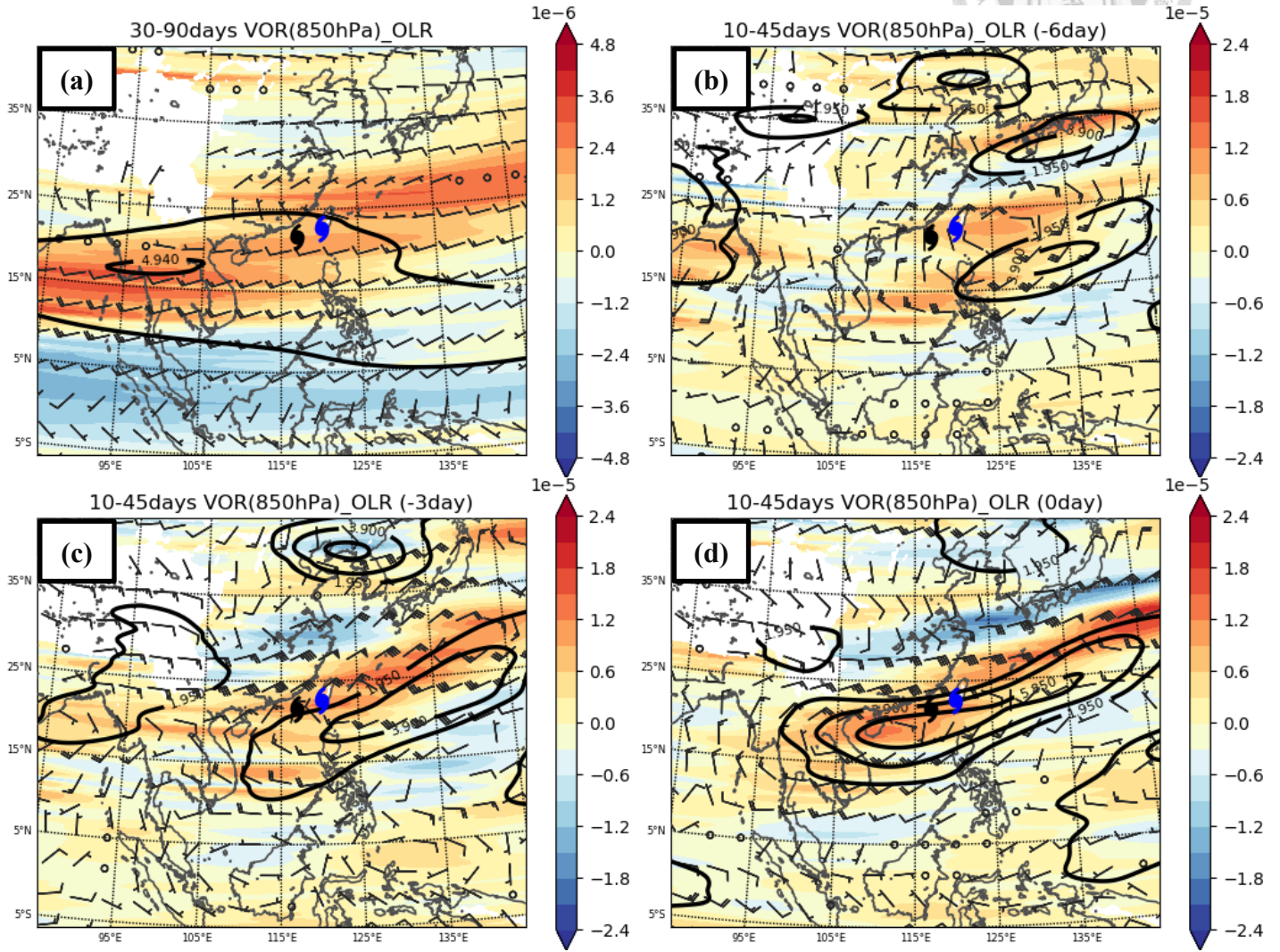


Figure 10. Same as Figure 3 except for the case study of TC Gaemi (2018).

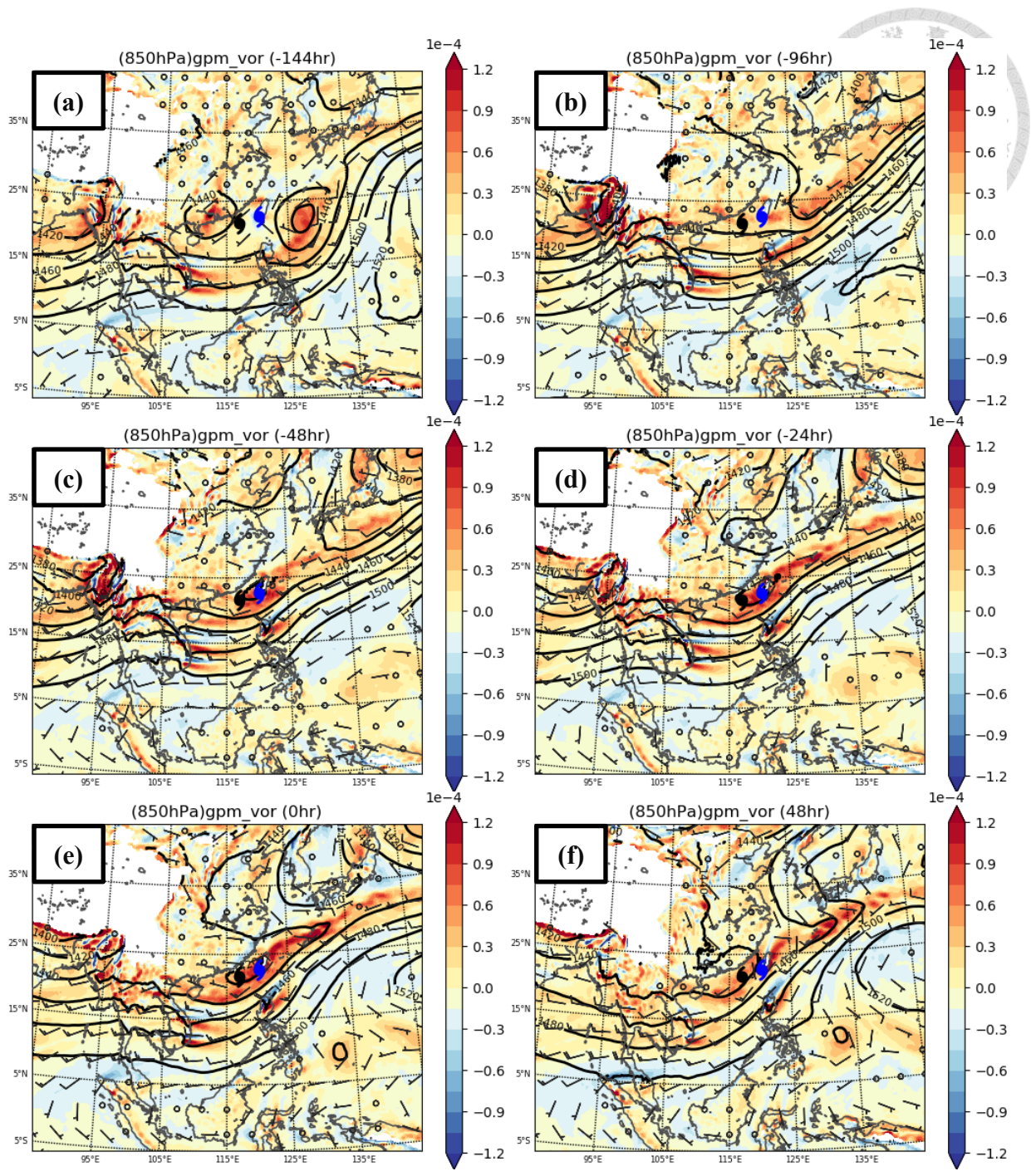


Figure 11. Same as Figure 4 except for the case study of TC Gaemi (2018).

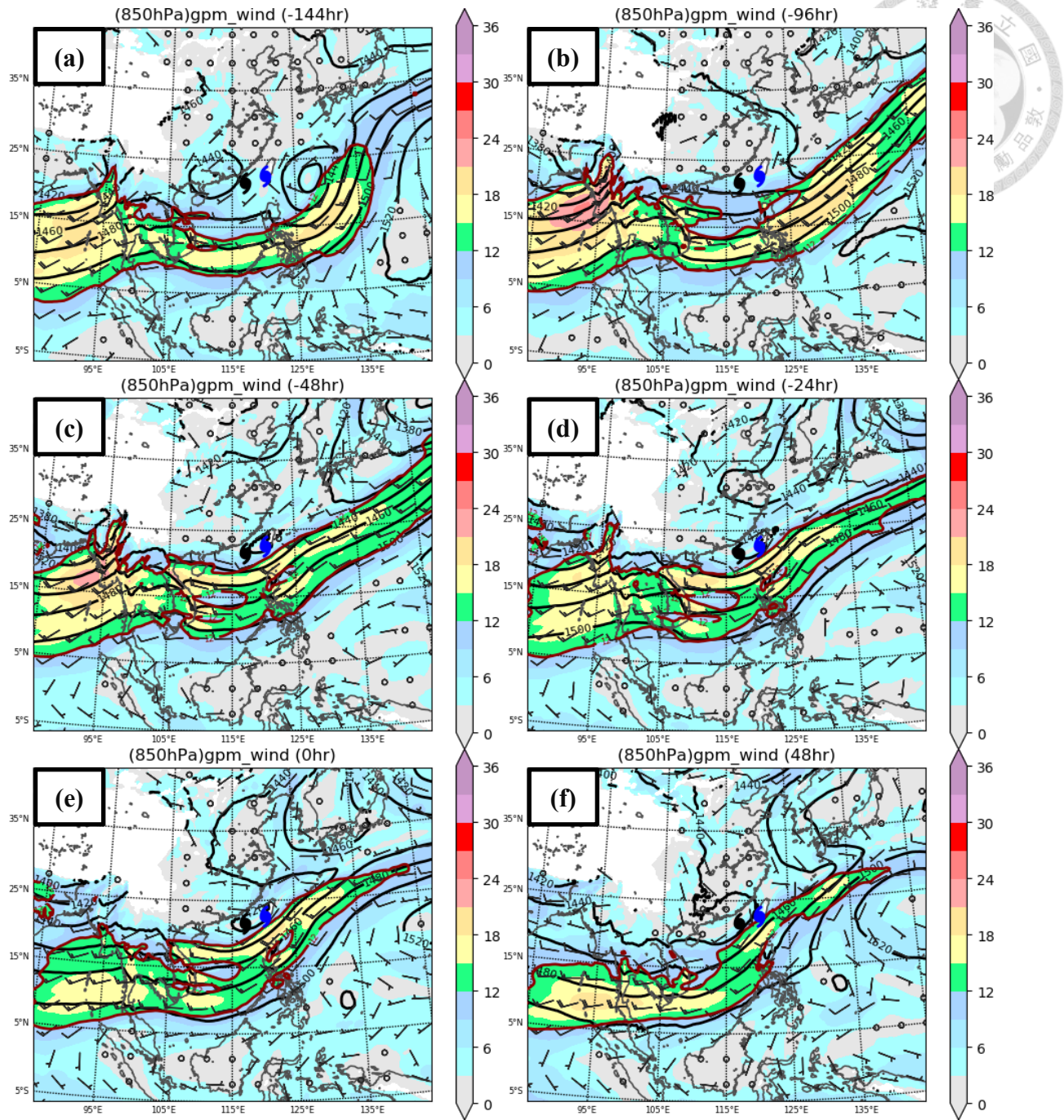


Figure 12. Same as Figure 5 except for the case study of TC Gaemi (2018).

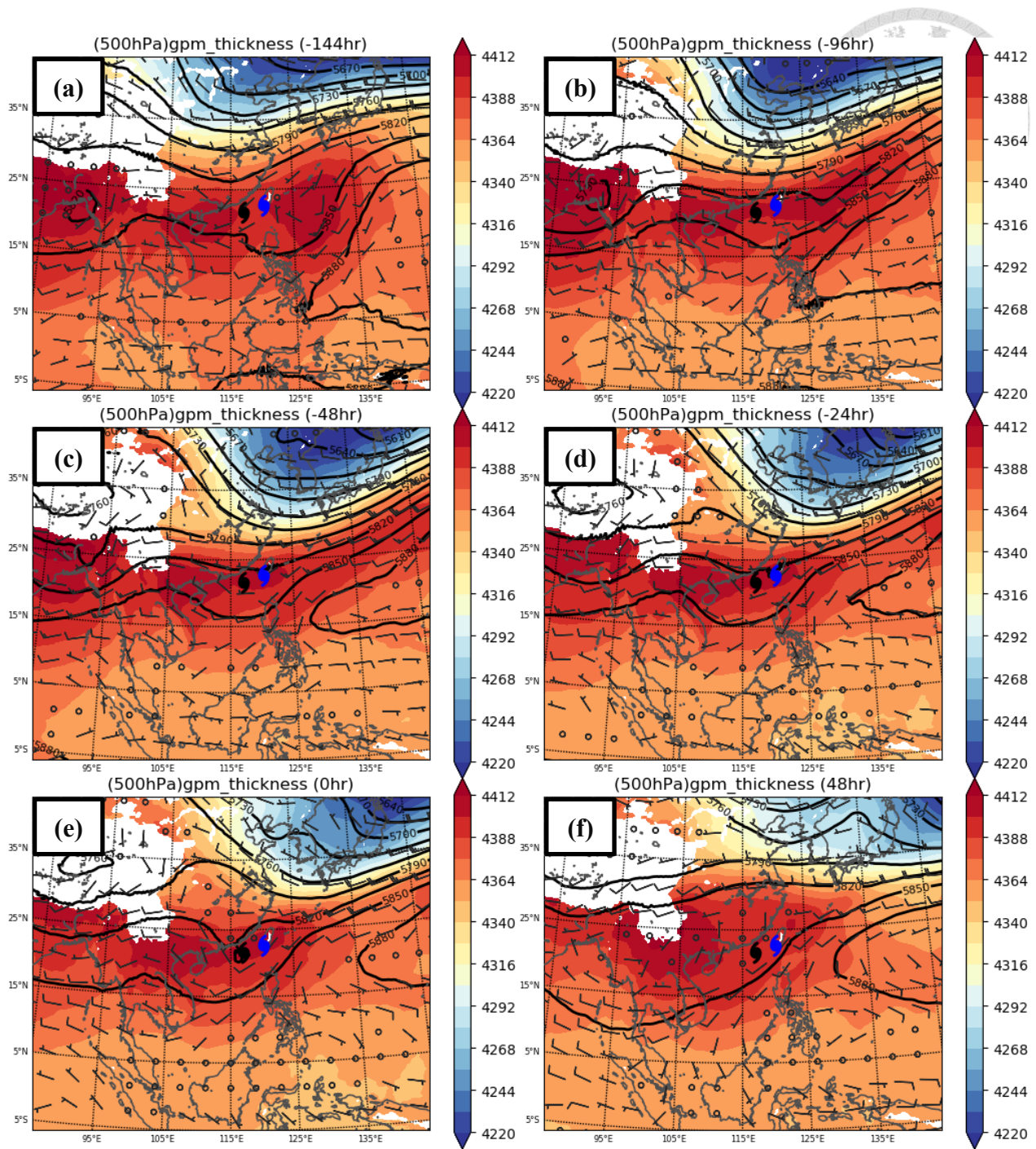


Figure 13. Same as Figure 6 except for the case study of TC Gaemi (2018).

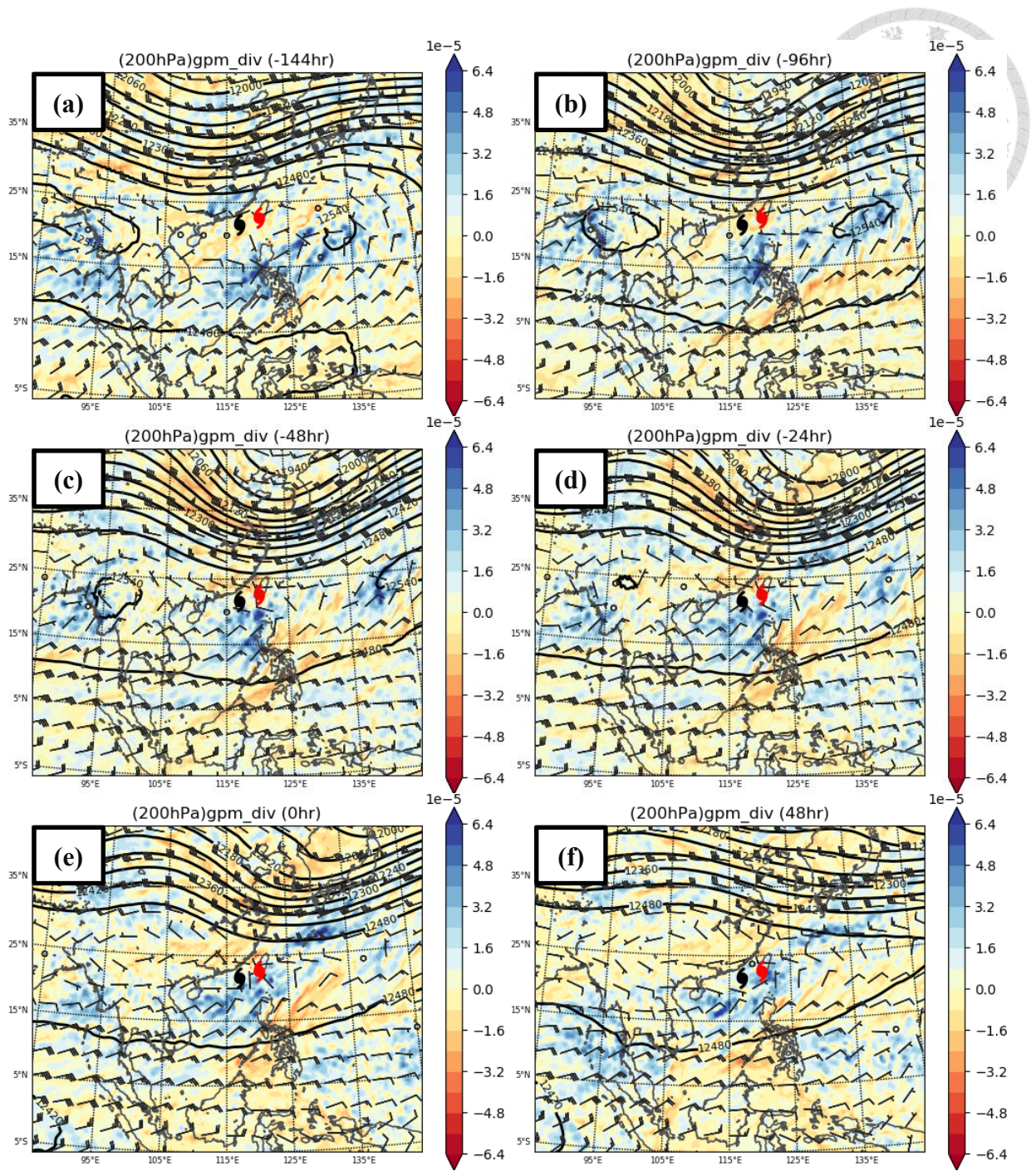


Figure 14. Same as Figure 7 except for the case study of TC Gaemi (2018).

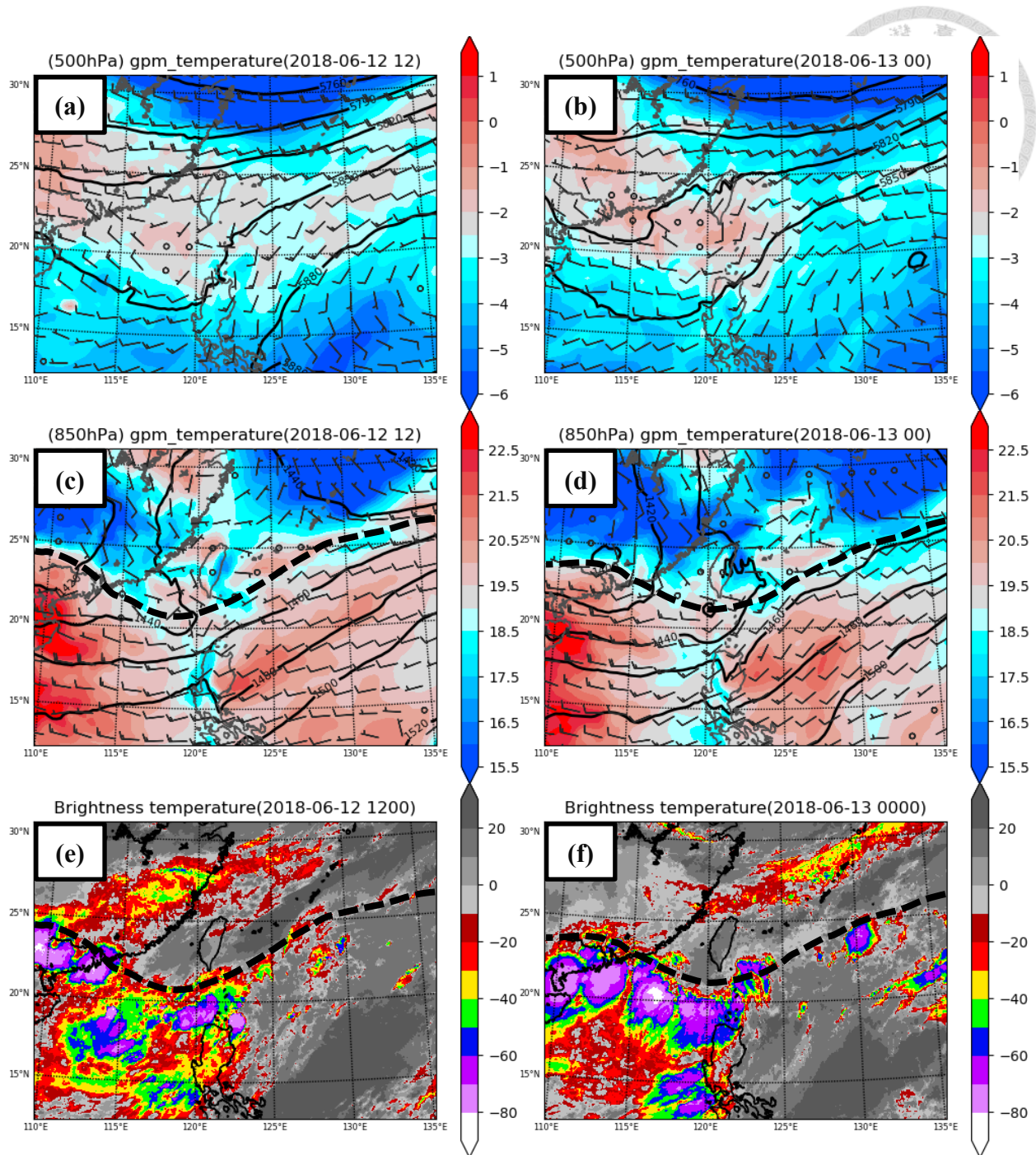


Figure 15. Gaemi's local evolution. The dashed line marked the location of the Mei-Yu front (wind shear line). (a), (c), (e) are at 12 UTC 12 June and (b), (d), (f) are at 00 UTC 13 June. (a) and (b) show the 500-hPa temperature (color, °C), geopotential height (solid line, m) and wind (barb, m/s) in reanalysis data. (c) and (d) show the 850-hPa temperature (color, °C), geopotential height (solid line, m) and wind (barb, m/s) in reanalysis data. (e) and (f) are the brightness temperature (°C) of Band-13 from Himawari-9 Satellite.

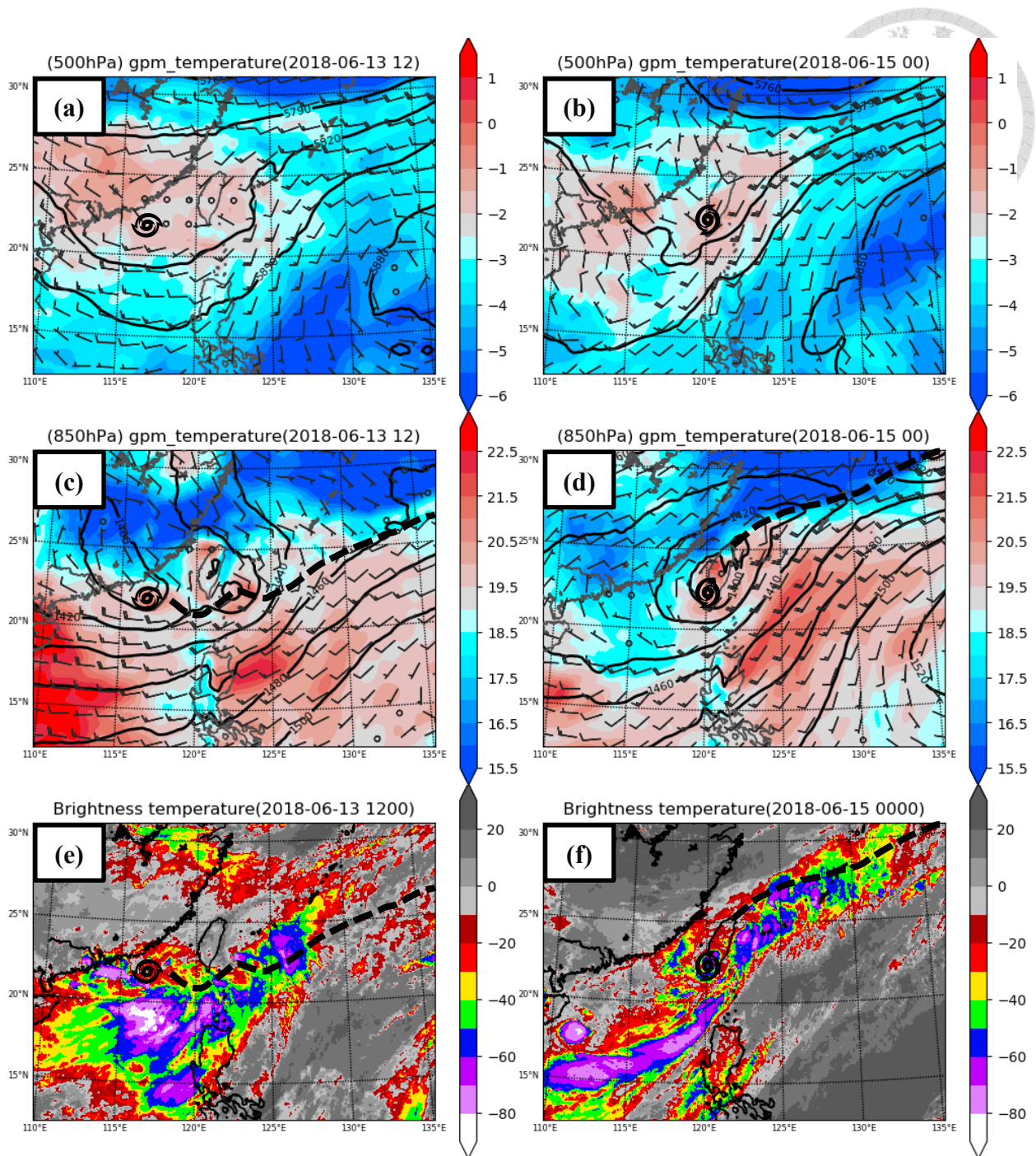


Figure 16. Same as Figure 15 except (a), (c), (e) at 12 UTC 13 June and (b), (d), (f) at 00 UTC 15 June

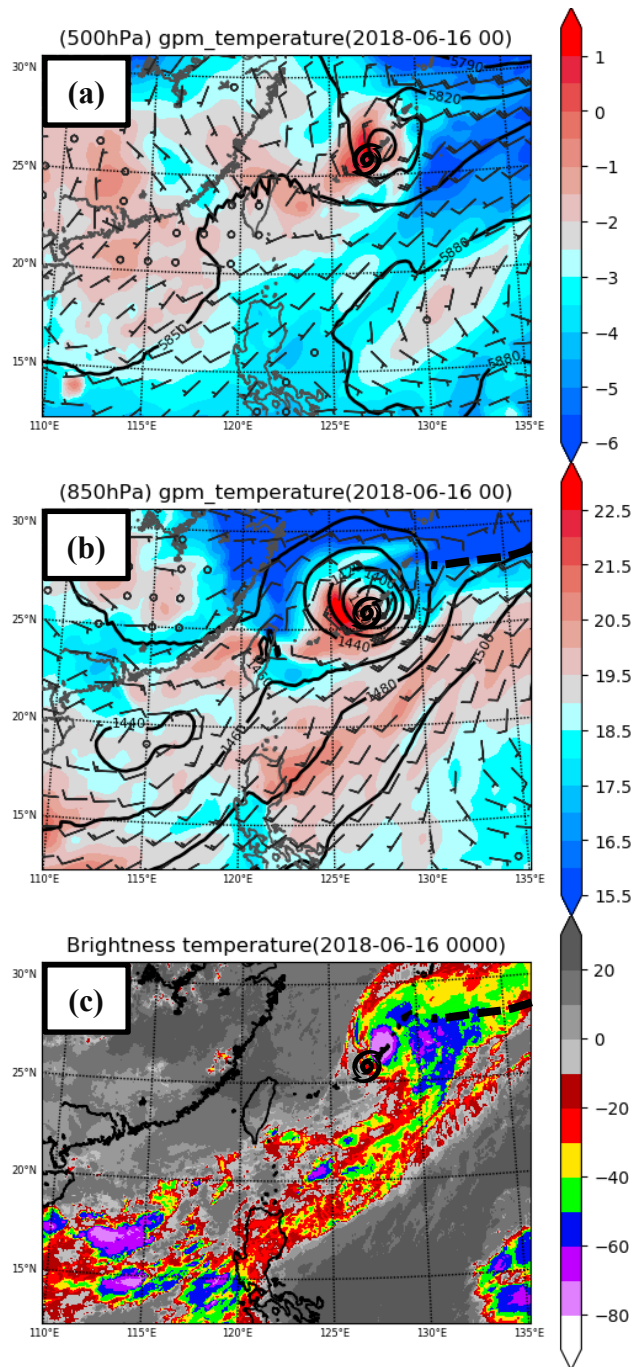


Figure 17. Same as Figure 15 except at 00 UTC 16 June.

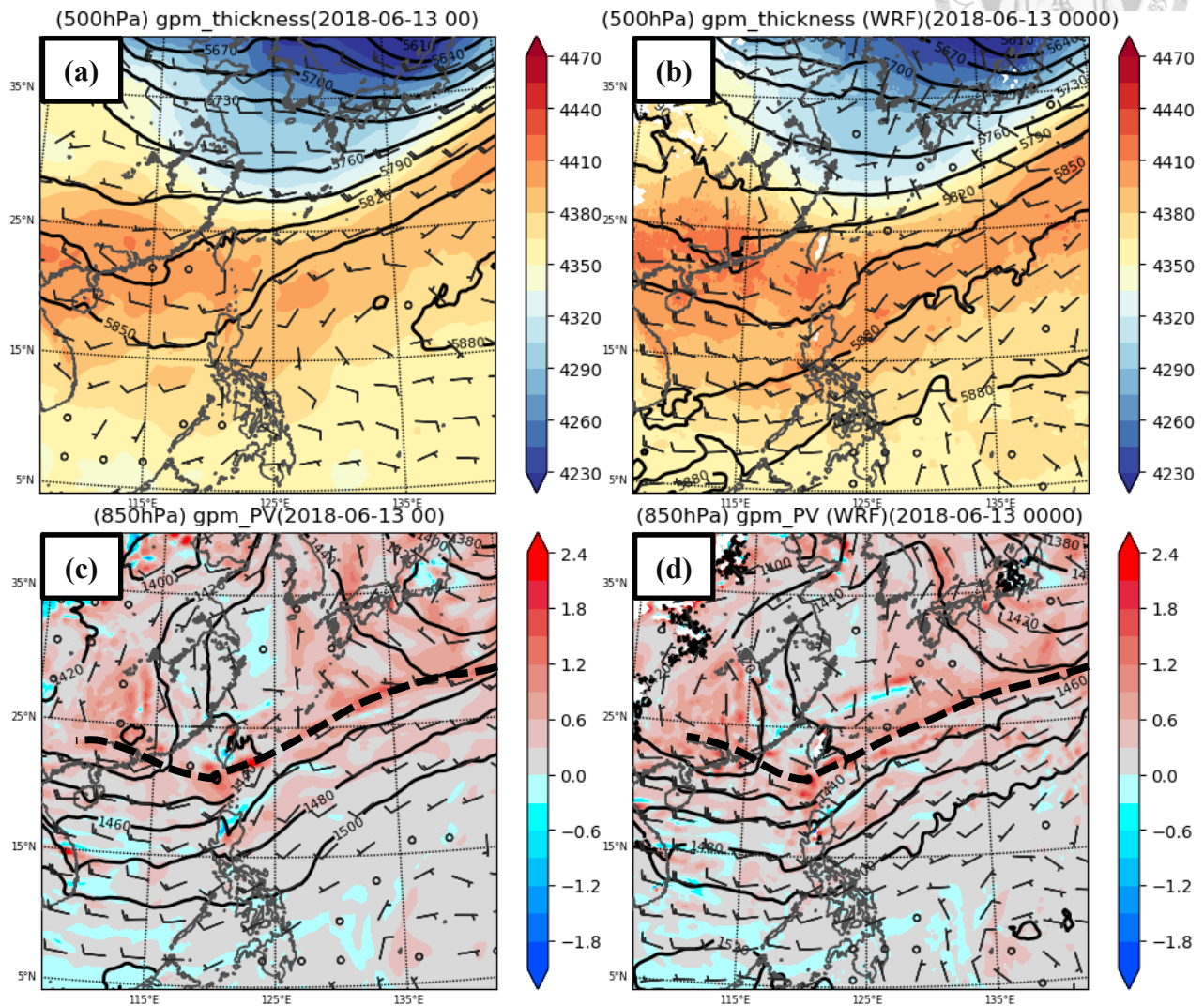


Figure 18. The comparison of the synoptic-scale evolution between reanalysis data and CTL simulation at 00 UTC 13 June. The dashed lines marked the locations of the Mei-Yu front (wind shear line). (a), (c) are from reanalysis data and (b), (d) are from CTL simulation. (a), (b) show the thickness between 850 hPa and 500 hPa (color, m), 500-hPa geopotential height (solid line, m) and 500-hPa wind (barb, m/s). (c), (d) show 850-hPa potential vorticity (color, PVU), 850-hPa geopotential height (solid line, m) and 850-hPa wind (barb, m/s).

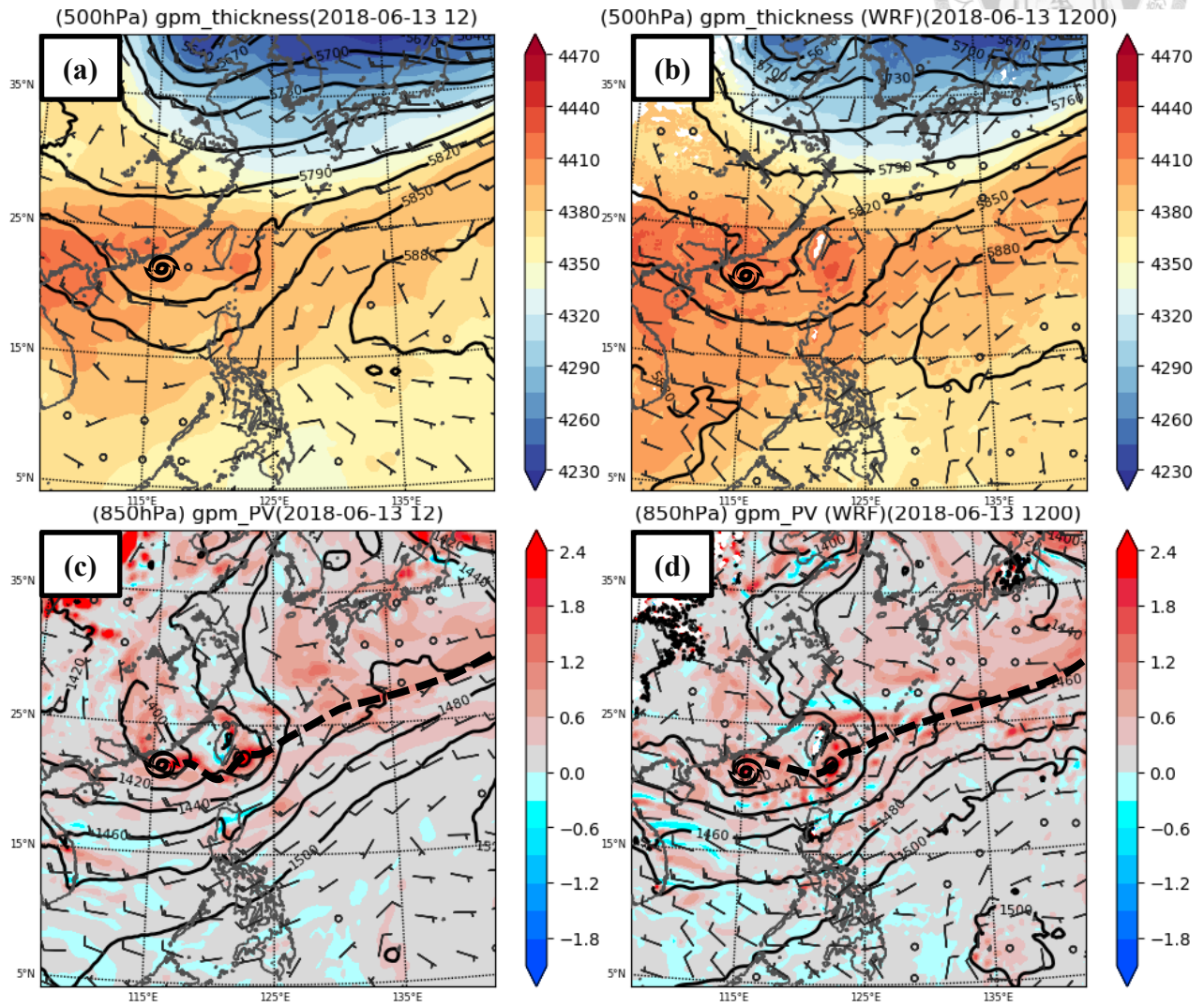


Figure 19. Same as Figure 18 except at 12 UTC 13 June.

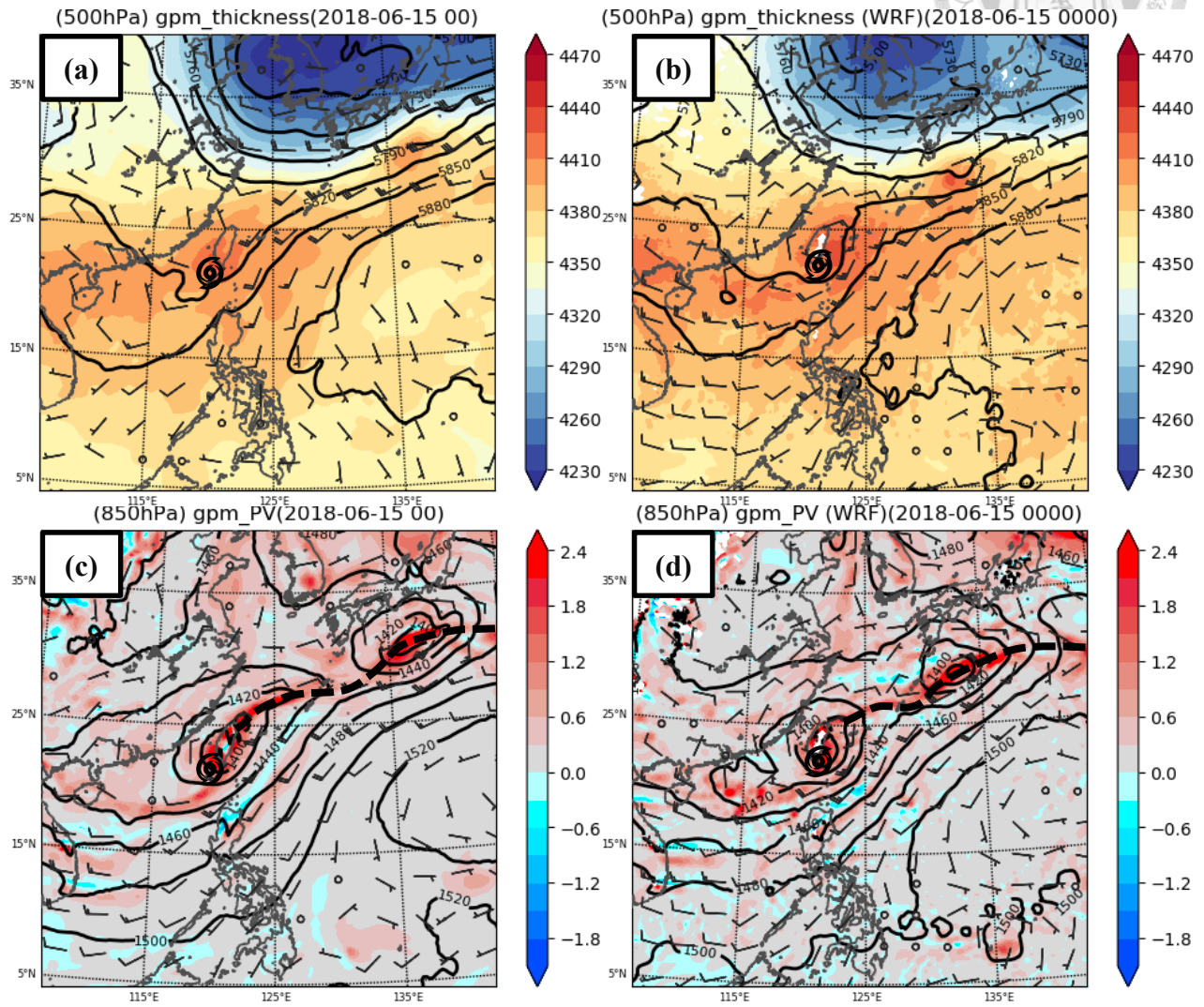


Figure 20. Same as Figure 18 except at 00 UTC 15 June.

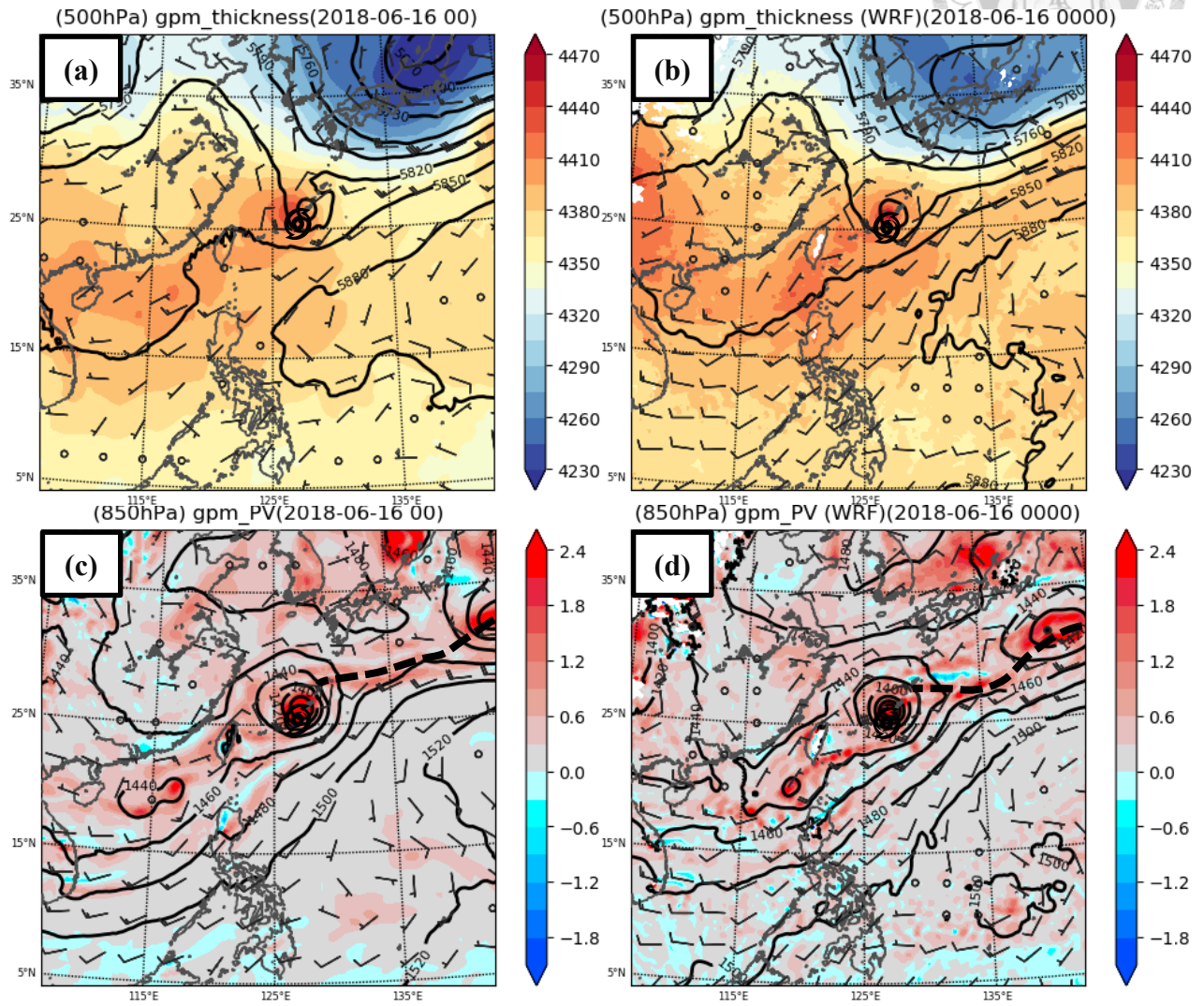


Figure 21. Same as Figure 18 except at 00 UTC 16 June.

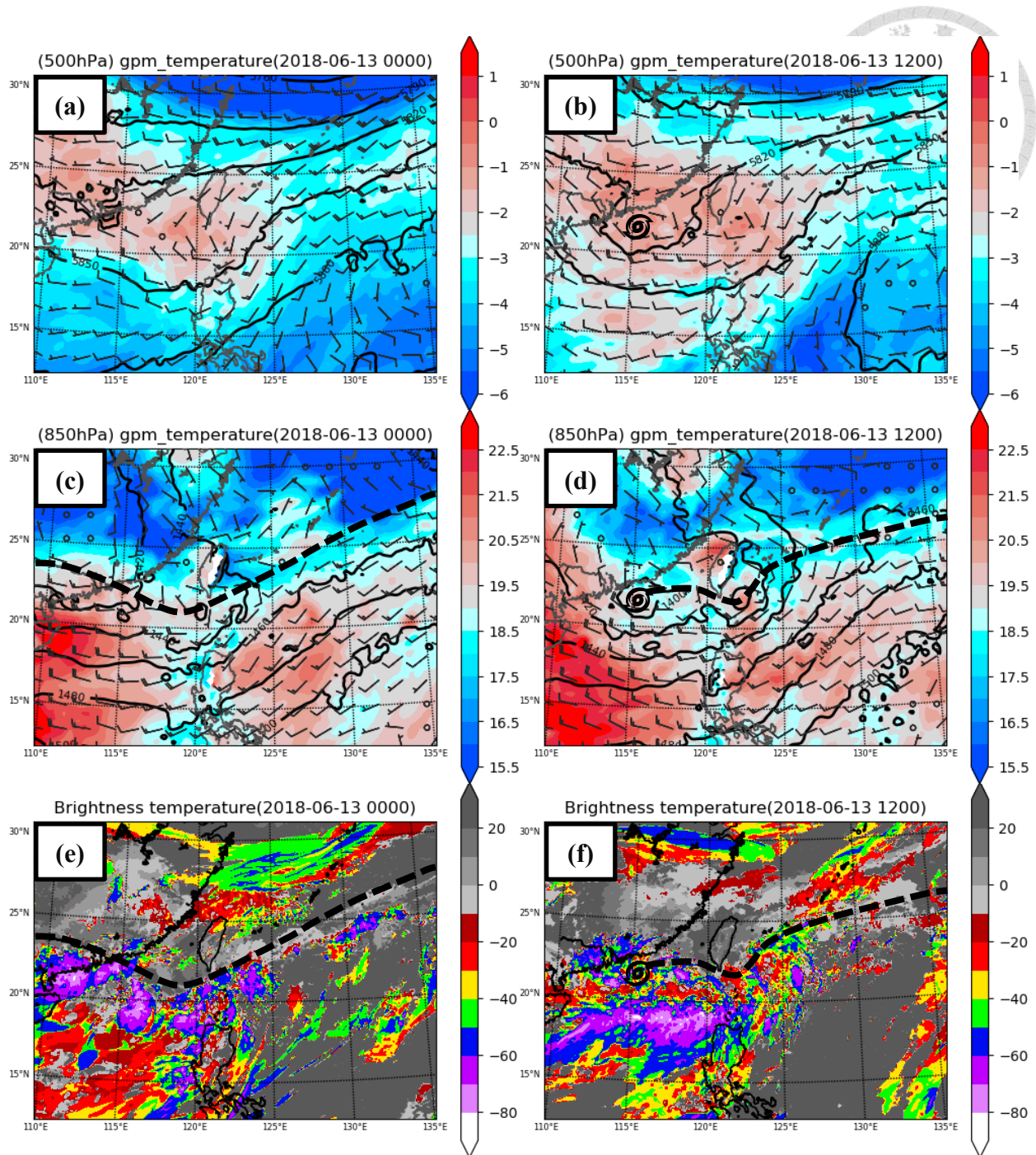


Figure 22. Gaemi’s local evolution in the CTL simulation. The TC symbols are Gaemi and dashed lines marked the locations of the Mei-Yu front (wind shear line). (a), (c), (e) are at 00 UTC 13 June and (b), (d), (f) are at 12 UTC 13 June. (a) and (b) show the 500-hPa temperature (color, °C), geopotential height (solid line, m) and wind (barb, m/s). (c) and (d) show the 850-hPa temperature (color, °C), geopotential height (solid line, m) and wind (barb, m/s) (e) and (f) are the brightness temperature (°C).

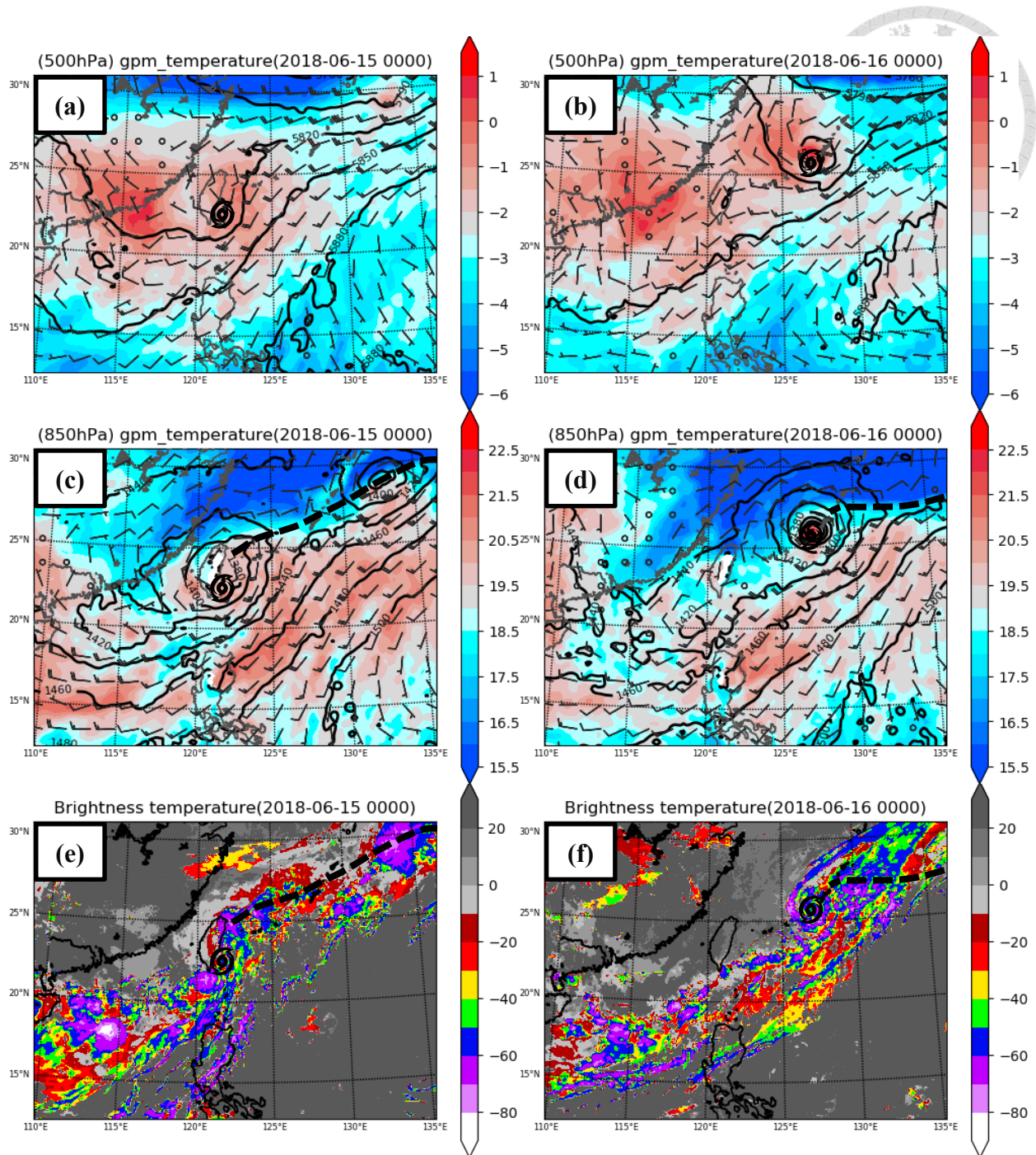


Figure 23. The same as Figure 22 except (a), (c), (e) at 00 UTC 15 June and (b), (d), (f) at 00 UTC 16 June.

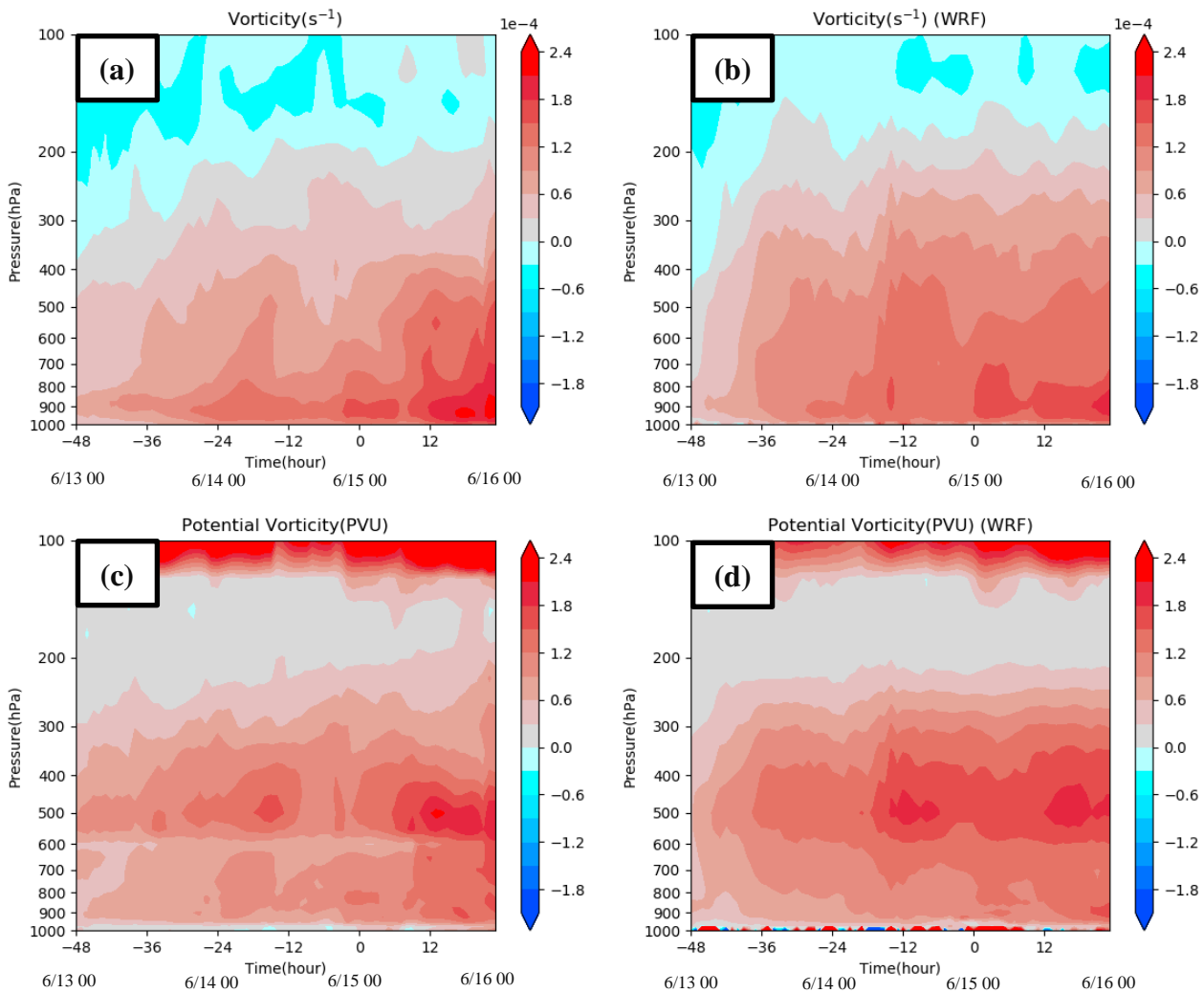


Figure 24. The comparison of the vortex-scale evolution between the reanalysis data and CTL simulation. The vorticity and PV were averaged within 200 km from Gaemi's center. The time label which was marked by hours was relative to the time when Gaemi intensified as a TS. (a), (c) are the cyclogenesis process from reanalysis data and (b), (d) are from CTL simulation. (a), (b) are relative vorticity and (c), (d) are PV.

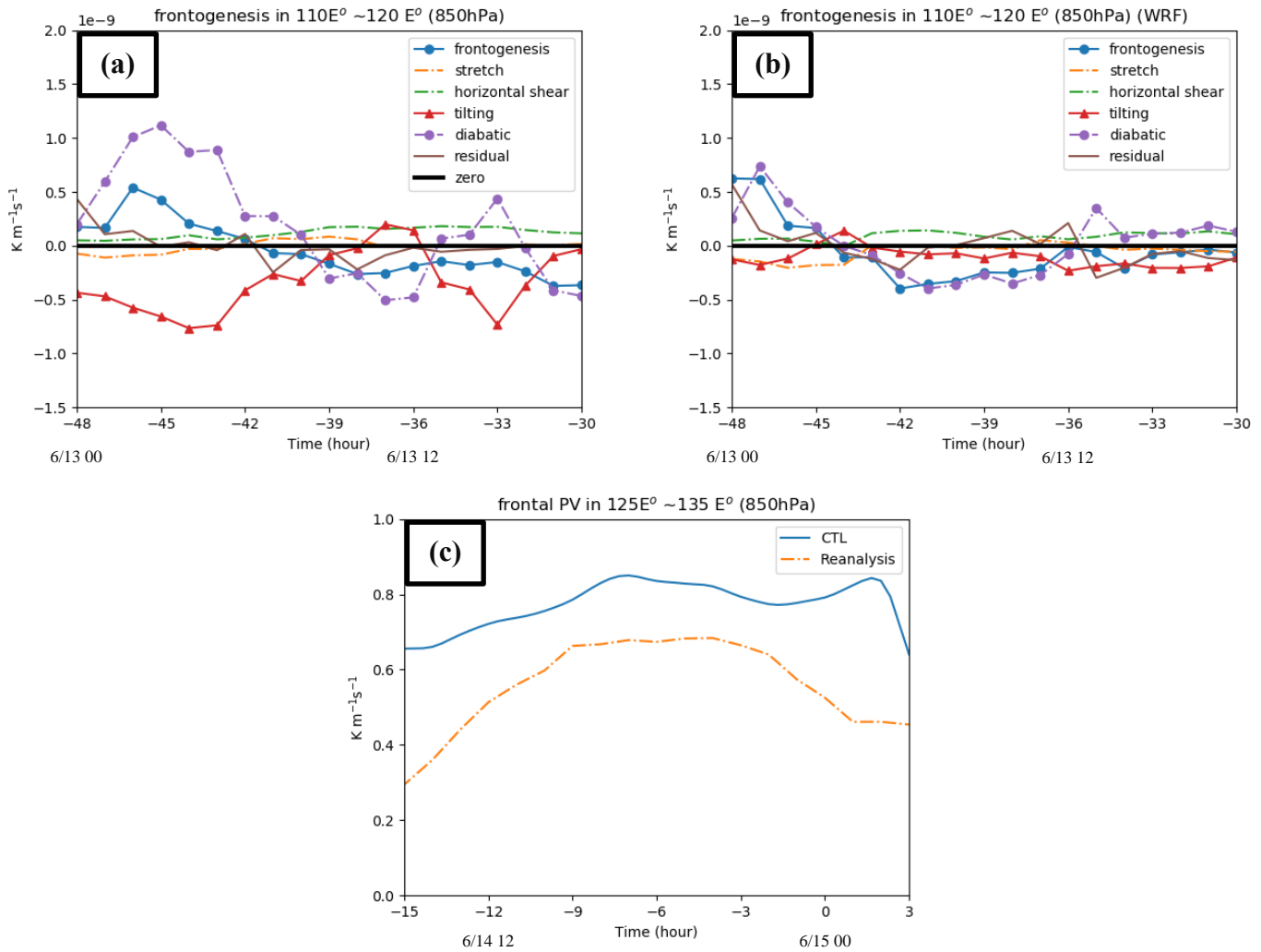


Figure 25. The comparison of the frontal evolution between reanalysis data and the CTL simulation. The frontogenesis function and PV were averaged within 200 km from the front. The time label which was marked by hours was relative to the time when Gaemi intensified as a TS. (a), (b) are the frontogenesis function in reanalysis and the CTL run, respectively, prior to Gaemi's formation between 110°E and 120°E. (c) is the comparison of PV in reanalysis and the CTL simulation between 125°E and 135°E as Gaemi approached.

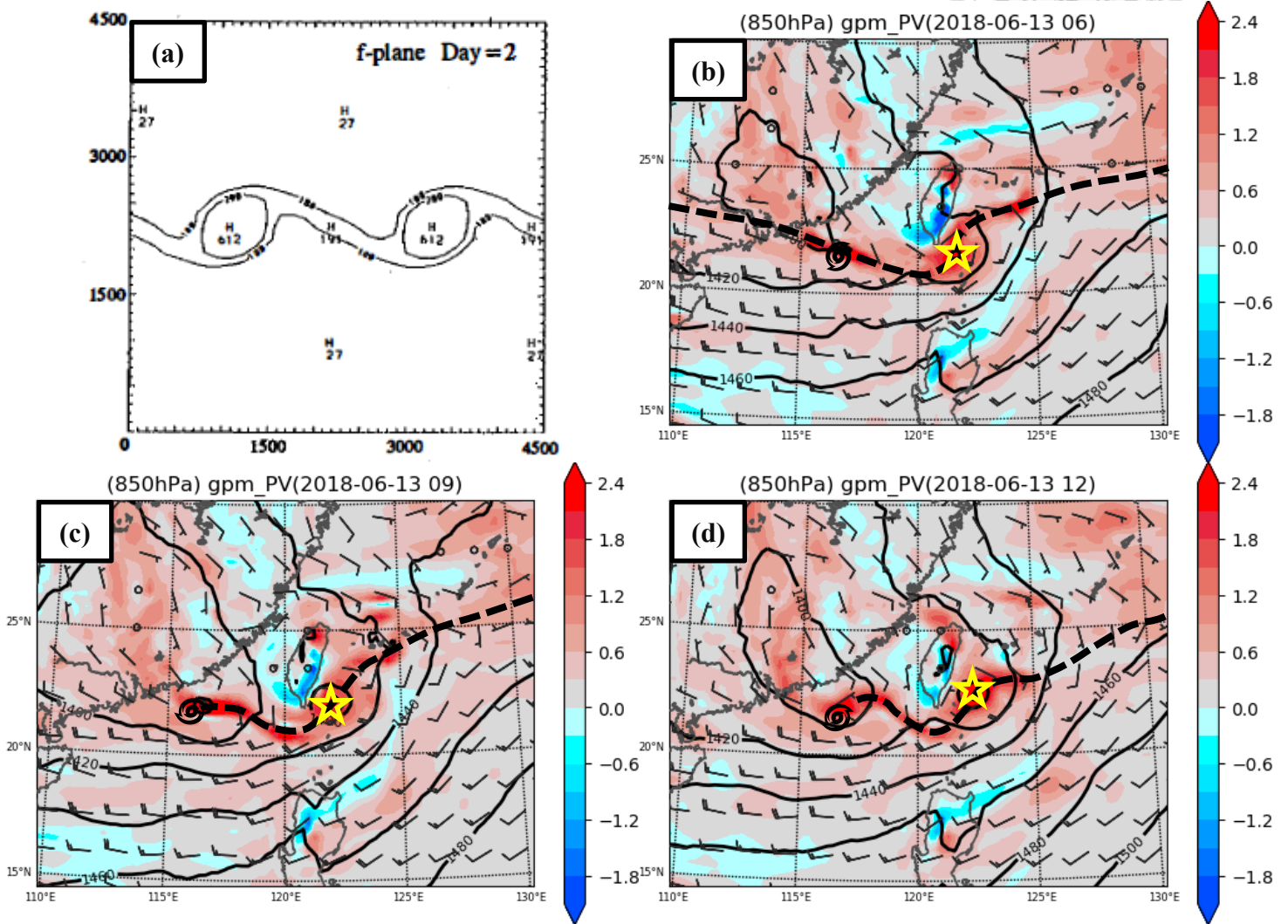


Figure 26. The subjectively analysis of barotropic instability. (a) is a classic mass-field distribution of the barotropic instability (Kuo and Horng 1994). In (b) (06 UTC), (c) (09UTC) and (d) (12 UTC), the TC symbols is the frontal vortex which developed into Gaemi and the star is another frontal vortex. The dashed line is the location of the front (wind-shear line). The color, contour, and barbs are PV (PVU), geopotential height (m), and wind (m/s), respectively.

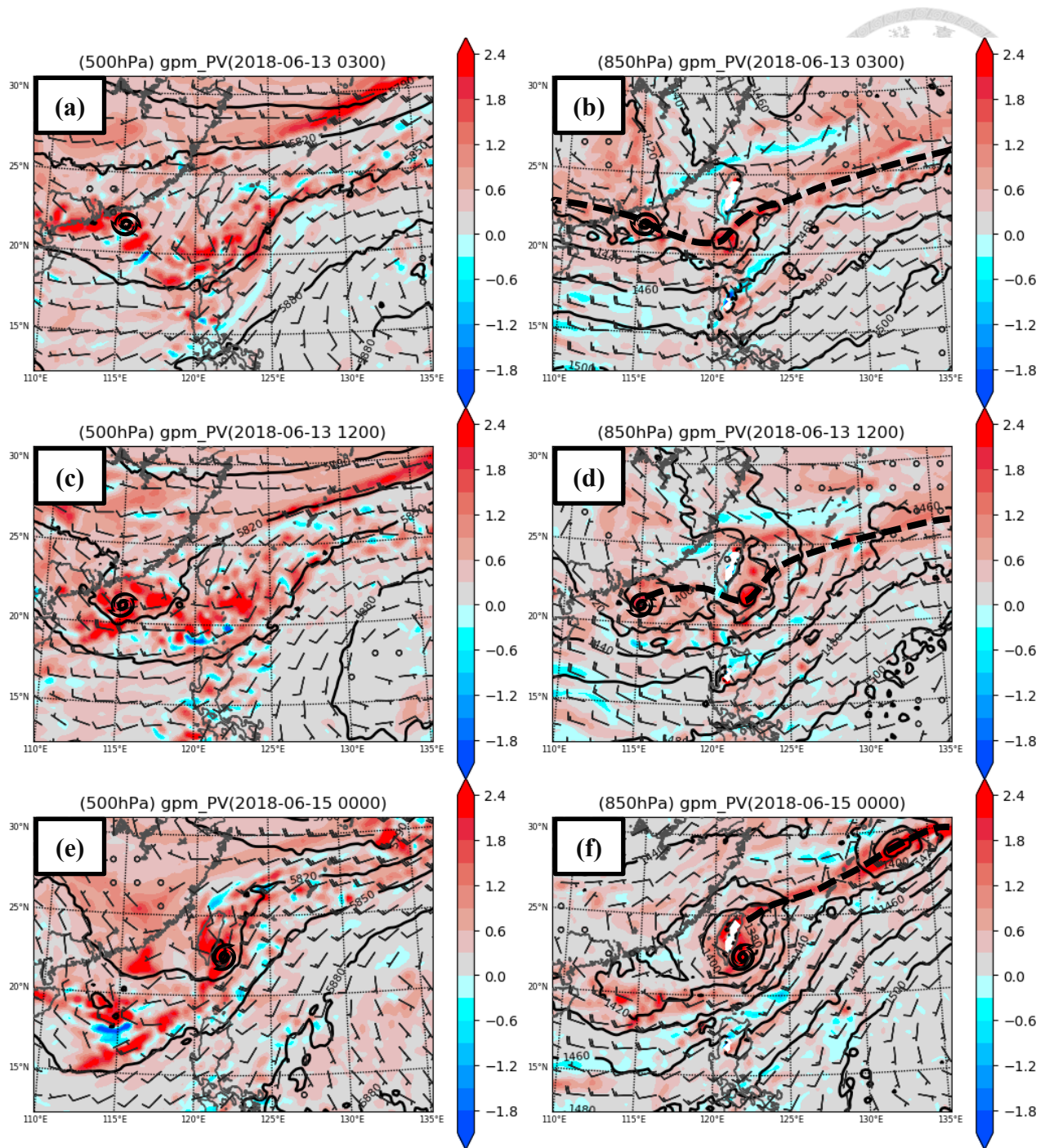


Figure 27. The PV distribution at 500 hPa and 850 hPa. The TC symbols are Gaemi. The dashed line is the Mei-Yu front. The color, contour, and barbs are PV (PVU), geopotential height (m), and wind (m/s), respectively. (a), (c), (e) are 500-hPa distributions at 03 UTC 13 June, 12 UTC 13 June and 00 UTC 15 June. (b), (d), (f) are 850-hPa evolutions at 03 UTC 13 June, 12 UTC 13 June and 00 UTC 15 June.

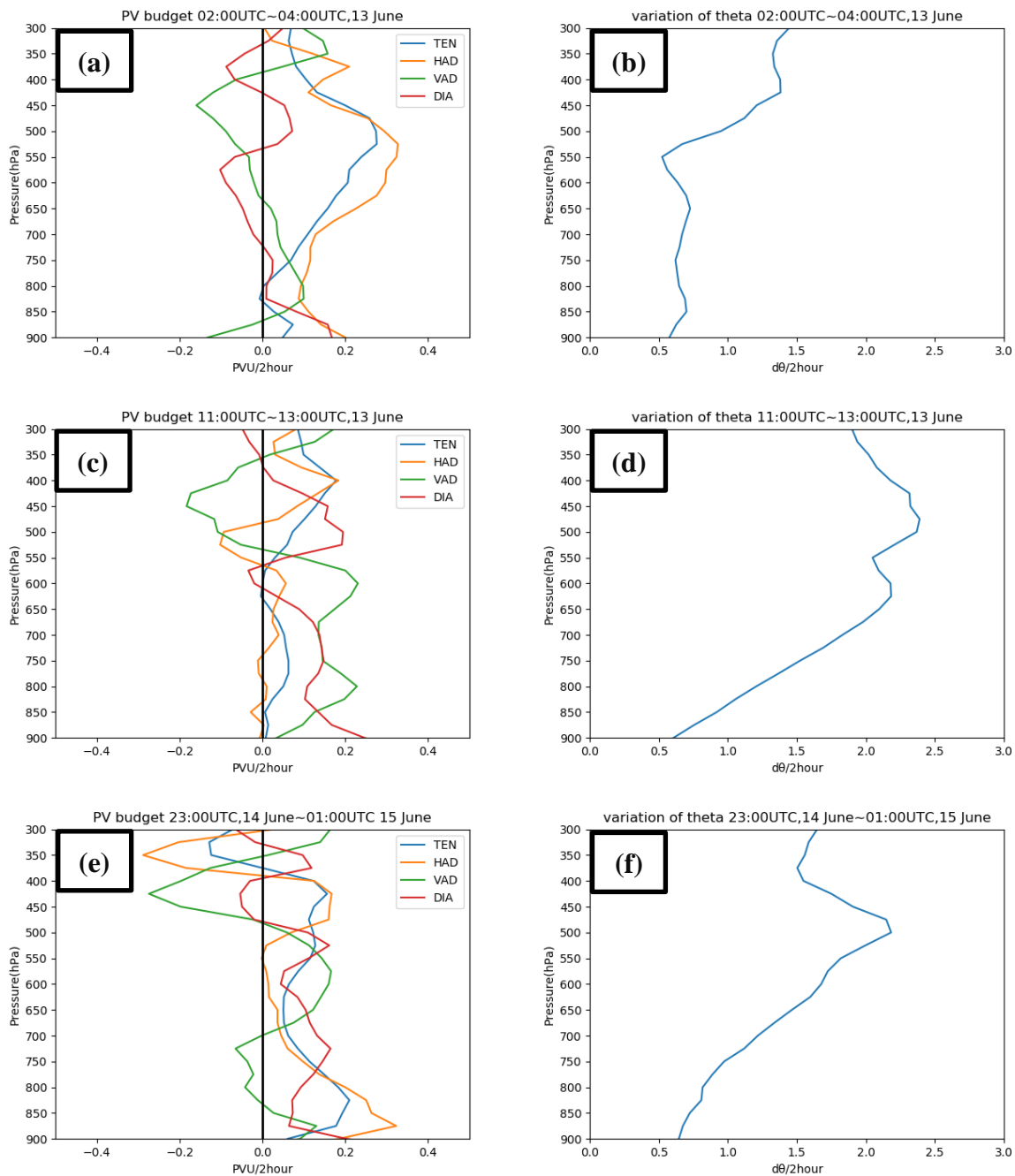


Figure 28. The PV budget and the associated diabolic heating. (a), (c), (e) are the PV profiles contributed by different forcings (PVU/2hours) from 02 to 04 UTC 13 June, 11 to 13 UTC 13 June, and 23 UTC 14 June to 01 UTC 15 June, respectively. (b), (d), (f) are the diabolic heating profiles (K/2hours) from 02 to 04 UTC 13 June, 11 to 13 UTC 13 June, and 23 UTC 14 June to 01 UTC 15 June, respectively.

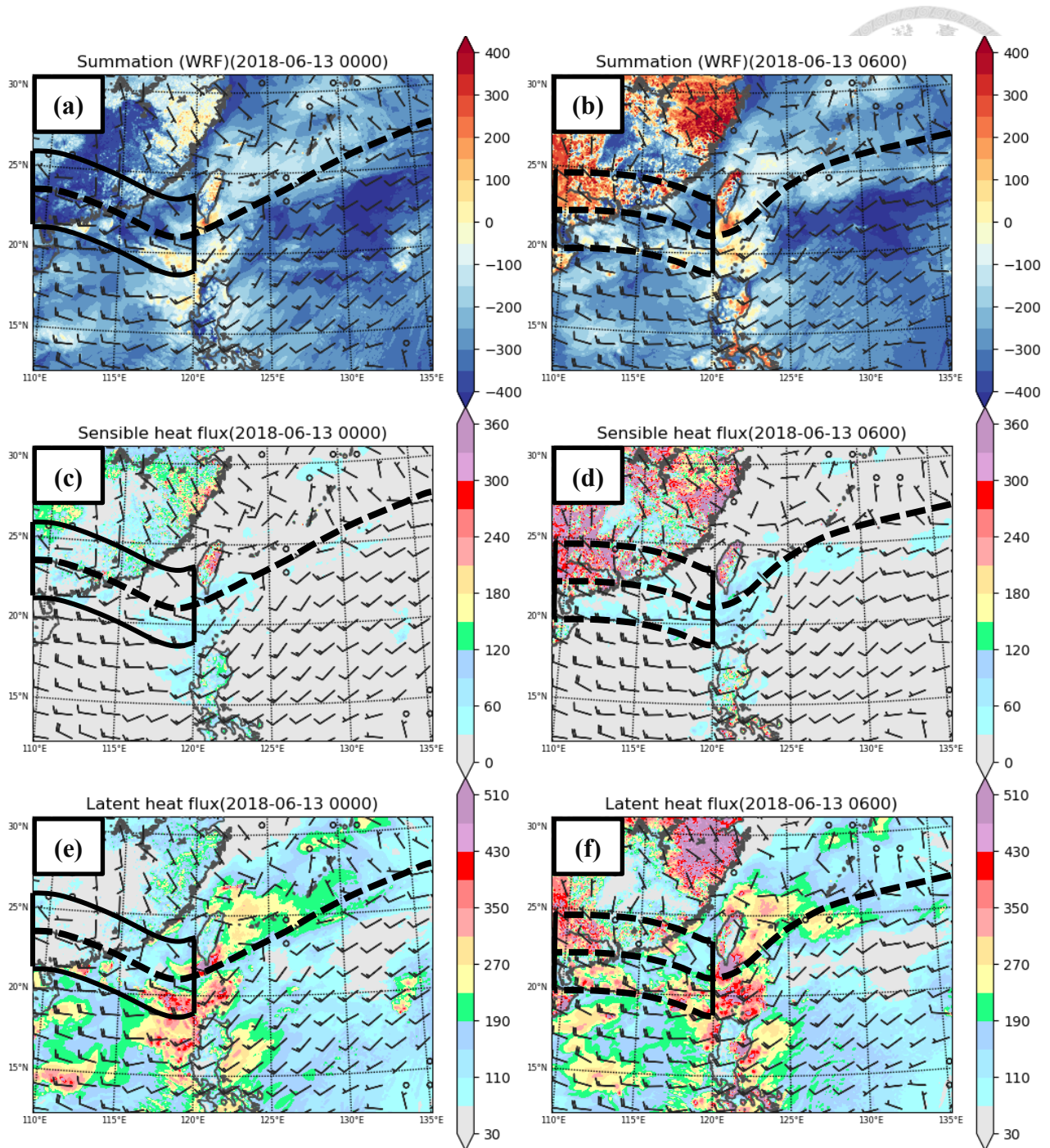


Figure 29. Diabatic heating in frontal boundary layer prior to Gaemi's formation. The dashed line is the location of the Mei-Yu front and the black box is the calculation domain of Figure 25(b). The barbs are wind. The color in (a) and (b) is summation of sensible heat flux, latent heat flux and long-wave radiation (W/m^2). The color in (c) and (d) is sensible heat flux (W/m^2) from surface. The color in (e) and (f) is latent heat flux (W/m^2) from surface. In addition, (a), (c) and (e) are at 00 UTC 13 June (frontogenesis stage). (b), (d), (e) are at 06 UTC 13 June (frontolysis stage).

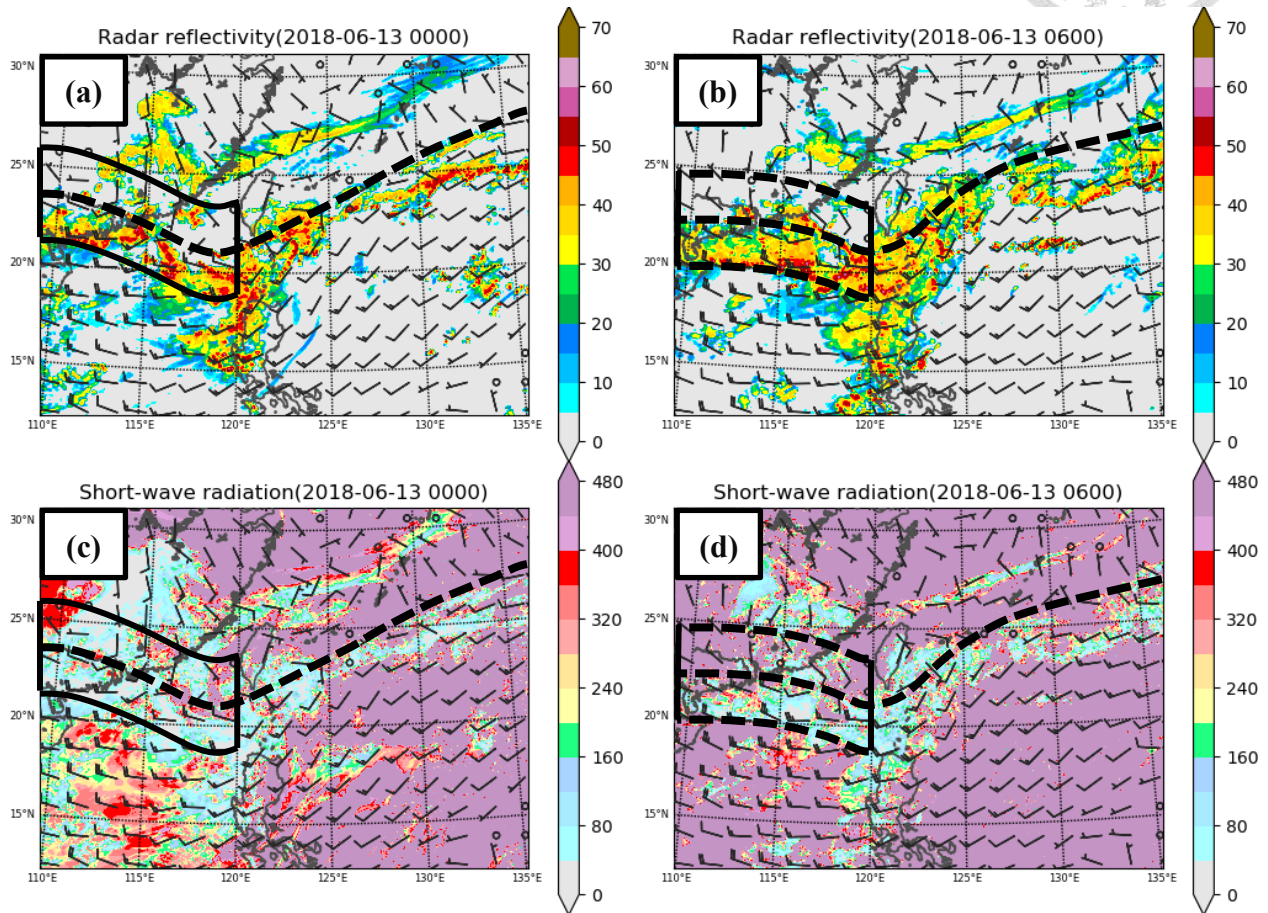


Figure 30. Same as figure 29. The color in (a) and (b) is radar reflectivity (dBz). The color in (c) and (d) is downward short-wave radiation at surface (W/m²). In addition, (a), (c) are at 00 UTC 13 June (frontogenesis stage). (b), (d), are at 06 UTC 13 June (frontolysis stage).

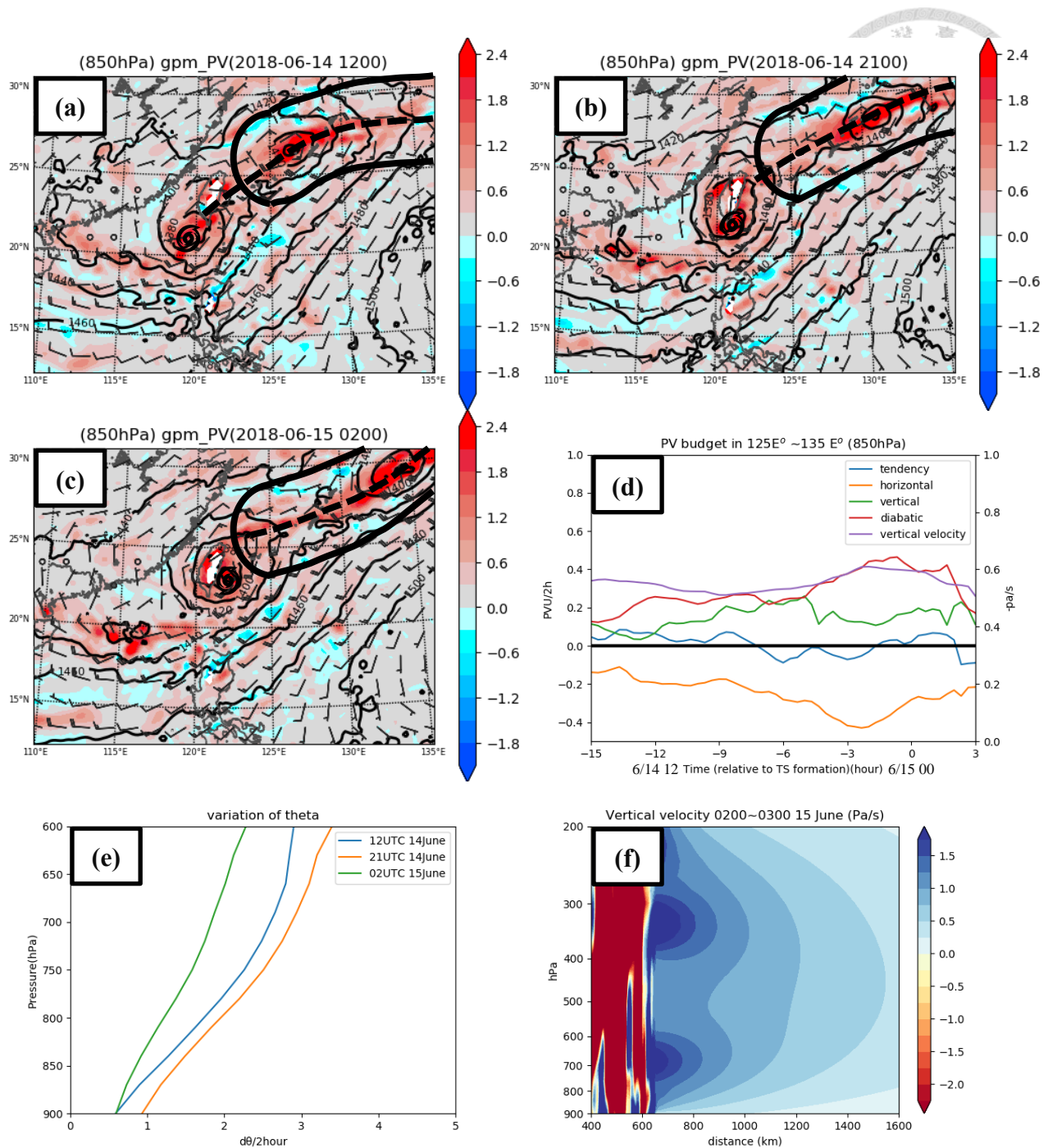


Figure 31. The frontolysis process from the PV aspect. (a), (b) and (c) are the PV distribution (color), geopotential height (contour), and wind (barbs) at 850 hPa. (d) shows the PV budget terms (PVU/2hours) and vertical velocity (-Pa/s). Every term was averaged within the black box in a-c. (e) is the diabatic heating below 600 hPa (K/2hours). (f) was the vertical velocity from the diagnose of Sawyer-Eliassen equation.

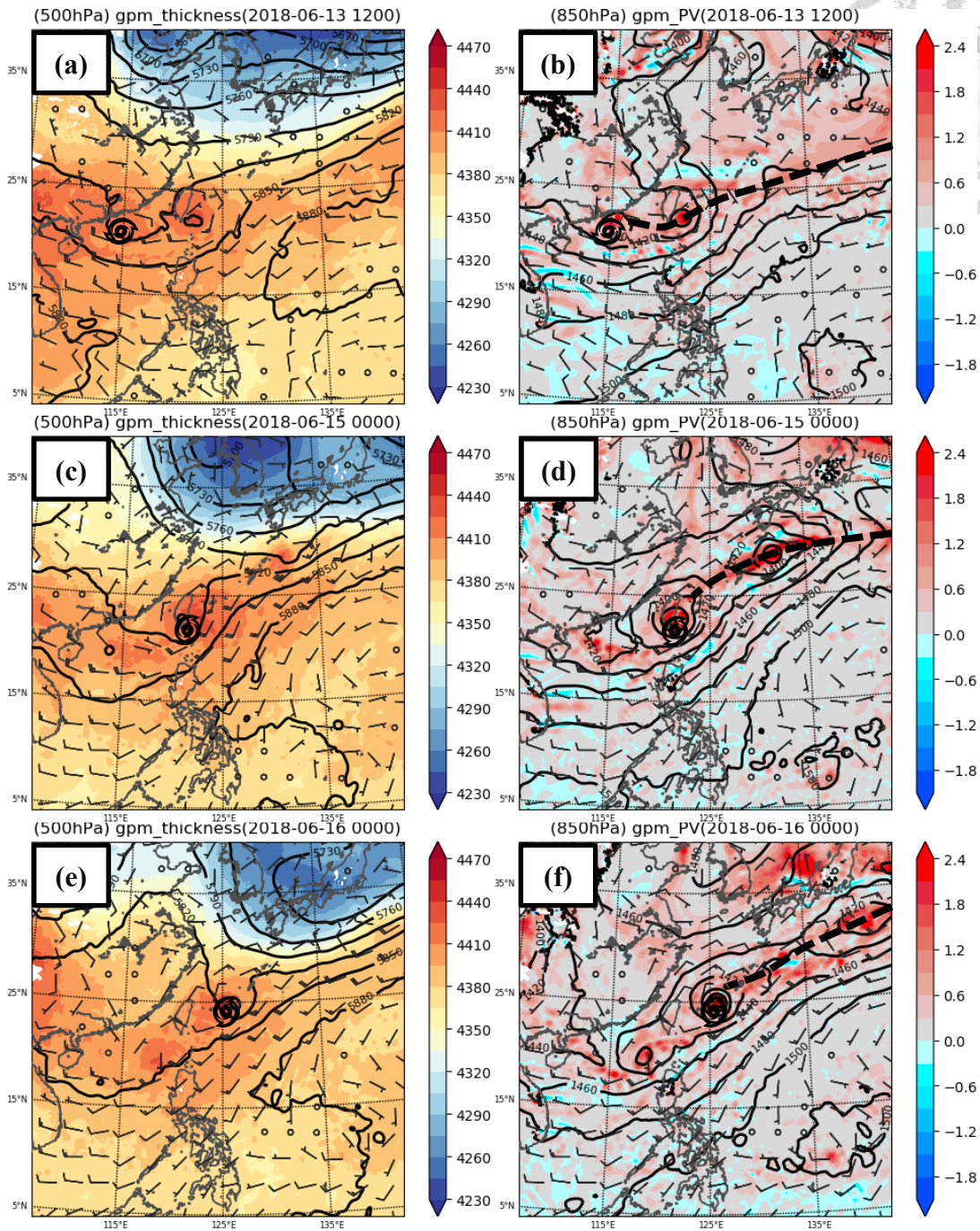


Figure 32. The synoptic-scale evolution in Noterrain simulation. The TC symbols are Gaemi and the dash lines marked the location of the Mei-Yu front (wind shear line). (a), (c) and (e) illuminate the thickness between 850 hPa and 500 hPa (color, m), 500-hPa geopotential height (solid line, m) and 500-hPa wind (barbs, m/s). (b), (d) and (f) show 850-hPa potential vorticity (color, PVU), 850-hPa geopotential height (solid line, m) and 850-hPa wind (barbs, m/s).

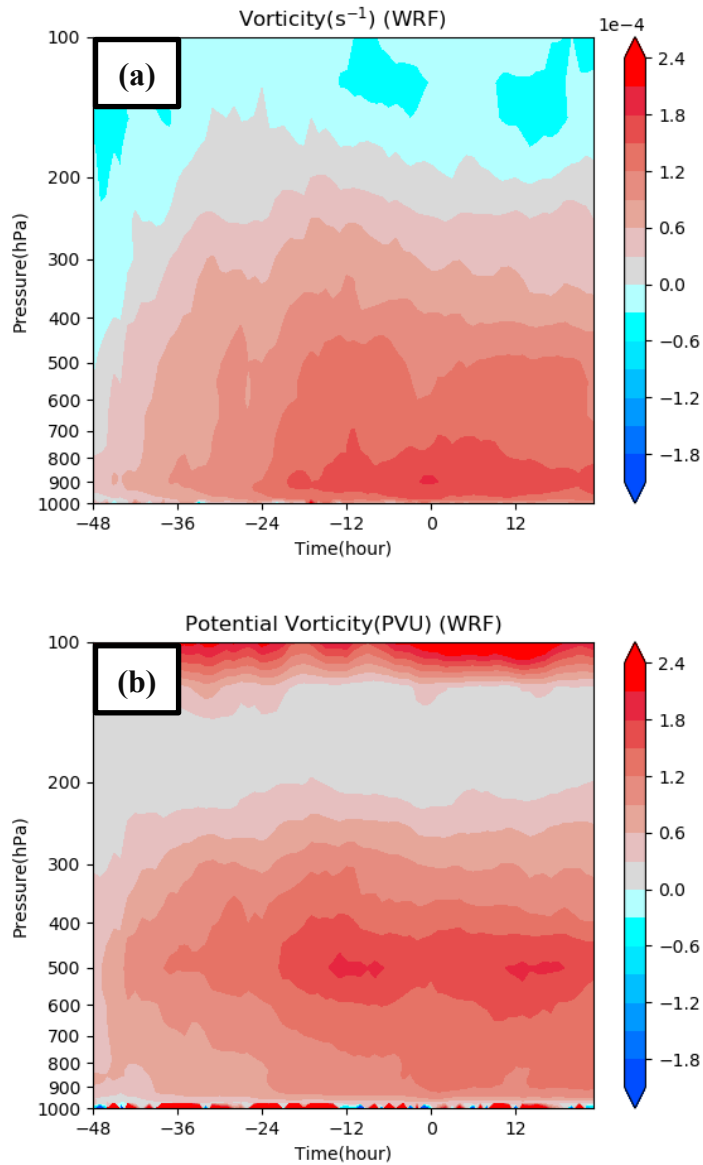


Figure 33. The vortex-scale evolution in Noterrain simulation. The vorticity and PV were averaged within 200 km from Gaemi's center. (a) is relative vorticity and (b) is PV.

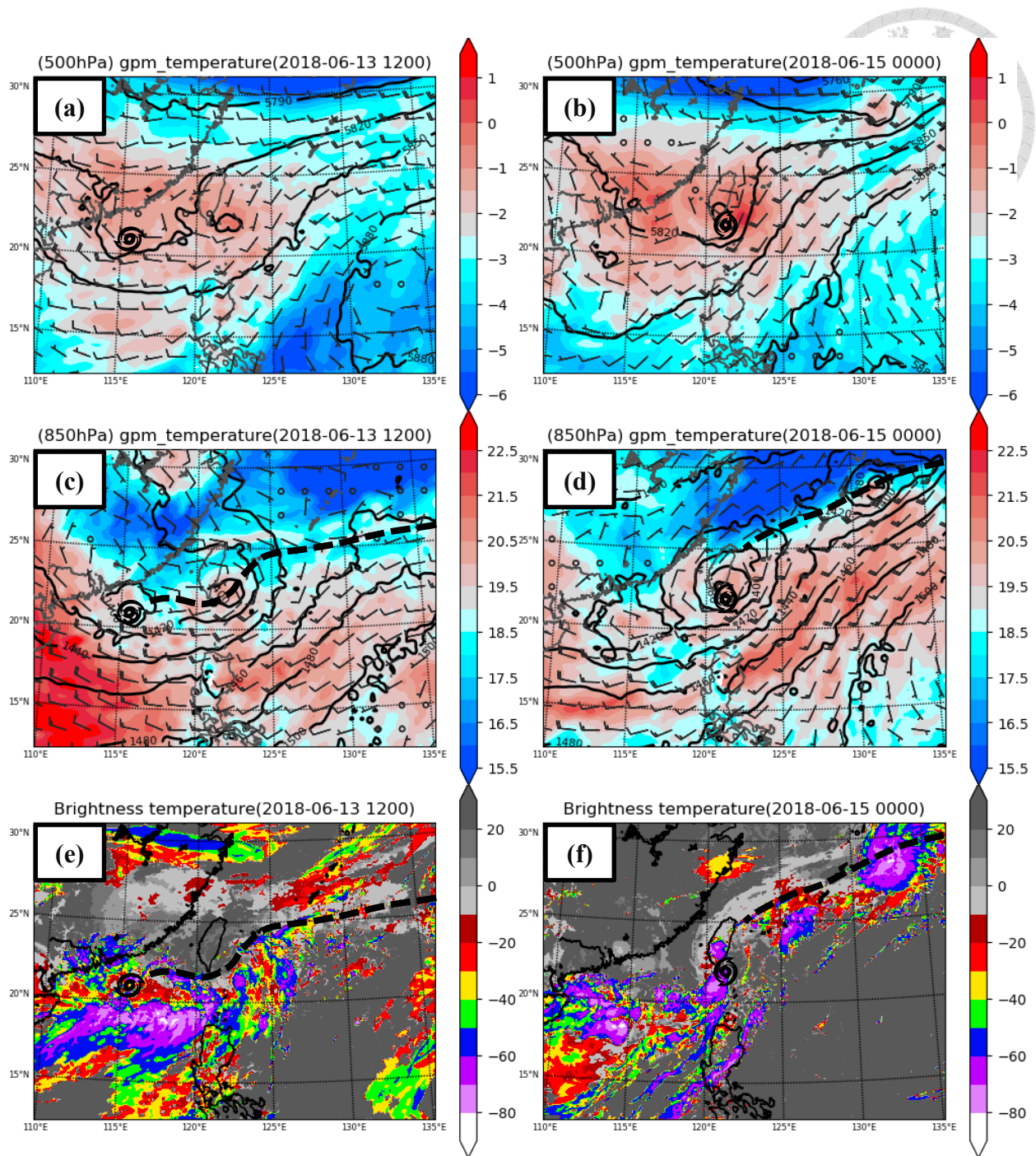


Figure 34. Gaemi's local evolution in Noterrain simulation. The TC symbols are Gaemi and dash lines marked the locations of the Mei-Yu front (wind shear line). (a), (c), (e) are at 12 UTC 13 June and (b), (d), (f) are at 00 UTC 15 June. (a) and (b) show the 500-hPa temperature (color, °C), geopotential height (solid line, m) and wind (barb, m/s) (c) and (d) show the 850-hPa temperature (color, °C), geopotential height (solid line, m) and wind (barb, m/s). (e) and (f) are the brightness temperature (°C).

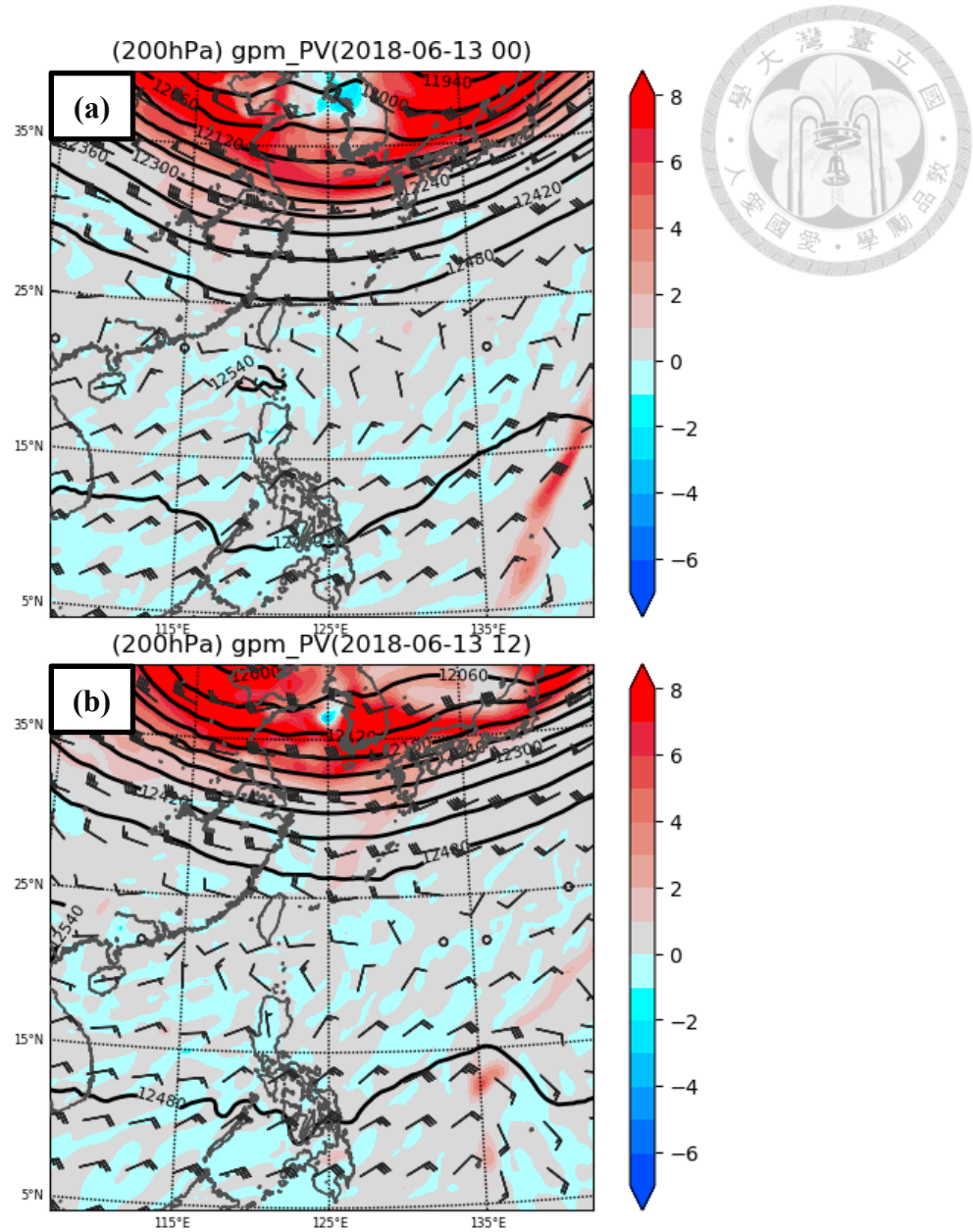


Figure 35. The 200-hPa PV at (a) 00 UTC and (b) 12 UTC on 13 June. The color is PV (PVU), contour is 200 hPa geopotential height (m), and barbs (m/s) are wind.

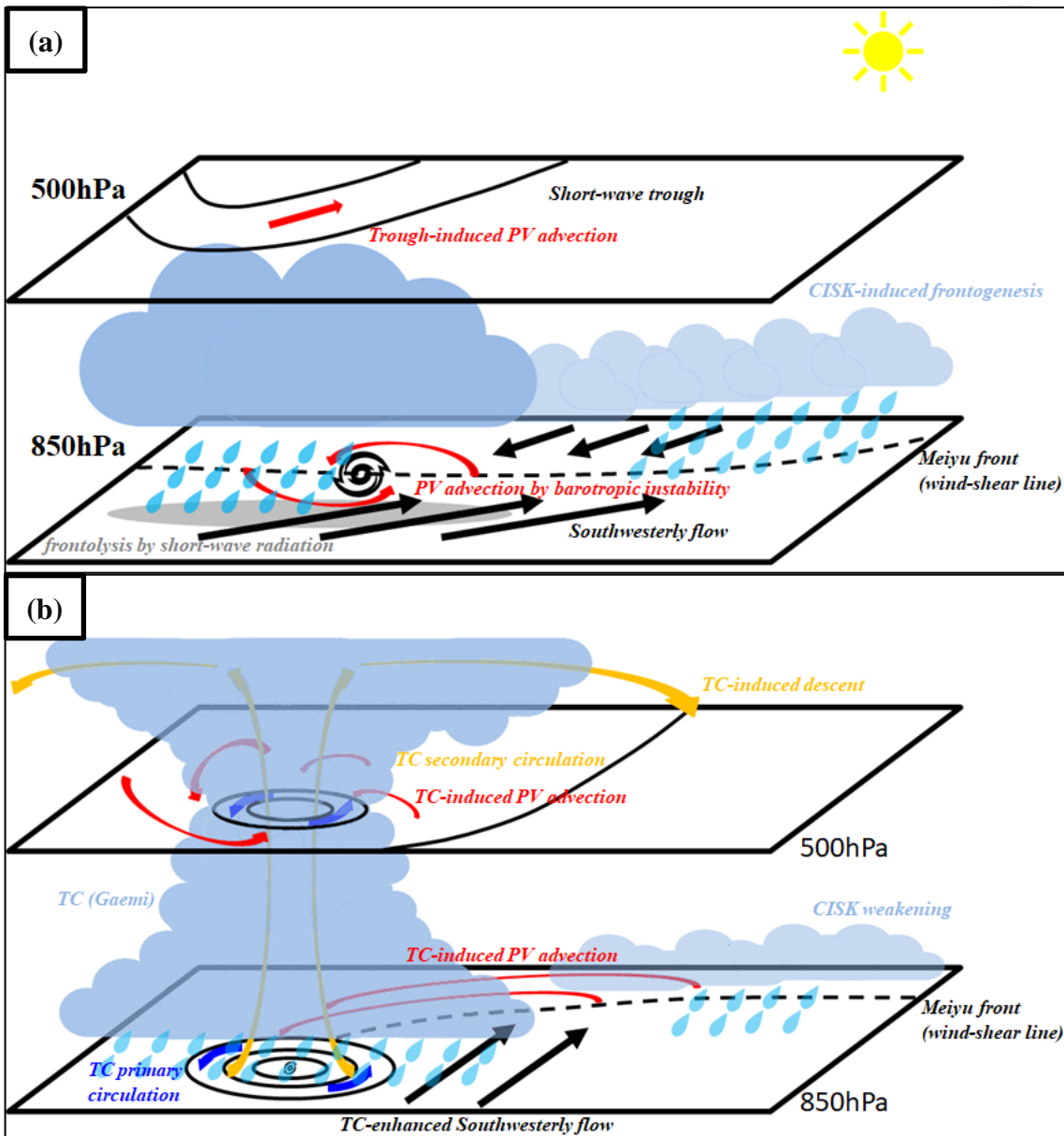


Figure 36. The conceptual model for the interactions between the frontal-type TC and the Mei-Yu front. (a) is prior to TC formation. In this stage, the short-wave radiation induced the frontolysis and the east section of front was maintained by the CISK. The barotropic instability triggered low-level perturbations and the the short-wave trough helped the establishment of the mid-level PV pool. (b) is after TC formation. The TC was a strong PV center to organize the weak PV pool adjacent to the TC. The frontal PV was pumped out by the TC and the secondary circulation of the TC restrained the convection in the frontal region. The front experienced significant frontolysis as TC approached.